NOVA SCHOOL OF
SCIENCE & TECHNOLOGY

PHYSICS DEPARTMENT

ANA FILIPA OLIVA REBELO
Bachelor of Science in Biomedical Engineering

SEMI-AUTOMATIC APPROACH FOR EPICARDIAL FAT SEGMENTATION AND QUANTIFICATION ON NON-CONTRAST CARDIAC CT

MASTER OF SCIENCE IN BIOMEDICAL ENGINEERING

NOVA University of Lisbon
November, 2021

SEMI-AUTOMATIC APPROACH FOR EPICARDIAL FAT SEGMENTATION AND QUANTIFICATION ON NON-CONTRAST CARDIAC CT

ANA FILIPA OLIVA REBELO

Bachelor of Science in Biomedical Engineering

Adviser: José Manuel Fonseca
Associate Professor, NOVA University Lisbon
Co-adviser: António Miguel Ferreira
Cadiologist, Hospital Santa Cruz, Western Lisbon Hospital Center

Examination Commitee:
Chair: Carla Maria Quintão Pereira
Assistant Professor, NOVA University Lisbon
Rapporteur: Ricardo Nuno Pereira Verga e Afonso Vigário
Associate Professor, NOVA University Lisbon
Adviser: José Manuel Fonseca
Associate Professor, NOVA University Lisbon

MASTER OF SCIENCE IN BIOMEDICAL ENGINEERING

NOVA University of Lisbon
November, 2021

Semi-automatic approach for epicardial fat segmentation and quantification on non-contrast cardiac CT

Aos meus pais e mana.

ACKNOWLEDGMENTS

My first appreciation is addressed to my advisor, Professor José Manuel Fonseca, for all his help, support, and motivation. And for instilling in me the passion for scientific research without the fear of being wrong. Thank you for the knowledge sharing and guidance throughout the entire project. I will always be grateful for the opportunity.

Also, I would like to thank my co-adviser, Doctor António Miguel Ferreira, for giving me the chance to realize my master thesis in the biomedical area that has always fascinated me the most. Thank you very much for the availability and precious clinical insights.

To the honorary reviewers of this thesis, thank you immensely for your patience and criticism. Rita, the human being with whom I most share my life (and genetics). Undoubtedly, she is the most patient twin of the two of us. Thank you for everything, especially for the computer insights. To Alex, thank you for the endless support and care. The love I found in you helps me grow in every possible way.

I would like to address a collective acknowledgement to everyone I had the pleasure to work with in all the associative projects I have been part of. To my friends and co-founders of Tec2Med, who taught me that it is possible to create a huge impact in healthcare with limited resources. To my friends of NBN, who joined me in the challenge of doing more on behalf of biomedical engineering students and helped me grow as a leader. To my friends of In-Nova, for pushing me into the craziest project of founding the Junior Enterprise of NOVA School of Science and Technology. Each one of these projects gave me the opportunity to grow, expand my horizons and learn a world of things alongside the most incredible people. I wish you all the best.

To all my friends of the Biomedical Engineering 2016-2021 Class, with whom I created memories that I will cherish forever. To my long-time friends for continuing to cheer each other's success even far away.

Finally, I address the most sincere thanks to my family and, if I may, in Portuguese so that they can understand without needing translation. Aos meus pais, Fátima e Ricardo, por apoiarem todas as minhas escolhas e investirem na minha formação, profissional e pessoal. Por serem os meus maiores fãs e acreditarem sempre em mim. Obrigada por tudo. À Bia, a minha segunda mãe, e à Joana e Zé, por todo o carinho e por me acompanharem em todas as fases da vida. E a toda a minha família (avós, tias, tios, primas e primos), por me ajudarem a crescer e festejarem os meus sucessos comos vossos.

The cost of being wrong is less than
the cost of doing nothing.

- Seth Godin

RESUMO

A gordura epicárdica corresponde ao tecido adiposo que envolve o coração, localizado entre o miocárdio e o pericárdio visceral. O volume de gordura epicárdica (do inglês *Epicardial Fat Volume*, EFV) representa um valioso indicador de eventos cardio- e cerebrovasculares, sem considerar outros fatores de risco. Na prática clínica, os procedimentos para a quantificação de EFV são essencialmente manuais, exigindo elevados custos temporais para os técnicos e médicos e envolvendo frequentemente variabilidade intra- e inter-observadores. A fim de melhorar a repetibilidade dos resultados e reduzir o tempo de processamento, esta tese pretende criar uma ferramenta assistida por computador que realiza automaticamente a segmentação da gordura epicárdica e a quantificação do volume em imagens cardíacas de Tomografia Computadorizada (TC) sem contraste.

Para este propósito, foram desenvolvidos dois métodos. Ambos priveligiam a utilização de técnicas básicas de processamento de imagem que não requerem fase de treino de dados, promovendo uma menor complexidade computacional. A performance dos dois métodos foi avaliada e o método que se mostrou mais preciso foi integrado num protótipo de software (HARTA) igualmente desenvolvido, que permite a intervenção humana em caso de ajustes.

Foram utilizados 20 exames de TC sem contraste (878 imagens no total) para validar o algoritmo. O tempo para segmentar a gordura epicárdica de um exame foi de 8,8±1,1 segundos. Enquanto que para a segmentação exclusivamente manual de um exame, 10 a 26 minutos seriam necessários. A segmentação da gordura epicárdica foi avaliada, obtendo-se uma precisão de 98,83% e um coeficiente de similaridade de 0,7888. A quantificação automática do EFV apresentou coeficientes de correlação de Pearson e Spearman de 0,9366 e 0,8773, respectivamente.

Os resultados obtidos sugerem que a ferramenta proposta tem potencial para ser implementada em contextos clínicos, ajudando os cardiologistas a alcançar um EFV de modo mais rápido e preciso, permitindo um diagnóstico e terapia mais personalizados. A componente de intervenção humana pode também melhorar os resultados automáticos e reforçar a credibilidade deste sistema de apoio ao diagnóstico. Mais se acrescenta que o software foi disponibilizado publicamente.

Palavas chave: Gordura epicárdica, segmentação automática, imagens de TC sem contraste, técnicas básicas de imagem, ferramenta assistida por computador.

ABSTRACT

Epicardial fat is the adipose tissue surrounding the heart, located between the myocardium and the visceral pericardium. Epicardial Fat Volume (EFV) represents a valuable predictor of cardio- and cerebro-vascular events, regardless of other risk factors. In clinical practice, the procedures to quantify EFV are mainly manual, requiring a high time cost for technicians and physicians and often involve intra- or inter-observer variances. In order to improve the repeatability of results and reduce the processing time, this thesis proposed a computer-assisted tool that automatically performs epicardial fat segmentation and volume quantification on non-contrast cardiac Computed Tomography (CT).

To this purpose, two methods were developed. Both methods prioritize the use of basic image techniques that do not require a training phase and promote lower computational complexity. The two methods performance was assessed, and the more accurate one was integrated into a prototype software (HARTA) also developed, which allows human intervention for adjustments.

A set of 20 non-contrast cardiac CT scans (878 images in total) was used to validate the algorithm. The time to segment epicardial fat on a CT was about 8.8±1.1 seconds. While for exclusively manual segmentation of one exam, 10 to 26 minutes would be required. Epicardial fat segmentation was evaluated, obtaining an accuracy of 98.83% and a Dice Similarity Coefficient of 0.7888. EFV automatic quantification presented Pearson and Spearman correlation coefficients of 0.9366 and 0.8773, respectively.

The results suggest that the proposed tool has potential to be used in clinical contexts, assisting cardiologists to achieve faster and accurate EFV, leading towards personalized diagnosis and therapy. The human intervention component can also improve the automatic results and ensure the credibility of this diagnostic support system. In addition, the presented software was made available for public access.

Keywords: Epicardial fat, Automatic segmentation, Non-contrast cardiac CT, Basic image techniques, Computer-assisted tool.

CONTENTS

LIST OF FIGURES

LIST OF TABLES

LIST OF ACRONYMS AND ABBREVIATIONS

AE	Absolute Error
AI	Artificial Intelligence
ANN	Artificial Neural Network
Ao	Aorta
CaSc	Calcium Scoring
CAT	Computed Axial Tomography
CCA	Connected Components Analysis
CCTA	Coronary Computed Tomography Angiography
CNN	Convolutional Neural Networks
CT	Computed Tomography
CVD	Cardiovascular Diseases
DICOM	Digital Imaging and Communication in Medicine
DL	Deep Learning
DSC	Dice Similarity Coefficient
EAT	Epicardial Adipose Tissue
EFV	Epicardial Fat Volume
FCM	Fuzzy C-Means
FFA	Free Fatty Acid
FN	False Negative
FNR	False Negative Rate
FP	False Positive
FPR	False Positive Rate
GT	Groundtruth
HU	Hounsfield Unit
LA	Left atrium
LV	Left ventricle
ML	Machine Learning
MR	Magnetic Resonance

PA	Pulmonary Artery
PM	Papillary Muscles
PV	Pulmonary Vein
RA	Right atrium
ROI	Region of Interest
RV	Right ventricle
SE	Structuring Element
SVC	Superior Vena Cava
TN	True Negative
TP	True Positive
UCP1	Uncoupling Protein-1
XGBoost	Extreme gradient boosting

1.

INTRODUCTION

Cardiovascular Diseases (CVD) are a leading cause of death globally and a major barrier to sustainable human development, accounting for one-third of deaths globally [1]. In recent years, there has been a significant growth in cardiovascular research to improve early diagnosis of heart diseases [2].

The heart is the most important component of the cardiovascular system since it is responsible for pumping blood to all organs and tissues of the body. The fatty layer around the outside of the heart is called the Epicardial Adipose Tissue (EAT). When associated with a pathological condition, this fat can affect the normal activity of the heart. EAT, or simply epicardial fat, is located beneath the pericardium that contacts the myocardium and coronary arteries [1], [2]

Experimental findings have reported a growing interest in epicardial fat quantification by representing a valuable predictor of cardio- and cerebro-vascular events, regardless of other risk factors [3], [4]. Epicardial fat can be assessed with different imaging techniques, among which the most validated and reproducible quantification has been obtained by using Computed Tomography (CT) due to its high spatial resolution and true volume coverage of the heart [4], [5].

Given these premises, it is necessary and valuable to precisely and non-invasively segment fat from CT scans in clinical studies to predict major adverse cardiovascular events. Nowadays, manual procedures for Epicardial Fat Volume (EFV) segmentation and quantification are still diffused in clinical practice. Technicians and physicians have to draw the pericardial contour in dozens of slices, taking 10 to 26 minutes per exam [6]–[9]. Besides the considerable time cost, manual methods involve intra- and inter-observer variances, compromising the repeatability of the results [3], [4], [10].

Therefore, to cope with the previously mentioned limitations, computer-assisted tools have been proposed for EFV quantification. Depending on the level of human intervention, these tools use automatic or semi-automatic methods. While semi-automatic methods require specialists' inputs, automatic methods can perform segmentation and quantification autonomously. It is worth pointing out that fully automated solutions might not always be suitable in clinical contexts. Human intervention is often required, so it should always be given the possibility of specialist intervention to handle unexpected events and address potential responsibilities.

1.1. Thesis Goals

This thesis arises from the need expressed by the Hospital de Santa Cruz to develop an automated method for the segmentation and quantification of epicardial fat in computed tomography images. Although methods for this purpose have already been proposed, most of them do not meet the typical needs of medical routine. The main limitations are:

- Execution times range from many minutes to hours;
- Requirement of large databases to be used in training phases (of supervised models);
- Requirement of high computational complexity;
- No open access for clinical practice and research.

Hence, this dissertation aims to develop a computer-assisted tool that overcomes the previously mentioned limitations by prioritizing basic image techniques. The hypothesis tested in this work is the following:

A method that uses basic image techniques is sufficiently accurate to semi-automatically segment and quantify epicardial fat in non-contrast CT scans and meet the needs of the medical routine.

This tool is expected to perform fully automatically. However, the term "semi-automatic" opens the possibility for specialist intervention in case of need.

In terms of clinical contributions, the development of this novel method gives cardiologists and researchers an expedited tool to achieve faster and accurate EFV, leading towards personalized diagnosis and therapy.

Several objectives were identified to achieve the overall goal outlined above:

1. Selection of basic image techniques suitable in non-contrast CT images;
2. Development of algorithms that perform automatic segmentation and quantification of epicardial fat;
3. Analysis and assessment of the developed methods;
4. Creation of a prototype software based on the achieved results.

1.2. Thesis Outline

The thesis is structured as follows:

Chapter 1: Motivation, context and main objectives of the thesis are described.

Chapter 2: Theoretical concepts introduce the transversal areas of this work: cardiovascular system, computed tomography principles and image processing.

Chapter 3: State-of-the-art of computer-assisted tools where semi-automatic and automatic methods are included.

Chapters 4: Segmentation and quantification algorithm is described, as well as the used dataset. The methodology is reported step-by-step for two proposed methods.

Chapter 5: The prototype software (HARTA) is presented in terms of the user experience and the implementation perspective.

Chapter 6: Results and discussion, where the assessment of the developed methods is analyzed, and concerns about their performances are given.

Chapter 7: Conclusion, where the achievements of this work are summarized and it is given answers for the thesis goals. The main contributions and directions for future work are also presented.

In addition, three Appendices are presented at the end of this document with some relevant information:

Appendix A: Detailed tables with metrics obtained from results.

Appendix B: General flowchart designed to guide and help readers throughout the reading of implemented methodology.

Appendix C: Basic image processing concepts are detailed to support readers understanding the main mechanisms of processing digital images.

2.

THEORETICAL CONCEPTS

This chapter empowers the reader with theoretical concepts of the transversal areas covered in this thesis. The chapter is divided into three sections. The first section is focused on the cardiovascular system, where some anatomic concepts are given. Then, the principles of computed tomography are presented and the characteristics of its images. Finally, the last section reports the main techniques used in image processing applied on medical imaging.

2.1. Cardiovascular system

In the cardiovascular system, the heart is a muscular pump that has two primary functions: (1) collect blood from the tissues of the body and pump it to the lungs; and (2) collect blood from the lungs and pump it to all other tissues of the body [11].

Concerning the internal anatomy, the heart reveals four chambers composed of cardiac muscle, called the myocardium. The two upper chambers (or atria) function mainly as collecting chambers, and the two lower chambers (ventricles) that are much stronger, pump blood.

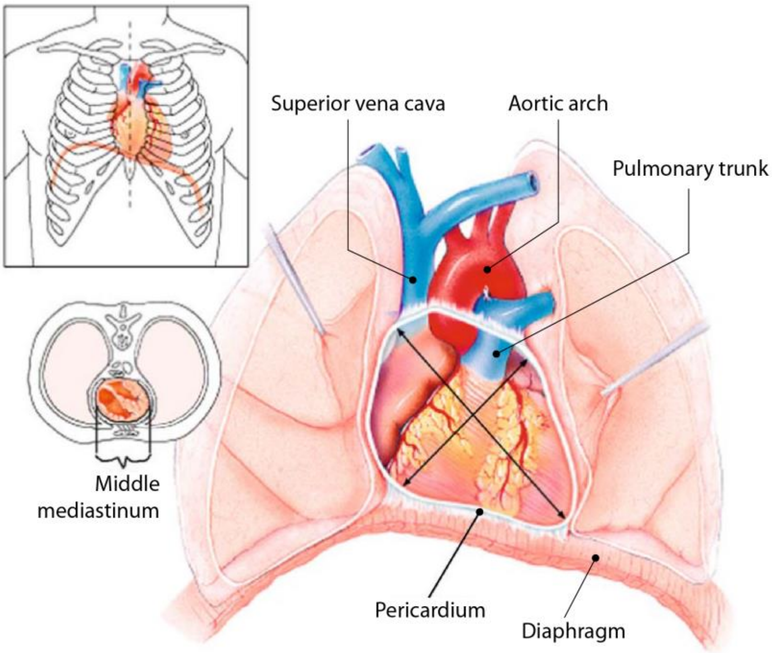

Figure 2.1 - Position of the heart in the anterior view. Adapted from Weinhaus and Roberts [11].

The human heart lies in the protective thorax, posterior to the sternum and costal cartilages, and rests on the superior surface of the diaphragm (Figure 2.1). This organ assumes an oblique position in the thorax, with two-thirds to the left of the midline. It occupies the middle mediastinum, defined as the space between the pleural cavities and inside the pericardium.

2.1.1. Heart layers

The pericardium is the covering around the heart and comprises three concentric layers. The outermost layer is the fibrous pericardium which is densely fibrous, rigid and inelastic. Inside the fibrous pericardium is the serous pericardium, which consists of two layers: the parietal layer, the outer of these which is reflected around the roots of the great vessels; and the visceral layer (epicardium), continuous with the parietal layer, that covers the internal surface of the heart and is firmly applied to it [12]. The parietal and visceral layers are separated by a space containing serous fluid, a lubricating substance. The fluid allows the inner visceral pericardium to glide against the outer parietal pericardium [11].

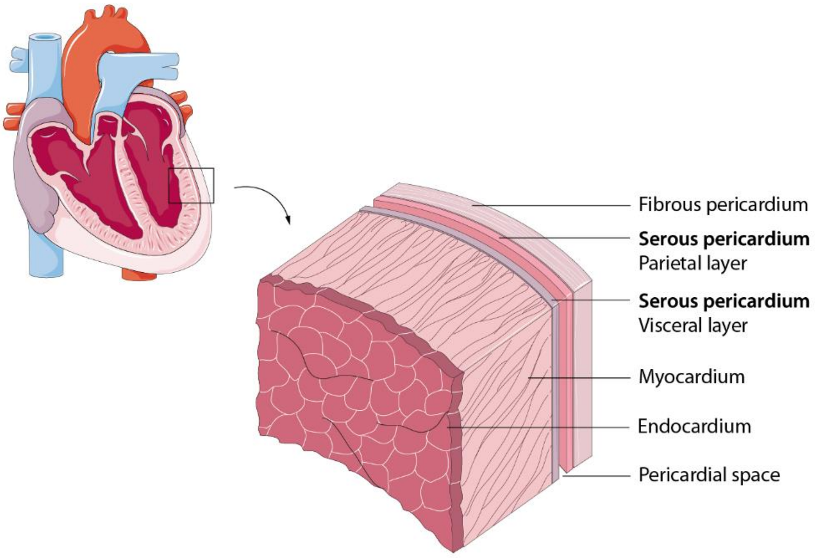

Figure 2.2 - Outermost layers of the heart. Adapted from Wong et al. [13]

2.1.2. Epicardial fat

Epicardial adipose tissue (EAT), or simply epicardial fat, is defined as adipose tissue surrounding the heart, located between the myocardium and the visceral pericardium (Figure 2.2). Epicardial fat should be distinguished from paracardial fat and pericardial fat. Pericardial fat is the adipose tissue situated external to the parietal pericardium, while pericardial fat is often defined as paracardial fat plus all adipose tissue located internal to the parietal pericardium. These later regions of fat are very close to each other and only the pericardium, a very thin barrier, separates them [13]–[15].

Adipose tissue covers 80% of the human heart surface area. Anatomical studies have shown that epicardial fat is not uniformly distributed around the heart. Also, interindividual differences in fat distribution have been observed [16]. Figure 2.3 illustrates the preferential accumulation sites of epicardial fat. Fat is mainly present over the base of the heart, the atrioventricular groove, bases of the great vessels, along with the distribution of the coronary arteries and over the right ventricle, especially over the free wall (along the right border, anterior surface and at the apex) [17].

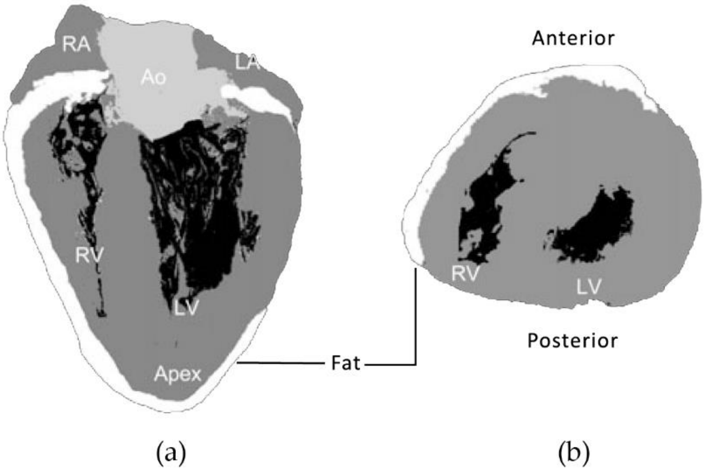

Figure 2.3 - Preferential accumulation sites of epicardial fat in four-chamber view (a) and transverse section of the heart (b). Left Atrium (LA); Right Atrium (RA), Left Ventricle (LV); Right Ventricle (RV); Aorta (Ao). Adapted from Rabkin et al. [17].

2.1.2.1. Physiological functions

The functional complexity of human epicardial fat is not fully elucidated. However, the role of this fat within the heart can be generally distinguished by the following functions [14]:

- **Mechanical functions:** Epicardial fat has compressibility and elasticity that can mechanically protect the coronary artery against excessive distortion caused by artery pulse and myocardial contraction.

- **Metabolic functions:** Epicardial fat has a higher rate of Free Fatty Acid (FFA). The energy production in the heart is highly dependent on FFA oxidation. This enrichment and increased metabolism of FFA in epicardial fat sustain myocardium energy supplies, especially during periods of high demand.

- **Thermogenic functions:** Brown adipose tissue contains mitochondria with large amounts of uncoupling protein-1 (UCP1) to generate heat in response to cold exposure. Since expressions of UCP1 are higher in epicardial fat [18], it is thought that epicardial fat could function similarly to brown adipose tissue, producing heat to protect the myocardium and coronary artery from hypothermia damage.

- **Endocrine/paracrine functions:** Growing evidence demonstrates that human epicardial fat can produce multiple bioactive cytokines. These cytokines are involved in regulating endothelial function, coagulation, and inflammation. Under normal physiological conditions, epicardial fat produces anti-inflammation or antiatherosclerotic cytokines to exert its cardioprotective functions (e.g., vasodilation, antidiabetic, antioxidative, and anti-inflammatory properties). In contrast, this fat can be harmful in disease conditions, producing inflammatory factors.

2.1.2.2. Cardiovascular diseases and risk factors

Under physiological conditions, epicardial fat protects and supports the heart to exert its normal function [14]. When associated with a pathological condition, this fat can affect the parts in which it has contact [1]. Several clinical studies have shown strong correlations between increased amounts of epicardial fat and the risk of future heart disease.

Cardiovascular diseases (CVD) are a leading cause of death and chronic disability in the world, and a major barrier to sustainable human development, accounting for one-third of deaths globally. A multifactorial etiology characterizes these diseases, and several factors simultaneously contribute to their development [19], [20].

The conditions that cause an increase in the probability of the disease onset are named risk factors. They are subdivided into modifiable, related to lifestyle changes or drugs (e.g. diet, smoking, alcohol, physical and social environments, including pollution and health systems) and not modifiable (e.g. age, sex, and genetic background) [4], [20]. There are pieces of evidence that most cases of CVD are associated with a handful of common modifiable risk factors directly related to the expansion of the fat depot surrounding the heart and coronary vessels. These risk factors for CVD include hypertension, obesity [17], diabetes mellitus, and cholesterol. Ultimately, the CVD that can develop as a result of these factors are: coronary artery calcification [21], coronary artery disease [22], coronary artery stenosis [23], myocardial ischemia [24] and atrial fibrillation [25].

Epicardial fat is emerging as an important biomarker of cardiovascular risk and a potential therapeutic target for cardiovascular disease. For this reason, it is essential to accurately and noninvasively quantify it for a given patient in clinical practice [3], [14], [16].

2.1.2.3. Imaging assessment

Detection and quantification of epicardial fat represent an important and useful clinical application, for which several imaging techniques have been developed [26]. Epicardial fat can be quantified non-invasively using echocardiography [27]–[29], Computed Tomography (CT) [2], [30] and Magnetic Resonance (MR) [31]. Although the images resulting from these exams present high resolution, some differences show a preference for each one type or another.

- **Echocardiography**

  This imaging modality is the most accessible and affordable to assess epicardial fat. Standard 2D echocardiographic methods are often used to measure the epicardial fat thickness. However, as this technique provides a linear measurement, it might not accurately reflect the epicardial fat volume.

As a matter of a fact, in echocardiography, epicardial fat and pericardial fat are often difficult to distinguish. In many instances, the thickness reported is regarding pericardial fat rather than epicardial fat. Therefore, in this imaging modality, pericardium and its borders cannot always be clearly visualized, which makes this method inaccurate for quantifying epicardial fat exclusively [32].

An example of an echocardiography image used to measure epicardial fat thickness is shown in Figure 2.4-a.

- **Magnetic resonance**

  Cardiac MR offers excellent spatial resolution and is considered the "gold standard" for imaging adipose tissue. In contrast to CT scanning, MR is not limited by ionizing radiation hazards. However, this exam is more costly and often less available than other modalities [1], [32]. In Figure 2.4-b, epicardial fat is marked in an image of MR.

- **Computed tomography**

  This imaging technique provides a true volumetric visualization and quantification of cardiac fat. Compared with other imaging modalities, CT provides a more accurate assessment of fat tissue due to its higher spatial resolution. A CT examination makes it possible to evaluate thickness, area, and volume, besides allowing the evaluation of the coronary arteries in the same exam [32]. A critical disadvantage of CT is that the exposure to ionizing radiation may limit the use, particularly if serial (follow-up) assessments are desired [13]. In Figure 2.4-c, epicardial fat is marked in a CT image.

  In fact, during the latest years, CT has been the most validated and reproducible quantification of epicardial fat. [4], [13].

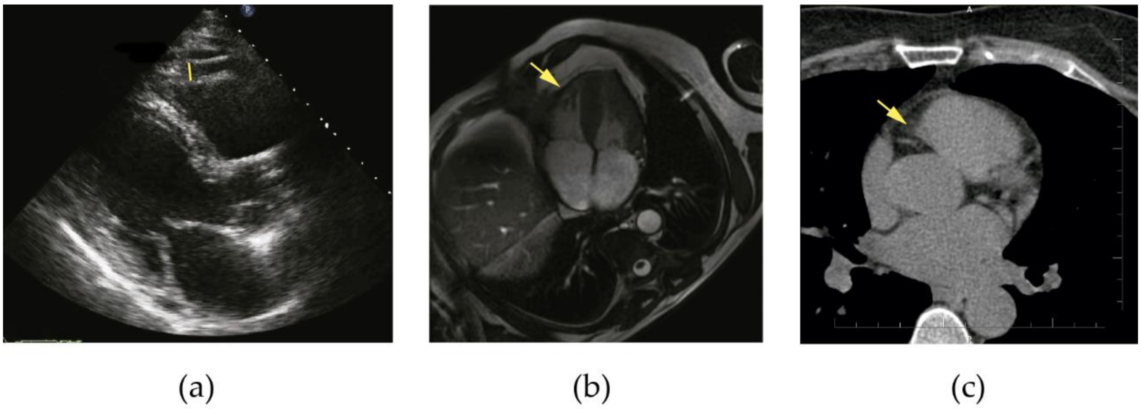

Figure 2.4 - Images of non-invasive imaging techniques for epicardial fat assessment. Echocardiography (a) with marked epicardial fat thickness. Cardiac magnetic resonance (b) and computed tomography (c) images. The yellow arrows indicate epicardial fat.

2.2. Computed Tomography

Computed Tomography (CT) scan is an imaging modality which uses X-rays to obtain structural and functional information about the human body. X-rays are electromagnetic waves and are used in diagnosis due to the property that all matters and tissues differ in their ability to absorb x-rays [33]. The CT scanner provides images in cross-sections of high quality, giving results with great accuracy [34].

During a Computed Axial Tomography (CAT) or simply Computed Tomography (CT) scanning, the x-ray source is moved in increments around the patient. The x-ray tube is turned on at each position, and the patient is exposed to a fan-shaped beam of x-rays. The fan beam is shaped by a collimator placed between the tube and the patient. The detector array registers the x-rays that pass through the patient's body, measuring their attenuation [34]. This data (attenuation and location) is then used to reconstruct a tomographic (3D) image.

The process of smearing back the projections across the image at the angle it was acquired is called backprojection. Figure 2.5 is a representation of this process. In backprojection, the data acquired by the detector are used to create multiple transaxial (or axial) slices [35]. These axial images are composed of pixels representing the tissue density of the region scanned.

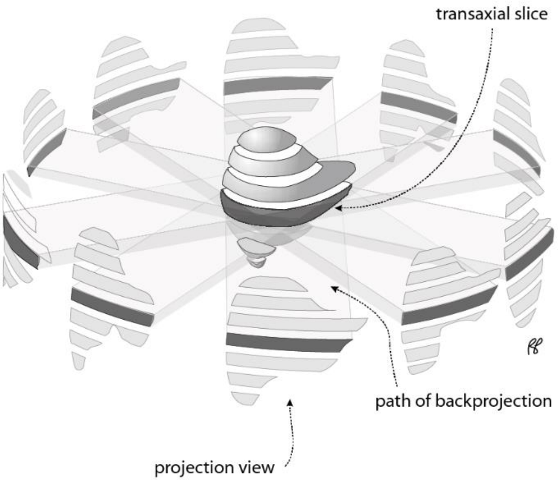

Figure 2.5 - Backprojection mechanism to create transaxial slices. Adapted from Powsner et al. [35].

Pixel is the picture element and relates to the smallest square unit of a digital image, typically arranged in a 2D grid (Figure 2.6). The image detail (or resolution) depends on the number of pixels: the more pixels present, the more closely the image resembles the scanned tissue. With computer software, multiple axial, sagittal, and coronal images can be stacked on top of each other and assembled into a 3D domain. In this case, the volume element is the voxel and, compared to the pixel, has a third dimension named pixel depth [36]. The advantages associated with this type of representation include lower computational complexity and lesser memory [33].

CT is based on the principle that the density of the tissue passed by the x-ray beam is calculated by the attenuation coefficient. The linear attenuation coefficient, μ, is a property of the attenuator (i.e., the matter through which the beam passes). The thickness is usually given in centimetres, and the linear attenuation coefficient is expressed as "per centimetre". This property is greater for dense tissue (e.g., bone) than for soft tissue (e.g., fat). However, radiodensity is not easily converted to SI units, so radiology uses the Hounsfield Unit (HU) for dose calculation according to the attenuation coefficient [34].

The relation between HU and the linear attenuation coefficient is given by

$$HU = (\mu - \mu_w)/\mu_w \tag{2.1}$$

where μ is the mean linear attenuation coefficient for the pixel of interest and μ_w is the value for water.

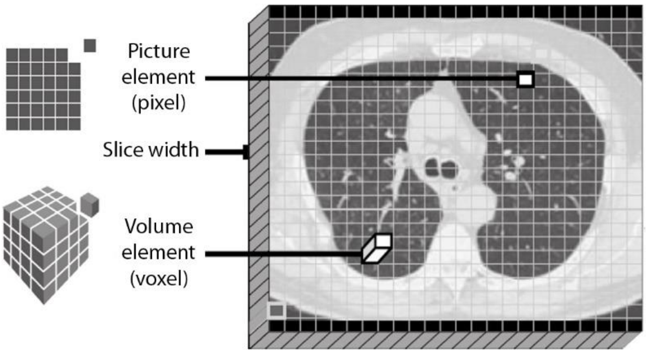

Figure 2.6 - Visual depiction of an axial slice and the structural elements of the scanned image: pixel and voxel. Adapted from Campos and Diaz [36].

2.2.1. Hounsfield unit scale

In general, the images obtained by CT have a bit-depth of 12 bits per pixel, allowing 4096 grey levels which in CT represents numbers ranging from -1000 to 3095 [15].

The HU scale (Figure 2.7) ranges between -1000 and 1000 HU. The minimum value corresponds to the air, which stops virtually no x-rays. On the other hand, the maximum value corresponds to the bone that blocks a large fraction of the beam. The middle scale (0 HU) corresponds to the water, which moderately attenuates the x-ray beam.

Translating this ability to absorb x-rays into terms of the image intensities, dense tissues such as the bones appear white on a CT film, while soft tissues such as the brain or the fat appear grey. The cavities filled with air, such as lungs, appear black.

More specifically, concerning cardiac tissues, the pericardium has a mean of -13 HU and a standard deviation of 31 HU. The cardiac muscle has a mean of 38 HU and a standard deviation of 23 HU. Although an interval around -100 HU can access the human body's fat, cardiac fat tends to register lower intensity values, reaching up to -200 HU [15], [37].

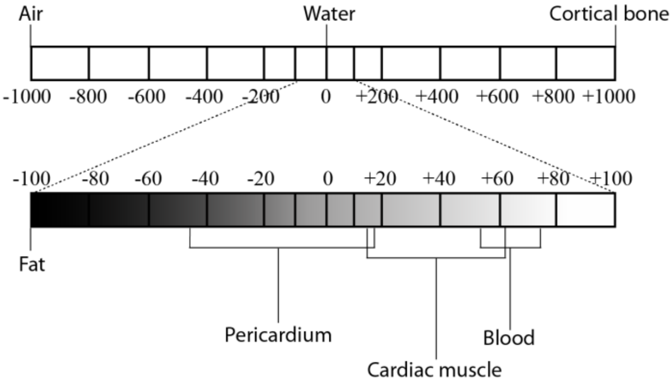

Figure 2.7 - Hounsfield Unit (HU) scale highlighting the cardiac tissues intensities' ranges. Adapted from Barbosa et al. [15].

2.2.2. Axial image interpretation

On an axial chest CT image, some anatomical structures' localization allows for a better image interpretation. Figure 2.8 shows three axial chest CT slices obtained through different levels of the heart. The images (a), (b) and (c) represent the superior, valvular and inferior levels, respectively.

In general, the right chambers (atrium and ventricle) form the heart's right lateral and anterior borders. In contrast, the left chambers (atrium and ventricle) constitute the posterior and left lateral borders.

The superior level corresponds to the major vessels of the heart: aorta (Ao), the pulmonary artery (PA), the superior vena cava (SVC) and the inferior vena cava. The valvular level comprises the chambers of the heart - right atrium (RA), left atrium (LA), right ventricle (RV) and left ventricle (LV) -, and structures like pulmonary veins (PV). Finally, the inferior level comprises the heart's papillary muscles (PM) located in the ventricles near the apex. The intraventricular septum is also visible.

In each level, the pericardium is seen as a single line surrounding the heart with a thickness of fewer than 2 millimetres.

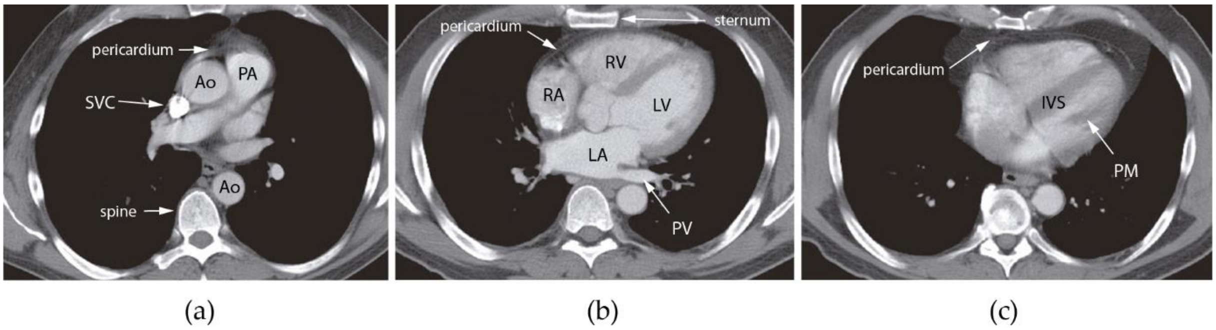

Figure 2.8 - Heart anatomy in chest contrast-enhanced computed tomography images from superior (a), valvular (b) and inferior (c) levels. Adapted from Kanza et al. [38]

2.2.3. Contrast resolution

The contrast resolution of CT is not intrinsically high because the difference in x-ray attenuation between different tissues is generally small, leading to low soft tissue contrast and the need for contrast agents. The primary way to increase contrast resolution on CT is to administer intravenous iodinated contrast. Iodine has a linear attenuation coefficient higher than the tissues. Thus, the areas with a high concentration of this agent present a higher attenuation and, consequently, a higher contrast relative to surrounding structures [39]. In Figure 2.9, it is possible to see that for a given x-ray energy comprised in the typical CT x-ray energy range, the linear attenuation coefficient of iodine is vastly superior to those of tissues without this contrast agent.

When contrast medium is used, structures like the coronary arteries, valves, papillary muscles, interatrial and interventricular septa, and other heart structures that were not clearly identifiable on unenhanced CT, become visible [38].

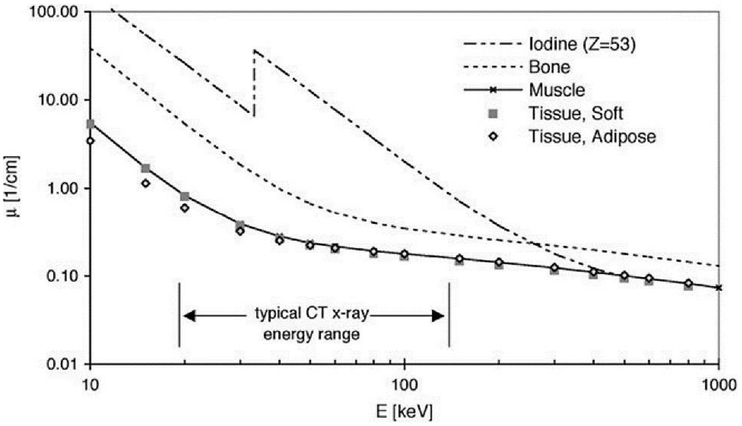

Figure 2.9 - Linear attenuation coefficient versus x-ray energy. From Lin et al. [39].

Figure 2.10 illustrates the difference between a non-contrast and a subsequent obtained contrast-enhanced image. In fact, the contrast resolution improves significantly with an intravenous contrast agent. Nevertheless, the need for intravenous contrast depends on the specific clinical indication. Contrast enhancement not only remarkably affects the CT image quality but also increases the total radiation dose to which the patient is exposed. For this reason, the benefits of contrast should be weighed against the potential risks in each patient [40].

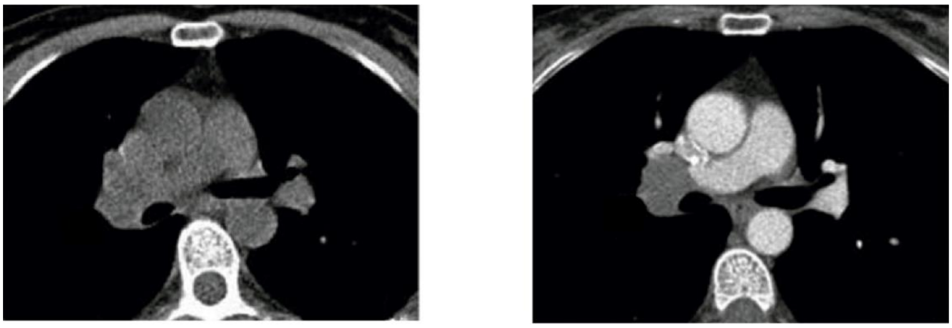

(a) (b)

Figure 2.10 - Cardiac CT images with non-contrast (a) and with contrast-enhancement (b). Adapted from Purysko et al. [41]

2.2.4. Clinical applications

Nowadays, CT offers important anatomic information about the number, size, and locations of tumours. Besides the non-contrast and contrast-enhanced CT previously discussed, the following types of CT scans are also used to diagnose heart diseases.

- **Calcium Scoring**

  Cardiac CT for calcium scoring (CaSc CT) is used to detect calcium deposits based on the radiographic density-weighted volume of plaques with attenuation values greater than 130 HU. These deposits represent brighter areas in CaSc CT images, as Figure 2.11 shows. The presence of coronary calcification is a robust predictor of adverse cardiovascular events as atherosclerosis or coronary artery disease. This technique constitutes a safe diagnosis exam as no contrast is required, and radiation doses are negligible [42], [43].

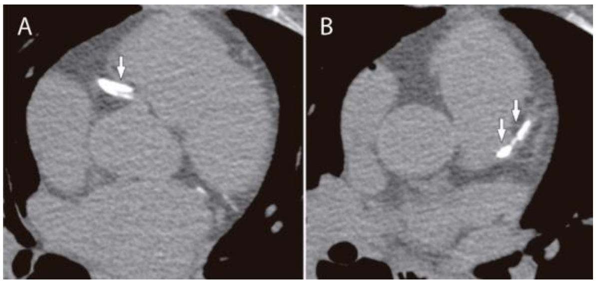

Figure 2.11 - Computed tomography for calcium scoring scan (CaSc CT). Arrows indicate severe calcifications in the proximal right coronary artery (A), and left anterior descending artery (B). Adapted from Hamilton et al. [42].

- **Coronary Computed Tomographic Angiography**

Coronary CT angiography (CCTA) is also a non-invasive heart imaging exam used in the 3D visualization of the coronary arteries. CCTA involves a venous injection of an iodine-based contrast agent. In many centres, CaSc CT is performed before CCTA to provide quantitative risk assessment and better planning of the CCTA acquisition, although with the penalty of mildly increased radiation exposure.

This technique generates high-resolution images in axial, multi-planar and volume-rendered reconstructions of the moving heart and great vessels. The several plans and reconstructions help to determine if either fatty or calcium deposits have built up in the coronary arteries [42], [43]. Figure 2.12 illustrates some images extracted from this type of examination.

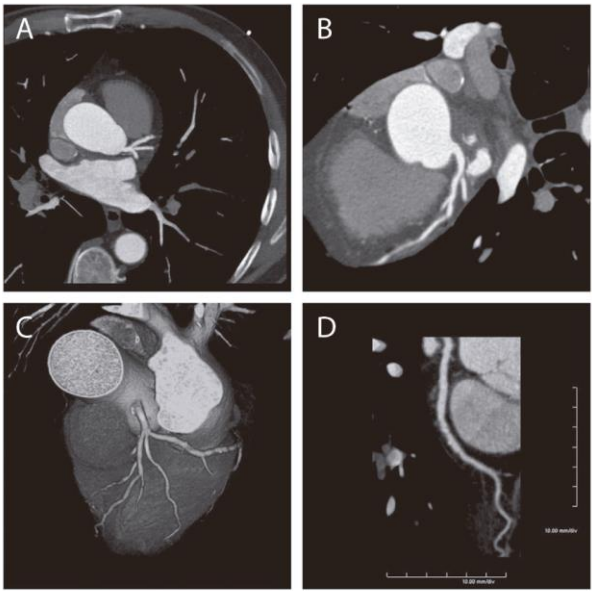

Figure 2.12 - Coronary Computed Tomographic Angiography (CCTA) reconstructions: axial image (A); multiplanar reconstructed image (B); anatomic 3D volume-rendered image; and curved multiplanar reconstruction (D). Adapted from Prat-Gonzalez et al. [43].

2.2.5. Digital storage

There are more than 100 images format types. Depending on the purpose of the data, some format types are more appropriate than others. Digital Imaging and Communication in Medicine (DICOM) is a standard format for encoding and transmitting medical CT and MR data. This format has become a central standard in radiology and is increasingly used in other medical fields.

DICOM files store the image information along with other data, including patient details and acquisition parameters. The list of attributes is contained on the descriptive "header", specifying the type of the object, patient data, and other information such as performed procedures or reports.

In the DICOM header, the data are divided into several groups (or tags), and each one has a well-defined meaning. For example, group 10 (0010, …) is reserved for patient data, group 18 (0018, …) presents details about the image acquisition technique, and group 28 (0028, …) contains data about image properties [44], [45]. Figure 2.13 shows a sample of a DICOM header containing these three groups. Some illustrated tags, including the slice thickness (0018, 0050) and pixel spacing (0028, 0030), are crucial in medical image segmentation and volume quantification, as will be seen further.

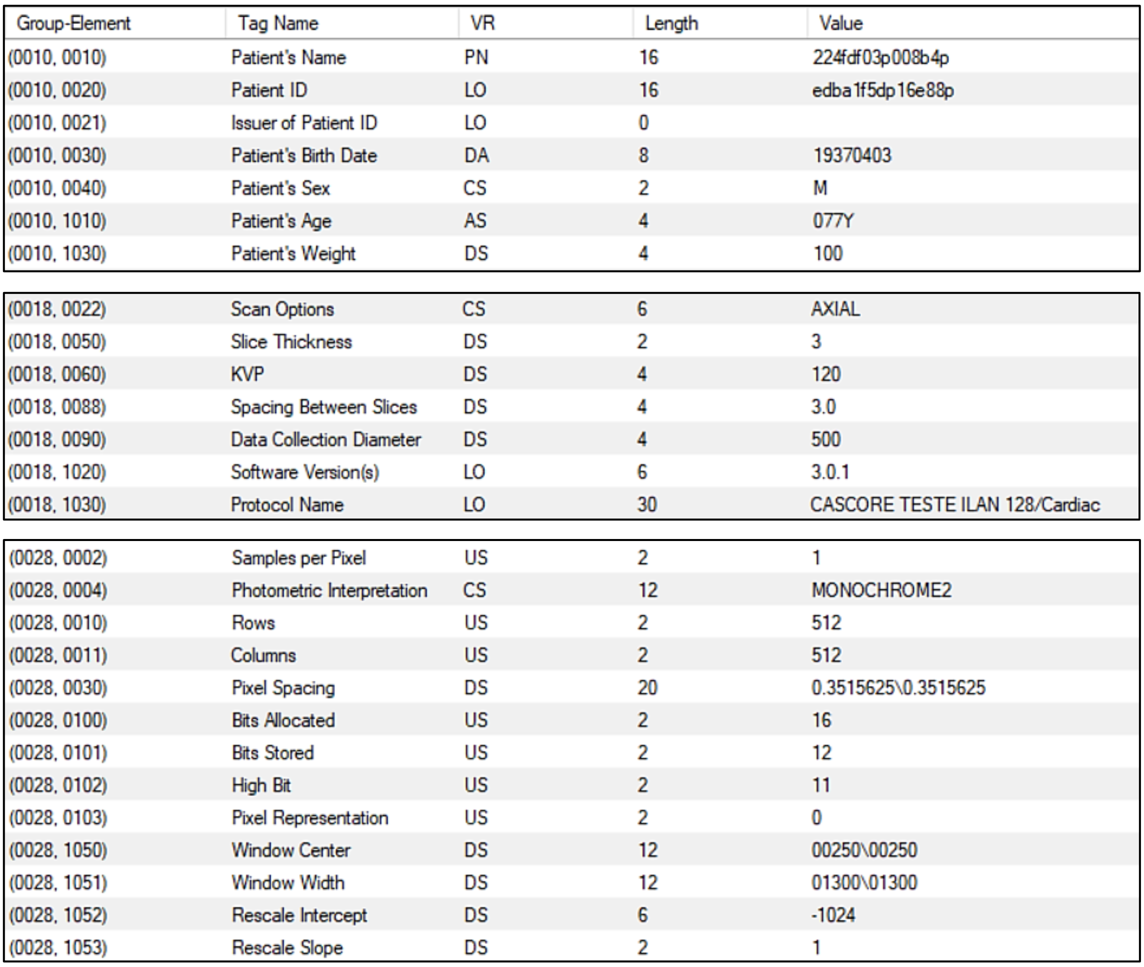

Group-Element	Tag Name	VR	Length	Value
(0010, 0010)	Patient's Name	PN	16	224fdf03p008b4p
(0010, 0020)	Patient ID	LO	16	edba1f5dp16e88p
(0010, 0021)	Issuer of Patient ID	LO	0	
(0010, 0030)	Patient's Birth Date	DA	8	19370403
(0010, 0040)	Patient's Sex	CS	2	M
(0010, 1010)	Patient's Age	AS	4	077Y
(0010, 1030)	Patient's Weight	DS	4	100
(0018, 0022)	Scan Options	CS	6	AXIAL
(0018, 0050)	Slice Thickness	DS	2	3
(0018, 0060)	KVP	DS	4	120
(0018, 0088)	Spacing Between Slices	DS	4	3.0
(0018, 0090)	Data Collection Diameter	DS	4	500
(0018, 1020)	Software Version(s)	LO	6	3.0.1
(0018, 1030)	Protocol Name	LO	30	CASCORE TESTE ILAN 128/Cardiac
(0028, 0002)	Samples per Pixel	US	2	1
(0028, 0004)	Photometric Interpretation	CS	12	MONOCHROME2
(0028, 0010)	Rows	US	2	512
(0028, 0011)	Columns	US	2	512
(0028, 0030)	Pixel Spacing	DS	20	0.3515625\0.3515625
(0028, 0100)	Bits Allocated	US	2	16
(0028, 0101)	Bits Stored	US	2	12
(0028, 0102)	High Bit	US	2	11
(0028, 0103)	Pixel Representation	US	2	0
(0028, 1050)	Window Center	DS	12	00250\00250
(0028, 1051)	Window Width	DS	12	01300\01300
(0028, 1052)	Rescale Intercept	DS	6	-1024
(0028, 1053)	Rescale Slope	DS	2	1

Figure 2.13 - Example of a DICOM image header showing different groups (or tags) and some of their elements: patient-related, acquisition technique and image-related data, in this order.

2.3. Image Processing

Digital imaging plays an important role in some medical practices, mainly studying anatomy and physiology abnormalities of internal organs. The manipulation of images using digital computers is called image processing, and its use has been increasing exponentially in the last decades [46].

Basic concepts of digital image processing are provided in Appendix C. The present section addresses more complex concepts, including image registration, image segmentation and performance metrics to evaluate segmentation methods.

2.3.1. Registration

Image Registration is a computationally expensive task that involves deforming an image, using a suitable deformation model, until it is similar to another image. This method aims to find the optimal transformation that produces the best alignment between the input images. The input for this process includes two images: the original image, which works as the reference, known as the fixed image; and the image to be aligned with the fixed image, known as the moving image.

Remote sensing, medical imaging and computer vision are some applications of this method. In particular, image registration is a crucial step in medical imaging analysis since it is necessary to compare images from different sensors or modalities (multimodal analysis), different viewpoints (multiview analysis) or even acquired at different times (multitemporal analysis) [47].

The research in medical image registration has frequently been increased mainly by the extended utilization of medical diagnostic devices, growing trust in medical diagnostics based technologies, and rapid development of low-cost computing and imaging technologies. During this evolution, image registration has been widely applied to diagnosis, staging, assessment of treatment response, surgery simulation, generation and comparison of atlases, anatomic segmentation, and pre- and post-contrast injection images [48].

Typically, image registration includes the following substages:

- **Similarity/Dissimilarity measure** is the first step where the input images are compared to each other to measure their similarity [48]. A similarity measure quantifies the degree of alignment between the overlapped regions of the input images. The methods for the alignment measure depends on the image information. Hence, measures can be intensity-based, when obtained in terms of intensity levels, or feature-based, when related to shapes, edges and landmarks. The effective measurement must resist the noise and background changes [47].

- **Point detection and extraction** are the following steps. *Point detectors* are applied to describe the key points that carry critical information about the images. The detected points should be independent of noise, blurring, contrast, and geometric changes. After detecting the control points, the next step is to extract the ones that represent the critical information in the processed images. The *extracted points* could be simple, like statistical points (e.g., mean and variance) or more sophisticated (e.g., texture points). Regardless of the type, extracted points must guarantee the following characteristics: distinction to the spatial neighbours, invariance to the original image variations, robustness against noise, computational efficiency, and comparability to facilitate the detection of corresponding points in other images [48].

- **Image descriptors** are then used to represent the extracted critical points that better help measure the images' similarity. All critical information and other content information are included in the image description. The aim is to facilitate the accessibility of the visual queries apart from the image content [48].

- **Point selection** step is responsible for decreasing the number of the extracted points. The selected points must have two characteristics: they must be independent of each other to avoid redundant information; they must provide complete information about the recognized objects to ensure the least ambiguity in distinguishing them [48].

- **Point pattern matching** methods are then applied. These methods establish a correspondence between the key points of the images. The objective is to determine the correct and incorrect matches. For instance, some key points can be outliers or slightly displaced from their true positions due to noise [48].

- **Robust parameter estimation and transformation functions** are applied as the next step. These functions use the correspondences of the key points for estimating the transformation functions' parameters used in the image registration. The transformation function is responsible for optimising (i.e. minimising or maximising) the similarity measure between the input images when applied to the moving image [47]. The choice of the transformation function depends on the nature of the images to be registered [48].

- **Image resampling and compositing** are the last registration step. In image resampling, the fixed image is scanned and, for each point, the corresponding point in the moving image is determined. Several methods have been evolved to estimate the required coordinates. In general, speed and accuracy are the main key factors to evaluate the performance of these methods. Finally, the composition stage combines the registered images into a larger image named a composite image [48].

Composite images can still undergo a fusion process. Image fusion consists of merging several composite images into a single output image containing a better description of a scene (or object) than any input image. The ultimate benefit is the quality of the information contained in the fused image [48].

Otherwise, the composite images can be compared with other composite images (without being fused) to evaluate the performance of several image processing methods, such as segmentation.

2.3.2. Segmentation

Segmentation is the process of dividing an image into regions with similar properties such as grey level, colour, texture, brightness, and contrast. The role of segmentation is to subdivide the objects in an image. For instance, in medical images, segmentation aims to identify a region of interest (ROI) or measure a tissue volume (e.g., tumour) to track its growth [33].

Considering the domain of the medical image is given by Ω, the segmentation problem is based on discovering the sets $S_i \subset \Omega$ ($i \leq k$, where k is the number of classes). Consequently, the sets that make up the segmentation must verify the following equation,

$$\Omega = \bigcup_{i=1}^{k} S_i \tag{2.2}$$

where $S_i \cap S_j = \emptyset$ for $i \neq j$. Ideally, a segmentation method finds the sets corresponding to distinct anatomical structures or ROI. Segmentation can be applied through manual, semi-automatic or automatic methods [49].

Automatic segmentation of medical images is a difficult task as medical images are complex and rarely have any simple linear feature. Although the number of algorithms proposed in this field, medical image segmentation continues to be a challenging problem. Several surveys were published in order to classify medical image segmentation algorithms [33], [49], [50]. This section explores the main image segmentation methods as well as the evaluation metrics used to assess their performance.

Overall, the segmentation methods can be grouped into three main groups: based on grey level features (threshold-based, edge-based, region-based), based on models and based on artificial intelligence methods (supervised and unsupervised). Figure 2.14 depicts each segmentation group.

This section briefly describes each segmentation method, further detailing the most commonly used CT image segmentation methods: threshold- and region-based; deformable models; fuzzy C-means; artificial neural networks [33].

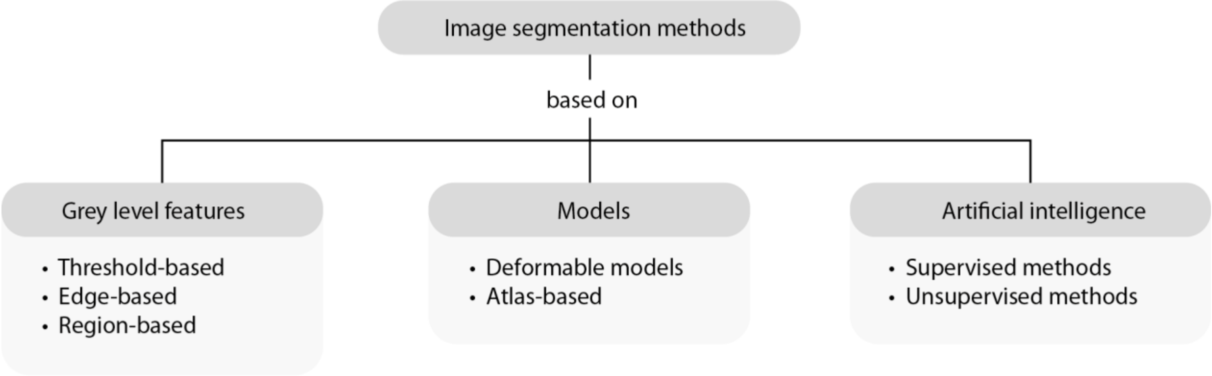

Figure 2.14 - Image segmentation methods.

2.3.2.1. Based on grey level features

The methods based on grey level features have pixel intensity as the main feature to perform segmentation. Threshold-based, edge-based and region-based are methods that use these fundamentals. Figure 2.16 shows an image output for each method presented below.

Threshold-based

The threshold-based segmentation method is the simplest and fastest method based on the hypothesis that different structures representing organs or tissues have different intensity levels [33]. This technique attempts to determine an intensity value, called the threshold, which separates the desired structures (or classes). The segmentation is then achieved by grouping all pixels with intensities greater than the threshold into one class and all other pixels into another class [49]. Mathematically the threshold can be defined as follows,

$$g(x,y) = \begin{cases} 1, & f(x,y) \geq T \\ 0, & f(x,y) < T \end{cases} \tag{2.3}$$

where $g(x,y)$ is the resulting pixel at coordinate (x,y), $f(x,y)$ is the pixel of the input image and T is the value of the threshold. These two classes are often designed as "foreground" (classified as 1) and "background" (classified as 0), where the first is the segmentation of a specific structure. For multiclass segmentation, several thresholds must be defined [33], [49]. In general, the threshold-based method is especially applicable in high-contrasted images with well-defined structures and significantly homogeneous intensities [15].

The thresholds are frequently determined using the image histogram, with the diverse peaks and valleys that enable the division of images into different regions [33]. Figure 2.15 denotes bimodal and multimodal histograms, where the valleys represent one and two potential thresholds, respectively. These values can be selected manually or automatically. Manual selection needs *a priori* knowledge and sometimes trial experiments, while the latter combines the image information to automatically get the adaptive threshold values [50]. For example, Otsu's method obtains the threshold by calculating the value that maximizes the separation between different threshold classes [51].

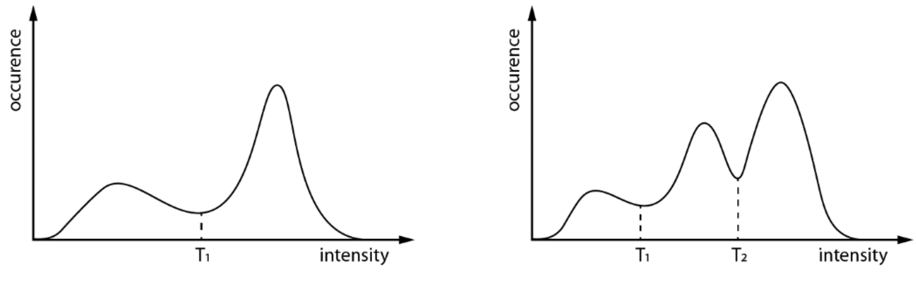

(a) (b)

Figure 2.15 - Bimodal (a) and multimodal (b) image histograms, suggesting two and three potential classes, respectively.

Edge-based

Edge-based segmentation methods separate images into distinct regions by detecting edges (or boundaries). An edge can be defined as the separation between two areas with distinct intensity or grey levels [33].

The image edges are detected by computing the gradient image with derivative (or gradient) filters. In these methods, the threshold values are associated with the edge information, i.e., considering the filter output, the pixels are classified as edge or non-edge. The pixels that are not divided by an edge are assigned to the same category [52].

Since the operations of the algorithms are based on pixel intensities, the detected boundaries consist of discrete pixels that may be incomplete or discontinuous. For a complete segmentation, this technique is usually conjugated with region-based methods or morphological operations that connect the breaks or eliminate the holes [50].

The number of detected edges depends on the gradient (derivative) function. For instance, Prewitt, Sobel, Roberts (first derivative type) and Laplacian (second derivative type), Canny, Marr-Hilclrath Edge Detector are gradient filters often used.

The main limitation of edge-based methods is the poor performance in the presence of noise, generating fake or weak edges [33].

Region-based

Region-based methods are according to the principle of homogeneity, i.e., the pixels with similar properties are clustered together to form a homogenous region.

The region growing algorithm is a typical example of a region-based method. Region growing is a technique for extracting an image region based on predefined criteria. These criteria can be related to intensity information or edges in the image. An operator manually selects a seed point, and all the pixels connected to the initial seed are extracted based on the predefined criteria. For each region needing to be extracted, a seed must be planted [33].

The main disadvantage of region growing is the manual interaction to obtain the seed point [49]. In order to remove the manual dependence on initial seeds and make the algorithm automatic, *a priori* knowledge and statistical information can be incorporated into the algorithms [53], [54].

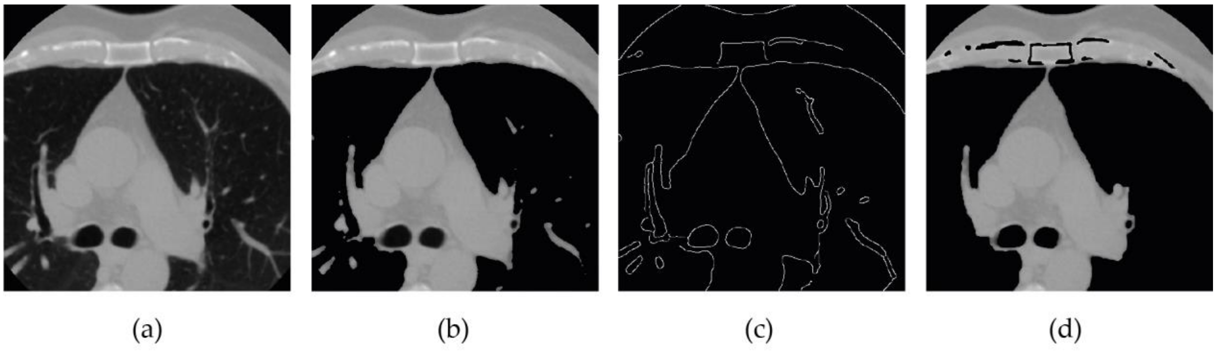

(a) (b) (c) (d)

Figure 2.16 - Image segmentation methods based on grey level features. Original CT image (a); Threshold-based method output (b); Edge-based method (Canny Edge Detector) output (c); Region-based method output (d).

2.3.2.2. Based on models

The methods based on models have a previous template or model which works as a reference and facilitates the segmentation process. Deformable models and atlas-based are methods that use these fundamentals.

Deformable models

Deformable models have been widely used in medical imaging segmentation. The basic approach of this technique is that the organs' structure has a repetitive form of geometry and can be modelled probabilistically for variation of shape.

This method delineates a ROI by using closed parametric curves or surfaces that deform under the influence of internal and external forces. Firstly, a closed curved must be placed near the desired (organ) boundary and then allowed to undergo an interactive relaxation process [49]. The internal forces are computed from within the curve or surface to keep it smooth during the deformation process. On the other hand, the external forces are usually derived from the image to drive the curve or surface toward the desired feature of interest.

The main disadvantage of this technique is the requirement of manual interaction to place an initial model and choose appropriate parameters. Also, the standard deformable models frequently do not exhibit a satisfactory convergence to concave boundaries [33].

Atlas-based

Atlas-based approaches are a powerful tool for segmentation medical images when a standard atlas or template is available. The atlas is generated by compiling information on the anatomic structure desired to segment (e.g., shape, size, type of tissue that composes the organ). This atlas is then used as a reference for segmenting new images.

These approaches are similar to correlation approaches with the plus point of performing segmentation and classification simultaneously. The process involves finding a one-to-one transformation that maps a pre-segmented atlas image to the target image that requires segmenting. This process is defined as "atlas wrapping".

Atlas-based approaches face limitations in the segmentation of complex structures with variable shape, size and other properties that require expert knowledge in building the database to generate the atlas. Thus, these approaches are generally better suited for the segmentation of structures that are stable over the population of study [33], [49]. One method that considers anatomical variability is probabilistic atlases [55], albeit requiring additional time and interaction to accumulate data. Another method is the use of manually selected landmarks to constrain transformation [56].

2.3.2.3. Based on artificial intelligence

The methods based on artificial intelligence algorithms are grouped into supervised and unsupervised methods. Supervised methods require operator interaction during the segmentation process, while unsupervised methods generally require operator involvement only after the segmentation is finished.

Supervised methods

Artificial Neural Network (ANN) algorithms are widely used in these methods. An ANN algorithm is inspired by the way biological nervous systems process information. It is an information processing system that contains a large number of interconnected processing neurons. These neurons work together in a distributed manner to learn from the input information $(x_1, x_2, \dots, x_n)$, coordinate internal processing, and optimise the final output (Y). The basic structure of a neuron can be theoretically modelled, as Figure 2.17 illustrates.

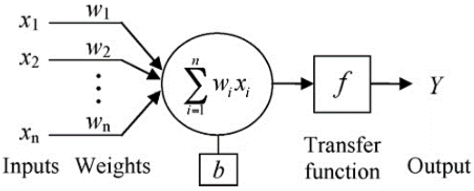

Figure 2.17 - The model of a neuron. From Jiang et al. [57]

Each input is multiplied by its weight w_i, a bias b is associated with each neuron, and their sum goes through a transfer function f. The relationship between input and output can be described by equation 2.4 [57].

$$Y = f\left(\sum_{i=1}^{n} w_i x_i + b\right) \tag{2.4}$$

Numerous algorithms have been reported in the literature applying neural networks to medical image segmentation. The most widely applied use is as a classifier, in which the weights are determined from manually segmented training data (i.e., labelled images). Taking the labelled images as reference, the ANN is then used to segment new data. In the training phase, comprehensive data sets are crucial so the ANN can learn from a diverse and large number of cases.

Although ANNs are inherently parallel, their processing is usually simulated on a standard serial computer, requiring high potential computational complexity [49].

Unsupervised methods

Most of the unsupervised algorithms are based on clustering techniques. Clustering algorithms essentially perform the same function as classifier methods without depending on the training phase and the training data. The clustering process consists of finding natural grouping clusters in multidimensional feature space based on an adequate rule [33].

The two commonly used algorithms for clustering are K-mean and Fuzzy C-means.

- **K-mean** splits the image into k sections based on the mean of each section. The data is firstly divided into k clusters, and the mean of each cluster is calculated. Each point is allocated into the cluster that presents the nearest distance to the cluster's mean using the euclidean distance.

- **Fuzzy C-means** (FCM) is one of the suitable clustering methods for medical image segmentation. The FCM generalizes the K-means algorithm, allowing an object belonging to different clusters. This property results in a soft segmentation, overcoming boolean boundaries that are often not natural or event counterintuitive [58].

These algorithms consume less time than supervised methods since they do not require the training phase. However, as a disadvantage, they do not consider spatial information, being sensitive to noise and intensity inhomogeneities [59].

2.3.3. Performance metrics

Some algorithms achieve better performance than others, depending on the image type and their purpose. The performance evaluation of segmentation methods is crucial to assess their accuracy. Several metrics can be used in this evaluation. However, two metrics are often used to evaluate segmentation methods: accuracy and dice similarity coefficient.

Both metrics can be easily retrieved from the confusion matrix, a fundamental concept in classification problems. The confusion matrix, shown in Figure 2.18, provides a tabular view of the method's predictions against the true labels.

		Predicted class	
		Negative	*Positive*
True class	*Negative*	True negatives (TN)	False positives (FP)
	Positive	False negatives (FN)	True positives (TP)

Figure 2.18 - Confusion matrix for a binary classification problem.

Accuracy can be described as the fraction of predictions the model got right. For binary classification, the number of correct predictions corresponds to the sum TP + TN.

$$Accuracy = \frac{TP + TN}{TP + TN + FP + FN} \tag{2.5}$$

Sometimes, to get more information about the segmentation type errors, the FP and FN rates are often calculated. FP corresponds to type I error, while FN corresponds to type II error. FP rate (FPR) is defined as the probability of falsely rejecting the null hypothesis.

$$FPR = \frac{FP}{FP + TN} \tag{2.6}$$

Complementarily, FN rate (FNR) is defined as the probability of falsely not rejecting the null hypothesis.

$$FNR = \frac{FN}{FN + TP} \tag{2.7}$$

The Dice Similarity Coefficient (DSC), also called overlap index, is the most used metric in validating medical volume segmentation [60]. This metric measures the spatial overlap between automatic segmentation, S_A, and ground truth (or manual) segmentation, S_M [61]. DSC varies between 0 and 1, where 1 indicates a total overlap. The values can also be presented as a percentage. Given the two segmentations S_A and S_M, DSC is defined as

$$DSC = \frac{2(S_A \cap S_M)}{S_A + S_M} \tag{2.8}$$

Since the region containing "true positives" is defined as $TP = S_A \cap S_M$, DSC can also be defined as follows

$$DSC = \frac{2TP}{2TP + FP + FN} \tag{2.9}$$

The metrics previously presented are the most commonly used to evaluate the performance of segmentation methods with the same purpose of this thesis, as will be verified in the next chapter.

3.
STATE OF THE ART

In the literature, several methods have been proposed to automate epicardial fat segmentation and quantification. These methods differ in the medical images they are applied to, the automation level, the processing time, and the number of patients used for testing and validation.

This chapter presents the evolution of computer-assisted tools over time, where the methodologies are grouped by semi-automatic and automatic methods. The main studies are described as well as their outcomes.

3.1. Manual methods

In current clinical practice, epicardial fat quantification studies were limited to manually outlined region of interest (ROI) and preset fat attenuation thresholds. In manual procedures, the specialist has to insert several points along the pericardium to separate the heart from other structures such as lungs, aorta, and bones and repeat the same process in dozens of slices that composes one CT exam [5], [62]. Figure 3.1 shows a manual pericardium delineation on a contrast-enhanced CT image.

Figure 3.1 - Manual delineation of the pericardium as the region of interest (ROI).

The workload and time-cost of manually segmenting and quantifying epicardial fat are very high for technicians and physicians [63]. Manual and subjective quantifications often involve significant intra- or inter-observer variances due to the difficulty of correctly identifying the area among multiple observers. Human limitations contribute to this, including physical tiredness, fatigue, and the repetitiveness of actions. Errors in the fat quantification step can affect the analysis of the specialist and result in an inaccurate diagnosis [1], [4]. To overcome inaccurate hand-segmentation and all inherent limitations, semi-automatic and automatic methods have been proposed.

3.2. Semi-automatic methods

In 2005, Pednekar et al. [64] proposed a method to segment abdominal adipose tissue. One year later, Bandekar et al. [65] further extended the method introduced by Pednekar et al. [64], having adapted it to segment epicardial fat. This first semi-automated segmentation method was based on a hierarchical segmentation, feature extraction, and fuzzy affinity-based framework. This method requires a training phase with 23 exams to extract features, mainly pixel intensity and texture. Although the accuracy of (99.13 ± 0.38)% was achieved, this method took about 1 minute per slice.

Dey et al. [16] (2008) proposed a semi-automatic method where manual intervention is required to determine upper and lower transverse slices containing the heart. After this step, all operations were fully automatic with a recursive 3D region-growing algorithm performing the segmentation. This work used a more extensive database of 105 exams. The results reported an execution time of 20 ± 4 seconds per exam (after the slice limit selection step) and a Spearman correlation coefficient of 0.98. However, the authors did not provide information about the segmentation performance.

Later in 2011, Barbosa et al. [21] presented another semi-automatic method with the preprocessing step proposed by Dey et al. [16] coupled with a pericardium delineation step. The delineation was covered by tracing lines from the heart's centroid to the pericardium layer and interpolating them using cubic interpolation. The methodology was tested in 40 exams, and a success rate of 52.5% (21/40 cases) was reported. Additional evaluation metrics about quantification or segmentation performance are not mentioned by the authors.

Coppini et al. [18] (2010) used a region growing strategy and a pre-processing step to remove all thorax structures apart from the heart. Human intervention was required to scroll the slices between the atrioventricular sulcus and the apex to place control points on the pericardium. The control points were used to draw the pericardium contour by a cubic spline. In contrast to the other methods previously discussed, this work was tested on 10 CT images obtained during standard calcium scoring CT (CaSc CT) studies. In this research, Coppini et al. [18] described the methodology without detailing the achieved results.

Zlokolica et al. [22] (2017) used a semi-supervised machine learning model for EFV quantification. This method was a semi-automatic slice-by-slice segmentation approach based on local adaptive morphology and fuzzy c-means clustering. Additionally, they used a geometric ellipse to post-filtering out undesired parts of the target cluster. The user was required to inspect a single CT slice and place a seed point to select the cluster corresponding to epicardial fat. The methodology was tested in 10 enhanced-contrast CT and having achieved a DSC of 69%.

3.3. Automatic methods

The first fully automatic approach for epicardial fat segmentation was proposed by Shahzad et al. [66] in 2013. They presented a multi-atlas-based method for segmenting the pericardium and calculating EFV. Eight manually segmented CT scans (atlases) from different subjects are registered. The atlases' obtained contours are converted into 3D surfaces and fused with a target patient scan to segment the pericardium. The method was tested on 98 non-contrast CT exams with a Spearman correlation coefficient of 0.91 and a DSC of (89.2 ± 9.1)%.

Using a similar approach, Ding et al. [3] (2015) proposed a hybrid algorithm based on initial segmentation with multi-atlas, followed by automated pericardium delineation using geodesic active contours. This method took about 60 seconds per exam. The authors tested their work on 50 non-contrast CT exams and achieved slightly better values than Shahzad et al. [66]: a Spearman correlation coefficient of 0.97 and a DSC of 0.92.

Similarly, Norlén et al. [67] (2016) proposed a hybrid method to detect the pericardium using the random forest classification algorithm and multi-atlas segmentation for spatial initiation in CCTA images. This approach was tested on 30 exams, having registered a Spearman correlation coefficient of 0.99 and a DSC of 0.91. The method performed each exam in approximately 51.9 seconds.

Spearman et al. [6] (2014) also proposed a fully automated 3D pericardial border definition software using a model-based approach. The model is trained on 70 manually annotated CCTA enhanced-contrast exams covering the pericardium from the ascending aorta to the end of the pericardial sac. The results reported a Spearman correlation coefficient of 0.889 and an execution time per exam of (135.6 ± 24.6) seconds. In this study, the fully automated measurements resulted in an overestimated EFV, decreasing with manual intervention. Thus, the authors concluded that a manually optimized semi-automatic approach is best suited for clinical routine.

In the studies mentioned above, the atlas-based method considers that heart shape data between the trained and the new exam are similar. However, there are anatomical variations among individuals that impose limitations to this type of approaches.

Militello et al. [4] (2019) propounded a semi-automatic method and an interactive interface that calculates EFV and fat subdivided into quartiles. This study was performed in 50 CaSc CT exams and 95 CCTA exams. The segmentation is done by double-thresholding and an interpolation step with manual and automated drawn contours. However, in the initial phase, the operator has to detect the bounding region containing the heart in at least 10 CaSc CT or 20 CCTA slices. This method achieved slightly better performance when applied in the CaSc CT datasets with a Spearman correlation coefficient of 0.9591 and a DSC of 0.9394. In the CCTA exams were reached a Spearman correlation coefficient of 0.9319 and a DSC of 0.9248.

Rodrigues et al. (2015) [68] and Rodrigues et al. (2016) [12] presented the first automatic methods using supervised machine learning algorithms to segment cardiac fat. The methodology was based on registration and classification steps. The registration was mentioned by the authors as an alternative step to optimize the problem. This process involved matching images' characteristics to search for alignments that minimize the variation between overlapping pixels [68]. The classification step followed a supervised model where each pixel is labeled with a certain class according to features extracted in training step. Specifically, each pixel can be labeled as making part of epicardial fat, mediastinal fat, pericardium or non-fat class. Despite achieving a high accuracy of 98.5% and a DSC of 0.977, this method suffers from long processing times, taking about 1.8 hours to segment a single CT exam.

One year later, the same authors proposed another method three times faster than the previous one. Rodrigues et al. [69] (2017) utilized a genetic algorithm to optimize the ellipse parameters that simulate the pericardium contour. The results revealed that the ellipse engulfed 99.5% of the epicardial fat. This upgrade made it possible to reach a processing time of 0.6 hours per exam, which still does not meet the typical needs of medical routines.

Rodrigues et al. [70] (2017) also realized a study regarding the feasibility of linear regressors to predict the cardiac fat volume. In this last work, each exam was evaluated in about 0.9 hours.

Rodrigues et al. work [12], [68]–[70] shows strong correlations between automatic and manual EFV, suggesting the great potential of methods that include Machine Learning (ML) algorithms. Nevertheless, it is important to note that the results were based only on the processing of 20 exams without specifying the size of the training and test datasets.

In the last years, artificial intelligence (AI) technology has been gaining ground in cardiovascular imaging. ML and Deep Learning (DL) architectures have been increasingly used in image segmentation, quantification, and clinical application. The most used DL algorithms are Convolutional Neural Networks (CNN), U-Net, K-mean clustering and extreme gradient boosting (XGBoost) [71].

Several DL works report poor performance in the blinded evaluation on unseen test data, probably due to reduced cases used in the training phase. The latest works show a notorious concern about using more extensive databases to avoid overfitting when applying ML or DL models. These AI algorithms were applied to more extensive databases, comprising 200 [72] to 1912 [73] patients.

Since the present thesis does not work with these large databases, DL and ML works will not be detailed. If the reader is interested in extending the knowledge to these technologies, the report of Zhang et al. [71] is strongly recommended. The authors elaborated a systematic review with the latest progress of image segmentation and the clinical application of AI in evaluating cardiac adipose tissue. Studies until April 2021 were reported in this review.

3.4. **Overview**

Several methods for automating epicardial fat segmentation and quantification were presented throughout this chapter. Table 3.1 summarises the characteristics and results of all studies discussed.

The first proposed algorithms were semi-automatic, which already allowed a significant reduction in time due to the decrease in the manual delineation. These methods mainly used basic image techniques, threshold-based and non-supervised segmentation. Although already presenting satisfactory accuracy, they still had limitations regarding the execution time per exam and the inter- and intra-observer variability.

In an attempt to overcome these limitations, the proposed algorithms were less and less dependent on human intervention until the emergence of fully automatic methods. Most of these methods were based on atlas-based segmentation or AI algorithms with supervised segmentation.

In general, the most accurate methods in literature use AI algorithms, presenting an excellent performance in terms of segmentation and quantification. However, they have two major limitations: the requirement of a sufficiently large and comprehensive database, and high computational costs for training the algorithms. These limitations make most methods incompatible with clinical implementation.

The next chapters will explore the proposal of this thesis: a hybrid method capable of performing fully automatic segmentation and quantification while optional manual human intervention is also allowed. This solution uses only basic image techniques, threshold-based segmentation and does not require a database for learning.

Table 3.1 - Characteristics of the studies in the literature that propose automated epicardial fat segmentation and quantification methods.

Authors	Methodology	Patients	Dataset type	Performance	Processing time
Bandekar et al. [65] (2006)	**Semi-automatic** ML: Features extraction; Fuzzy affinity-based.	23	Non-contrast CT	Acc (%) = 99.13 ± 0.38	< 1 min per slice
Dey et al. [8] (2008)	**Semi-automatic** BIA: Region-based thresholding.	105	Non-contrast CT	Spearman = 0.98	20 ± 4 s
Coppini et al. [10] (2010)	**Semi-automatic** BIA: Thresholding and level set segmentation.	10	CaSc CT	N.A.	N.A.
Barbosa et al. [15] (2011)	**Semi-automatic** BIA: Cubic interpolation; Region growing.	40	Non-contrast CT	Success rate of 52.5% (21/40 cases)	N.A.
Shahzad et al. [66] (2013)	**Automatic** BIA: Multi-atlas-based; thresholding.	98	Non-contrast CT	Spearman = 0.91 DSC = 89.2±1.9	N.A.
Spearman et al. [6] (2014)	**Automatic** BIA: Model-based	70	CCTA enhanced-contrast	Spearman = 0.889	135.6 ± 24.6 s
Ding et al. [3] (2015)	**Automatic** BIA: Atlas-based; Geodesic active contours.	50	Non-contrast CT	Spearman = 0.97 DSC = 0.92	60 s
Rodrigues et al. [68] (2015)	**Automatic** ML: registration; RF.	20	Non-contrast CT	Acc (%) = 98.4 DSC = 0.968	Few hours
Rodrigues et al. [12] (2016)	**Automatic** ML: Atlas-based; RF.	20	Non-contrast CT	Acc (%) = 98.5 DSC = 0.977	1.8 h
Nórlen et al. [67] (2016)	**Automatic** ML: Multi-atlas; RF.	30	CCTA	Spearman = 0.99 DSC = 0.91	51.9 s
Rodrigues et al. [69] (2017)	**Automatic** ML: Genetic algorithms.	20	Non-contrast CT	99.5% of epicardial fat engulfed by ellipse	0.6 h
Rodrigues et al. [70] (2017)	**Automatic** ML: RF; Multi-layer perception regressor.	20	Non-contrast CT	Spearman = 0.9683 RAE = 19.6% RRSE = 24.9%	0.9 h
Zlokolica et al. [74] (2017)	**Semi-automatic** ML: FCM clustering; geometric modeling.	10	CT enhanced-contrast	DSC = 69%	N.A.
Militello et al. [4] (2019)	**Semi-automatic** BIA: thresholding segmentation.	50 95	CaSc CT CCTA	Spearman = 0.9591 DSC = 0.9394 Spearman = 0.9319 DSC = 0.9248	3.5 min

Acc: Accuracy; BIA: Basic Image Analysis; FCM: Fuzzy c-means; RAE: Relative absolute error; RRSE: Root relative squared error; RF: Random Forest.

4.

SEGMENTATION AND QUANTIFICATION ALGORITHM

The present chapter presents the materials and methods used to implement the proposed semi-automatic approach for epicardial fat segmentation. The methodology is described step-by-step, where two processes are distinguished.

4.1. Materials

The medical images used are from the database provided by Visual Lab [75]. Currently, this is the unique database of cardiac CT publicly available. The database has 20 non-contrast cardiac CT scans and respective Ground Truth (GT). As a remark, all the patients were informed about the objectives of the original study and signed a consent form [12].

Each scan is stored in DICOM format and comprises 40 to 50 slices (or images), making 878 images. Each image has a spatial resolution of 512×512 pixels, a variable pixel spacing between 0.26 to 0.39 mm and a slice thickness of 3.0 mm. The GT images were performed by a physicist and a computer scientist who manually segmented all slices in the axial plane [12]. The labelling done by specialists is shown in Figure 4.1. Each colour corresponds to one type of fat: red, green, and blue represent epicardial, mediastinal fat and pericardium (the gap between these two fats), respectively. As the proposed study focuses only on the epicardial fat segmentation, only the red label will be relevant for validating results.

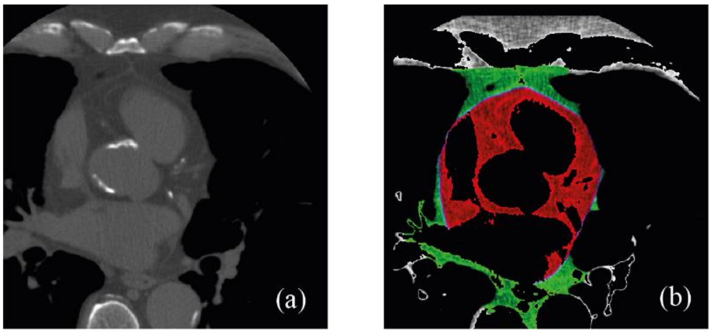

Figure 4.1 - Sample from medical imaging dataset (a) and correspondent ground truth image with fat type classification (b): epicardial (red) and mediastinal (green) fats, and the pericardium (blue).

All scans in the database are anonymous and do not contain any personal information. Details about each scan are provided in Table 4.1. Each patient was named with an acronym, but to more easily refer to each one, only a numeric ID (from 0 to 19) will be used.

Table 4.1 - Dataset description: ID, name, number of slices and epicardial fat volume of each patient scan.

Patient ID	Patient name	Number of slices	Epicardial Fat Volume (ml)
0	ACel	42	137.1
1	AEdu	41	68.7
2	AFre	43	124.9
3	AMar	42	66.4
4	AXav	48	242.3
5	CFer	43	204.3
6	CLis	36	68.8
7	DLag	41	123.6
8	DSan	36	134.9
9	DSil	54	29.6
10	EGra	48	90.8
11	FGas	48	39.7
12	FSiq	43	68.8
13	ISou	42	76.3
14	JFul	45	63.2
15	JMir	41	107.8
16	MPai	54	66.4
17	MSil	41	131.1
18	TJes	42	50.6
19	VMar	48	62.4

The proposed approach was entirely developed using Python language and image processing libraries, including OpenCV and scikit-image. The software interface was implemented using PyQt5.

4.2. Methodology

The proposed approach is intended to perform fully automatic without previous input from the specialist. Although, at the end of automatic segmentation, it is possible for human intervention so the specialist can make adjustments if needed and rerun the algorithm.

The whole processing pipeline (Figure 4.2) can be divided into four mandatory automatic steps and one optional step that can require human intervention: (1) Pre-processing; (2) ROI selection; (3) EAT Segmentation; (4) EFV computation; (5) ROI refinement. Step (5), the optional step, will be covered in more detail in Chapter 5 regarding the software.

A general flow chart of the image processing methods analysed in this work is given in Figure B.1 of Appendix B. The visualization of this diagram is recommended to get a general overview of the developed work coupled with output images of each step.

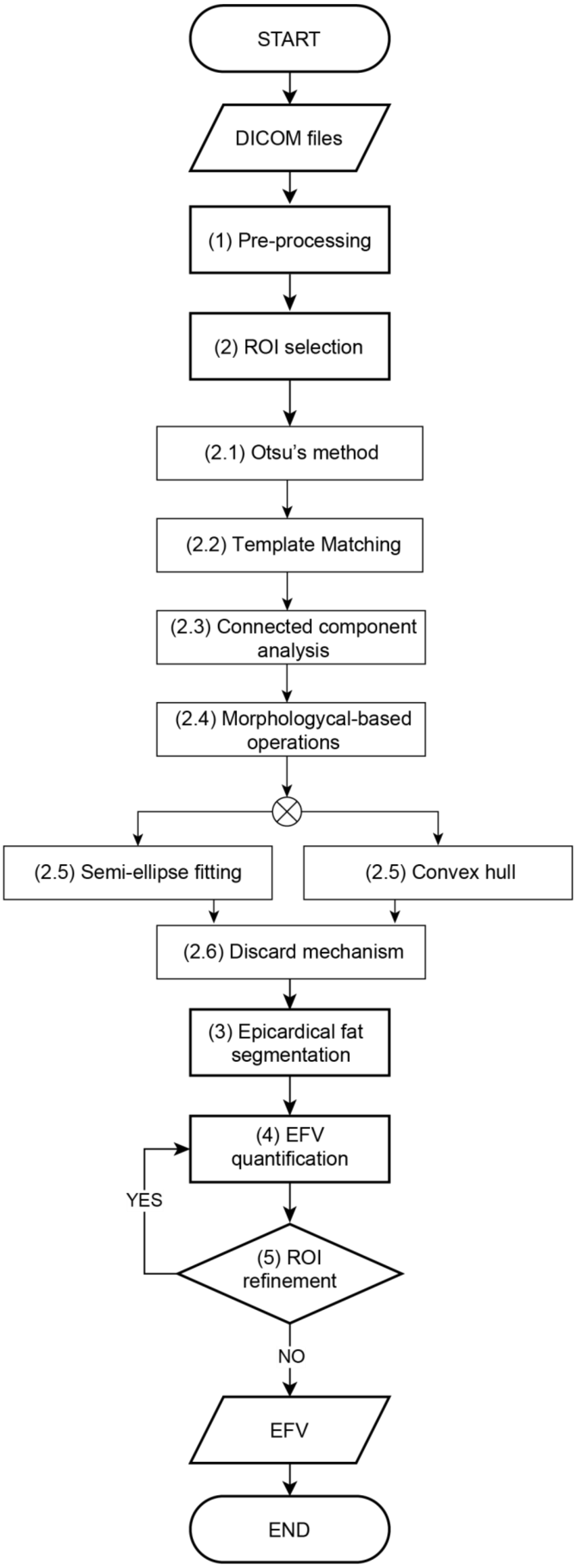

Figure 4.2 - Algorithm pipeline of the proposed approach.

4.2.1. Step 1: Pre-processing

The main goal of the pre-processing step is to reduce noise and remove artefacts in images that can perturb the clustering steps. The median filter is useful to reduce the noise in CT images, as evidenced by Omer et al. [76]. It is a non-linear filtering method, efficient in removing impulsive noise while preserving the edges in the image. Edges preservation is important since they will be used for high-level operations such as segmentation [77]. Therefore, a 5 × 5 median filter was applied in each slice. The kernel size was empirically determined.

The median filter replaces the intensities of all image pixels by the median of the pixels present in a two-dimensional kernel of size $n \times n$. The values of the image covered by the kernel are arranged in ascending order, and the median value is the one that divides the list into two halves. Figure 4.3 shows the median filtering mechanism exemplified with a 3 × 3 kernel.

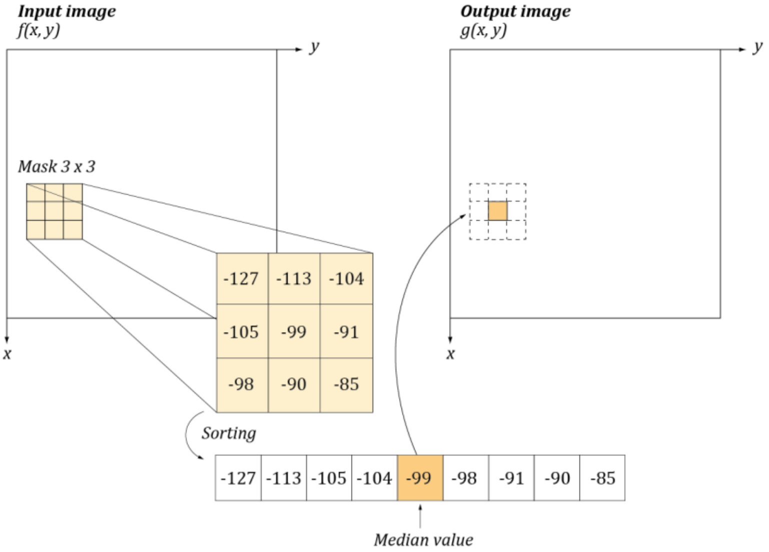

Figure 4.3 - Median filter mechanism characterized by 3×3 convolution kernel.

The application of median filter leads to images with more homogeneous zones, especially those representing the same type of tissue. Figure 4.4 shows zoomed portions of the original and filtered images. After the median filter application, the images became smoother without blurring the edges.

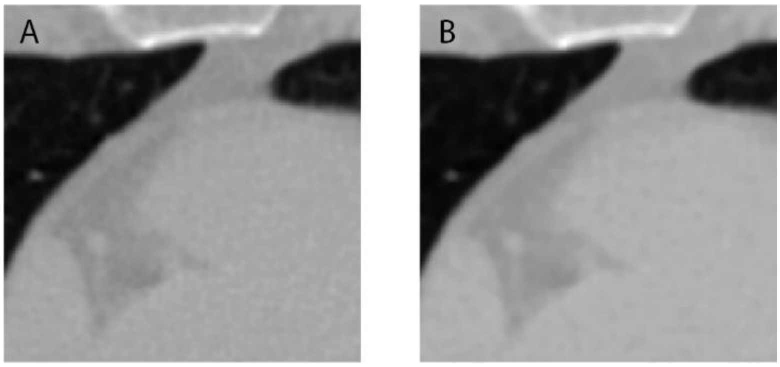

Figure 4.4 - Zoomed portions of the original image (A) and median filtered image characterized by 5×5 convolution kernel (B).

4.2.2. Step 2: ROI selection

The epicardial fat corresponds to the fat within the pericardium boundary. As discussed in Chapter 2, fat segmentation is a time-consuming process because the very thin barrier of the pericardium might be difficult to identify along its entire length. Thus, automatic delimitation of the pericardium is challenging due to its non-linear anatomy.

In the ROI selection step, the strategy adopted to access the pericardial limit is based on a successive restriction of the ROI. For this purpose, this step is divided into substages. All thorax structures are firstly removed apart from the heart. Subsequently, the resulting heart regions are post-processed to remove the remaining areas outside the pericardium contour.

Two different sets of five basic image techniques were applied to perform ROI selection. These two sets, hereafter designed as Method 1 (M1) and Method (M2), differ only in the last step. The methods are detailed in Figure 4.2, and each step (or image technique) will be described in the following sections.

4.2.2.1. Otsu's Method

Otsu's Method is a threshold-based segmentation used to automatically calculate an adequate image thresholding level. In this step, Otsu's Method segments the heart, ribcage and spine from the background in each slice.

This method searches for a threshold that maximizes the variance between two groups as homogeneous as possible. Although it can be applied to other histograms, Otsu's Method works better in bimodal histograms [51].

CT image histograms are typically bimodal, as can be observed in the histogram of Figure 4.5. The yellow line marks the Otsu thresholding, which separates the two main histogram peaks. In each slice, the Otsu's Method returns a threshold value, T, in HU, that maximizes the variance between the groups ($\sigma^2_{inbetween}$). Or, in other words, minimizing the variance within the group (σ^2_{within}).

$$\sigma^2_{inbetween} = \sigma^2 + \sigma^2_{within} = P_b(t)P_f(T)\left[\mu_b(T) - \mu_f(T)\right]^2 \tag{4.1}$$

$$\sigma^2_{within} = \sigma^2_b + \sigma^2_f = P_b(T)\sigma^2_b + P_f(T)\sigma^2_f \tag{4.2}$$

Where $P_b(T)$ and $P_f(T)$ represent the probability of the background and foreground pixels, respectively, and n is the number of pixels.

$$P_b(t) = \sum_{i=0}^{t} p(i) \tag{4.3}$$

$$P_f(t) = \sum_{i=t+1}^{n-1} p(i) \tag{4.4}$$

$\mu_b(t)$ and $\mu_f(t)$ represent mean intensities of the background and the foreground, respectively.

$$\mu_b(t) = \frac{\sum_{i=0}^{t} ip(i)}{P_b(t)} \quad (4.5)$$

$$\mu_f(t) = \frac{\sum_{i=t+1}^{n-1} ip(i)}{P_f(t)} \quad (4.6)$$

Although T values are different from slice to slice, these values registered a mean of -425 HU. The advantage of using Otsu's method over using a basic threshold technique with a static value T ensure more flexible and personalized foreground segregation to each slice.

The input image pixels with intensity greater than or equal to T are considered foreground; otherwise, they are considered background. The output of this step is a mask (Figure 4.5-c) where the foreground gets the value 1 (white), and the background brings the value 0 (black).

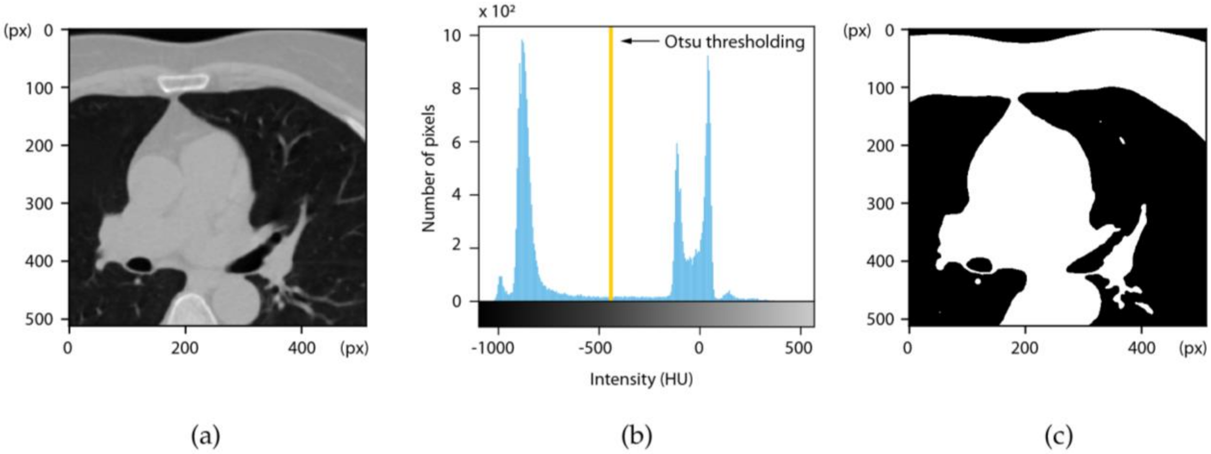

Figure 4.5 - Otsu method. Median filtered image of a slice (a), its histogram (b) with the Otsu thresholding marked by the yellow line and the resulting thresholded image (c).

4.2.2.2. Template Matching

Template Matching is a method for finding the location of a template pattern in an image [78]. This substep is used to restrict the heart region by detecting two anatomical structures in each slice: the sternum and the spine. The inferior limit of the sternum area (line with abscissa X_B) and the superior limit of the spine area (line with abscissa X_T) will be the top and bottom limits of the heart (Figure 4.6), respectively.

The sternum is a flat bone located at the anterior of the thorax, highlighted by the yellow rectangle in Figure 4.6. This area does not vary significantly among patients [1] and it is virtually never cropped off during the acquisition of the cardiac images. Due to sternum tapered anatomy, it is easily recognized in the first 20 slices, but it fades from then on. In these cases where the sternum is not easily detected, the last detected area is taken as the current position. The spine, unlike the sternum (blue rectangle in Figure 4.6), maintains its circular appearance throughout the slices. However, it is sometimes accidentally cropped during image acquisition. When the spine is not visible, no area is detected for this anatomical structure.

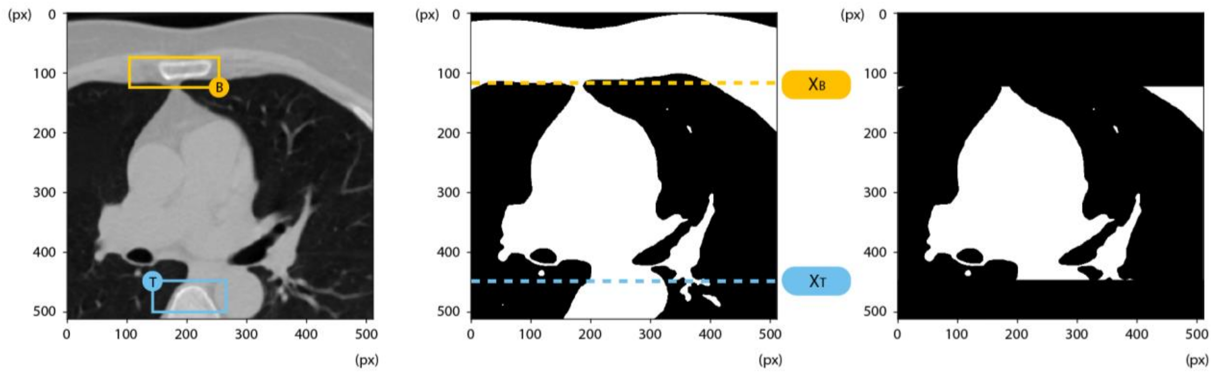

(a) (b) (c)

Figure 4.6 - Template Matching process. The sternum and spine templates are firstly found (a). Points B and T are the bottom right point of sternum detected area and the top left point of spine detected area, respectively. The abscissas X_B and X_T mark the superior and inferior limits, respectively (b). The output is a mask of the heart region (c).

To generate the sternum and spine templates, 20 slices were randomly selected. In each slice, the sternum and the spine were manually cropped. Finally, the 20 selections (of each structure) were manually aligned. The final template is the weighted average of the 20 chosen images, where each selection with intensities previously normalized between 0 and 1 has a weight of 0.2. Using a weighted average template rather than only one sample allows a more comprehensive detection since more anatomic variations are considered throughout slices.

The generated template for the sternum and spine are depicted in Figure 4.7 and Figure 4.8, as well as the process to their generation.

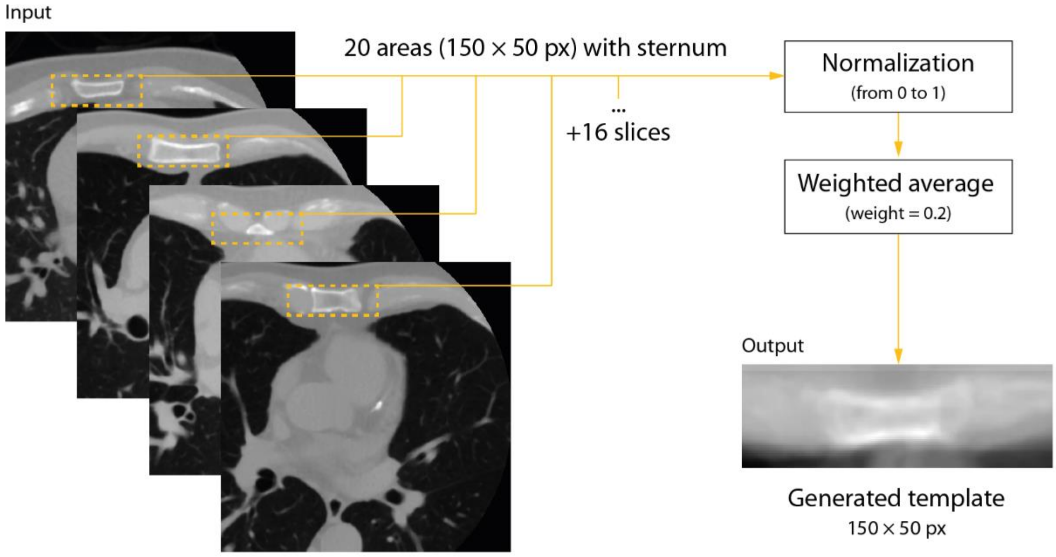

Figure 4.7 - Sternum template generation.

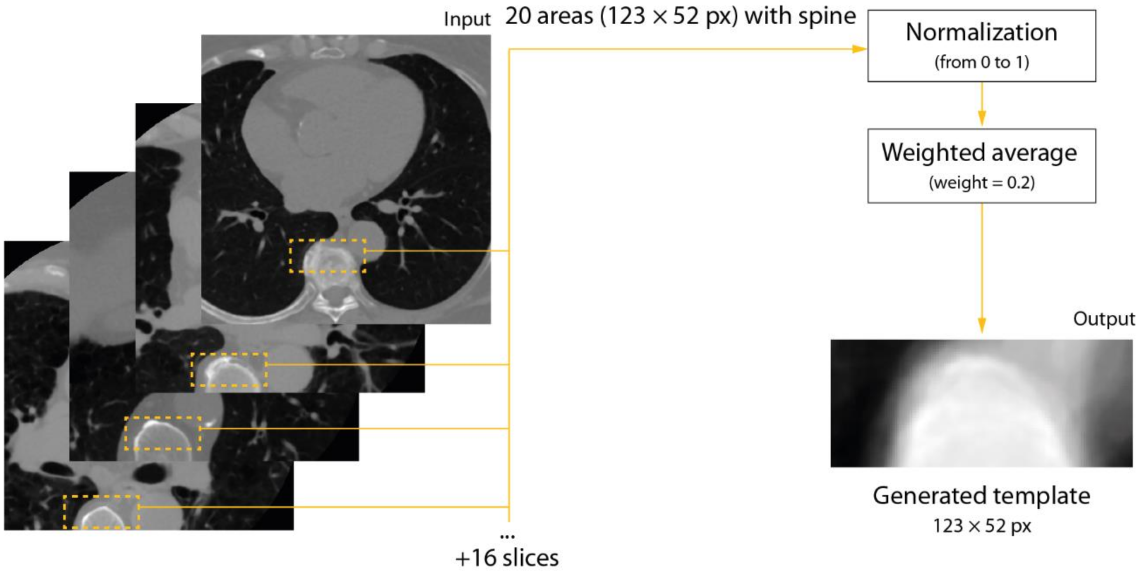

Figure 4.8 - Spine template generation.

The Template Matching mechanism slides the template image over the input image (as in 2D convolution) and compares the template with the input image patch under the template. The output is a grayscale image (Figure 4.9), where each pixel denotes how much the neighbourhood of that pixel matches the template. Between several comparison methods, the correlation coefficient was chosen. Equation 7 define the correlation coefficient, where I denotes the image, T the template, and R the result.

$$R(x,y) = \frac{\sum_{x',y'}\left(T'(x',y')\cdot I'(x+x',y+y')\right)}{\sqrt{\sum_{x',y'}T'(x',y')^2\cdot\sum_{x',y'}I'(x+x',y+y')^2}} \tag{4.7}$$

The correlation coefficient varies from +1 to -1, presenting higher values (bright colours) where the pixel neighbourhood is better correlated with the template and lower values where it is worst correlated (dark colours).

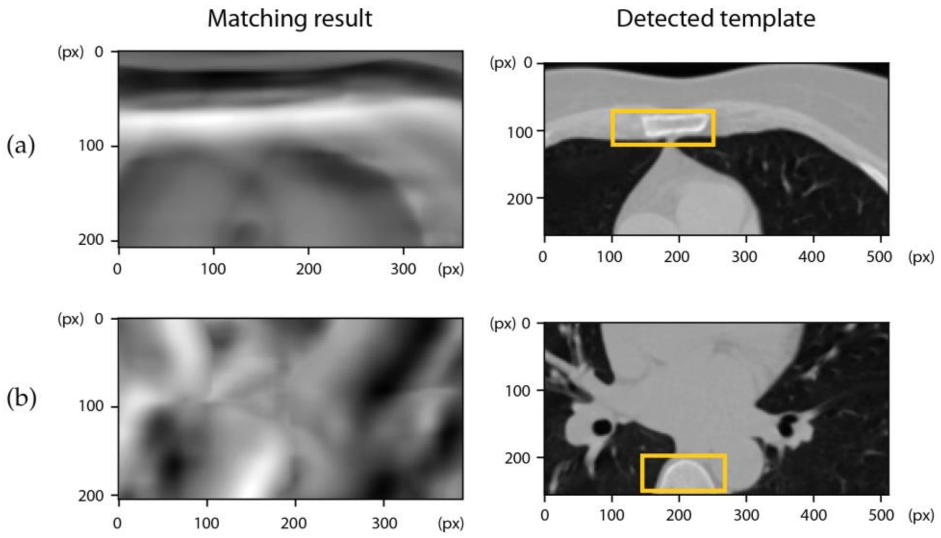

Figure 4.9 - Sternum (a) and spine (c) detection using Template Matching.

Given the input image $N \times M$ and the template image $m \times n$, the output image will have a size of $(N - n + 1) \times (M - m + 1)$. The sum is done over the template and the image patch: $x' = 0, \dots, m - 1, y' = 0, \dots, n - 1$.

After the correlation coefficient comparison, the best match corresponds to the global maximum of the output image. In the input image, this point is taken as the top-left corner of the $m \times n$ rectangle corresponding to the template region. In the present case, the sternum and spine templates have a resolution of 150×50 and 123×52, respectively, and the input image has 512×256, representing half of the original slice resolution. Depending on the template detection (sternum or spine), the input image corresponds to the top or bottom half, in that order. The decision of taking half of the image was based on matching errors minimization.

Although detecting the two anatomical structures works well on most slices, approximations were made to handle some scenarios. Regarding sternum detection, Figure 4.10 shows the two leading causes of matching errors.

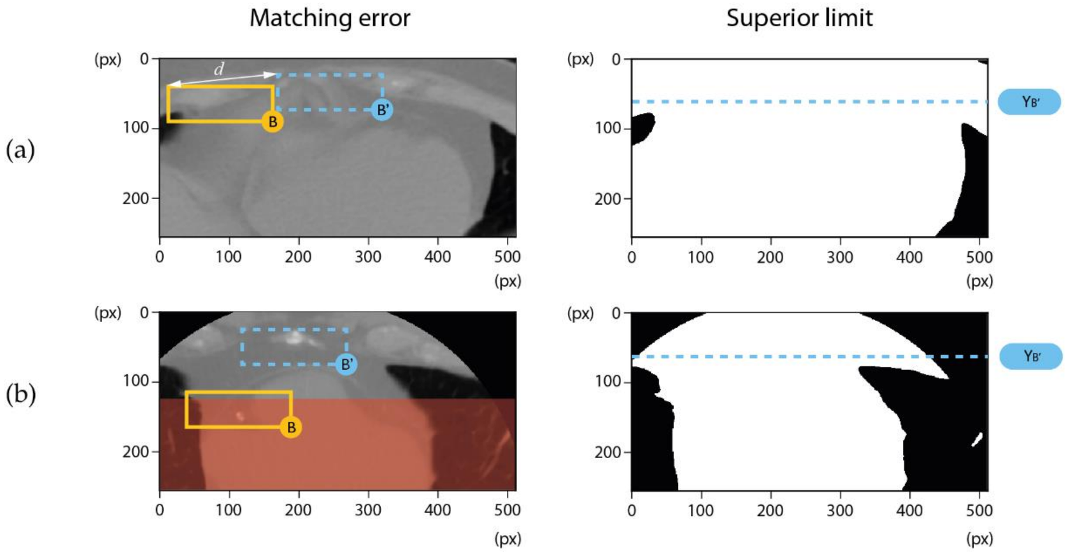

Figure 4.10 - Sternum matching errors. The yellow rectangles represent the current output, while the blue ones represent the previous output.

As previously discussed, the sternum is no longer present in the last slices of each CT exam. In these slices, other regions are detected in place of the sternum (Figure 4.10-a). Another common matching error is generated for calcifications easily confused with the end of the sternum xiphoid process (Figure 4.10-b). These two types of matching errors concerning the sternum are formalized below, as well as the strategy adopted to overcome them.

- **Error:** It is considered a *sternum matching error (a)* when the $m \times n$ rectangle is detected more than a distance d[1] away, in pixels, from the detected rectangle in the previous slice.
- **Error:** It is considered a *sternum matching error (b)* when the bottom left point B of the $m \times n$ rectangle is in the lower half of the input image, even though it is less than a distance d[1] away, in pixels, from the bottom left point B' of the last detected rectangle.

---

[1] The distance d is taken as 150 px, empirically determined.

Solution: For *sternum matching errors (a) and (b),* the last detected $m \times n$ rectangle is taken as the actual matching result. In other words, the superior heart limit becomes the line with the previous abscissa B' in place of the current abscissa B.

Regarding spine detection, Figure 4.11 shows similar leading causes of matching errors. As previously mentioned, in the registration step taken by Rodrigues et al. [12], anatomical structures as the spine were accidentally cut. In this case, random regions are detected in place of the spine (Figure 4.11-a). In slices where the spine is cropped but not completely cut, the descending aorta is often taken as a matching result (Figure 4.11-b). These two types of matching errors concerning the spine are formalized below, as well as the strategy adopted to overcome each one:

- **Error:** It is considered a *spine matching error (a)* when the $m \times n$ rectangle is detected more than a distance d [2] away, in pixels, from the detected rectangle in the previous slice.

  Solution: For *spine matching error (a),* the last detected $m \times n$ rectangle is taken as the actual matching result. In other words, the inferior heart limit becomes the line with the previous abscissa T' in place of the current abscissa T.

- **Error:** It is considered a *spine matching error (b)* when the top right point T of the $m \times n$ rectangle is in the upper $1/5$ of the input image, without distance d [2] defined.

  Solution: For *spine matching error (b),* the inferior heart limit corresponds to the inferior limit of the input image.

As shown in Figure 4.6-(c), the output of the Template Matching step is a mask of the heart region.

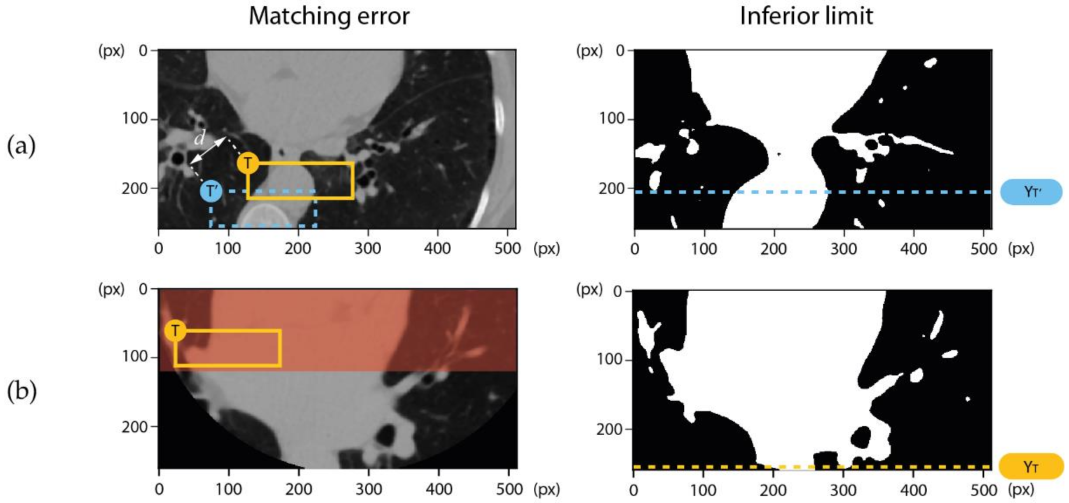

Figure 4.11 - Spine matching errors. The yellow rectangles represent the current output, while the blue ones represent the previous output.

---

[2] The distance d is taken as 20 px, empirically determined.

4.2.2.3. Connected component analysis

Besides the contour of the heart, other contours are still detected in the current ROI due to a suboptimal segmentation resulting from Otsu's Method. In order to select the largest contour corresponding to the heart, the connected component analysis with 4-connectivity was applied.

Connected Component Analysis (CCA) is the process of identifying disjoint elements in a binary image. This analysis involves scanning the image by rows and assigning a unique label to the pixels of the same object (or component). In the case of 4-connectivity CCA, it is considered as a component, a group of pixels connected by their faces (i.e., horizontally and/or vertically) [79]–[81].

After labelling, the binary image is transferred to a labelled image (Figure 4.12). All components areas are calculated, and the largest one is extracted by its label. The selected component represents the heart contour. Taking Figure 4.12 as reference, the component with the largest area has the label number 2.

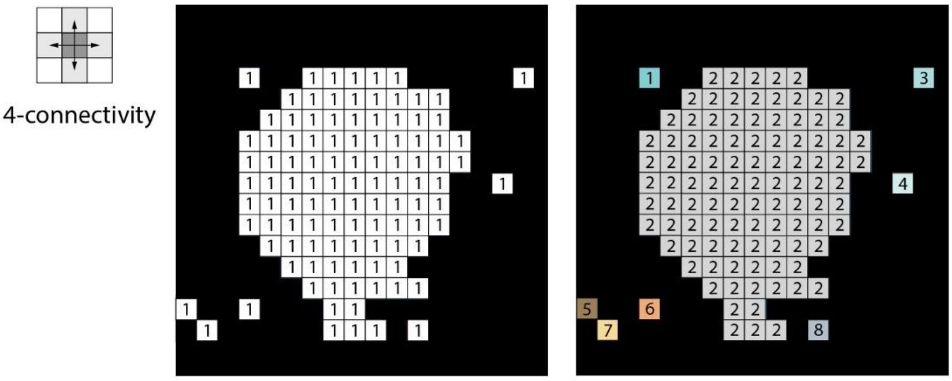

(a) (b)

Figure 4.12 - Connected Component Analysis. Binary image (b) and labelled image after 4-connectivity connected component analysis.

4.2.2.4. Morphology-based operation

Figure 4.13-a shows that close to the heart are other anatomical structures, such as bronchioles and pulmonary arteries and veins. Due to this proximity, the ROI resulting from the previous substep is often linked to some of these structures.

In order to remove surrounding parts of the heart, a morphological opening operation was used where the structuring element (SE) was a filled ellipse with 65 px of width and 70 px of height. The use of an elliptic SE is due to the main circular shape of the heart (in 2D image slice). The optimal size of SE was empirically obtained.

Two opening operation iterations were applied in each slice, which is equivalent to applying the sequence erosion-erosion-dilation-dilation. In the erosion operation, the SE moves the image twice point to point, turning black all 65×70 pixels patches where the elliptic kernel does not fully fit. Subsequently, SE moves the image twice in the dilation operation, turning white all the pixels patches where the kernel partially or fully fits.

At this pipeline stage, the ROI is no longer the "heart region" but a more restricted heart area, resulting in a tighter mask shown in Figure 4.13-b.

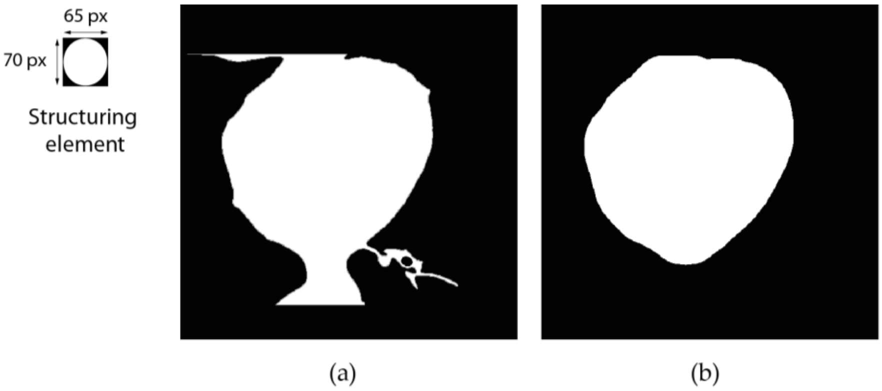

Figure 4.13 - Opening operation. Heart region mask (a) and heart mask after opening operation (b) which the structuring element is a filled ellipse with 65×70 pixels.

4.2.2.5. Semi-ellipse fitting

After inspecting the images segmented by the previous ROIs, mediastinal fat was often found. Mainly in the upper half of the ROI, where the contour is not close enough to the pericardium. As mediastinal fat is easily confused with epicardial fat in terms of grey level, including it in the ROI would generate false positives. Hence, the present substep aims to post-processing and filter the undesirable fat.

The epicardial fat distribution can be well fitted to an ellipse. Moreover, ellipse fitting algorithms were already proposed, as highlighted in the state-of-the-art chapter. Rodrigues et al. [69] and Zlokolica et al. [74] achieved positive results when segmenting epicardial fat using ellipse geometry.

Based on a similar strategy, a semi-ellipse fitting was performed to remove heart areas outside the pericardium contour. This step consists of drawing an ellipse centred on the current ROI centroid that passes through the pericardium outline (Figure 4.14-b). ROI areas within the semi-ellipse are selected as desirable, while other parts are filtered out as undesirable.

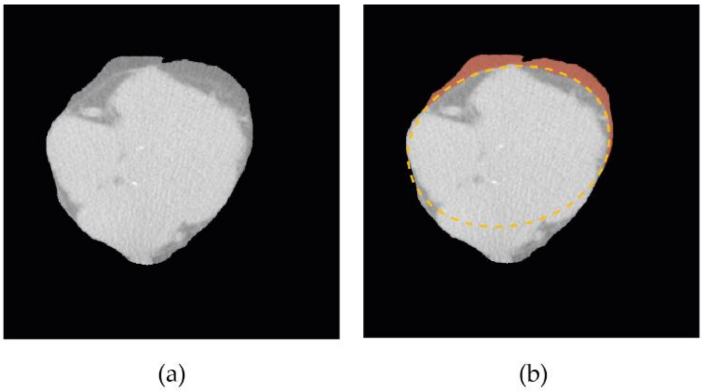

Figure 4.14 - Segmented heart using the ROI from morphology-based masking step (a). The red shadow highlights mediastinal fat, and the yellow dashed line indicates an ellipsoidal shape that fits pericardium contour (b).

The following steps reach ellipse computation for a particular image slice:

1. Pericardium assessment by segmentation based on thresholding;
2. Estimation of ellipse centre (x_c, y_c);
3. Estimation of the leftmost (L), topmost (T) and rightmost (R) points of pericardium contour;
4. Estimation of ellipse parameters a and b corresponding the axes length;
5. Estimation of the angle θ_0 between major axis of ellipse and y-axis of the image slice.

The assessment of the pericardium area was achieved by applying a threshold-based technique on the current segmented ROIs. The thresholding range was estimated based on Barbosa et al. [15] work, where the authors evaluate the possibility of segmenting the pericardium based on intensity values. Statistically, the pericardium samples have a mean of -13 HU and a standard deviation of 31 HU. On the other hand, the cardiac muscle samples have a mean of 38 HU and a standard deviation of 23 HU. To minimize the overlap between these two tissues, a range of [-44, -1] HU was set to access the pericardium. As shown in Figure 4.15, this range corresponds essentially to pericardium grey levels.

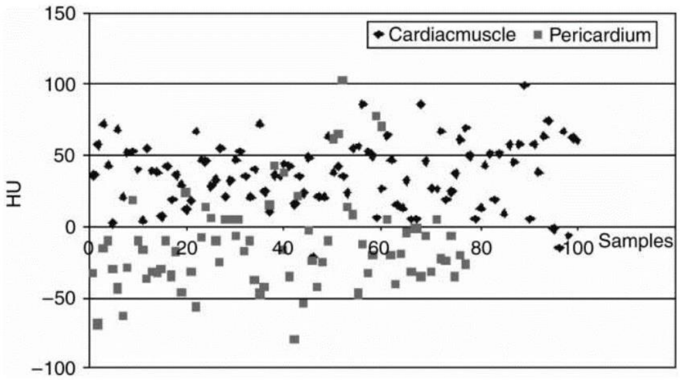

Figure 4.15 - Intensity values in HU for pericardium and cardiac muscle samples. From Barbosa et al. [15].

The threshold result is shown in Figure 4.17-a. As predicted by Barbosa et al. [15], the threshold-based technique does not exclusively segment the pericardium. However, it is possible to approach the pericardial contour to the outer segmentation shape. The upper half of the pericardium contour is fitted into a semi-ellipse by calculating the centre point and three contour points of the ROI.

An ellipse is parameterized in polar coordinates by the following form

$$\begin{gathered} x(\theta) = x_c + a\cos(\theta + \theta_0), \\ y(\theta) = y_c + b\sin(\theta + \theta_0), \\ \theta \in [0, 2\pi[\end{gathered} \tag{4.8}$$

where $(x_c, y_c) \in \mathbb{R}^2$ is the ellipse centre, $a, b > 0$ are parameters corresponding to the axes length, and θ is the angular parameter (Figure 4.16). Ellipse centre was calculated as the ROI centroid, based on the centre of gravity approach. The centroid is given by

$$\hat{x}_c, \hat{y}_c = \left\{ \frac{M_{10}}{M_{00}}, \frac{M_{01}}{M_{00}} \right\} \tag{4.9}$$

with image moments $M_{i,j}$, $i, j \in \mathbb{N}$, defined by

$$M_{i,j} = \sum_{x=1}^{M} \sum_{y=1}^{N} x^i y^j I(x, y) \tag{4.10}$$

where i and j are discrete spatial coordinates corresponding to x- and y-axes of the image, and $I(x, y)$ is the pixel intensity.

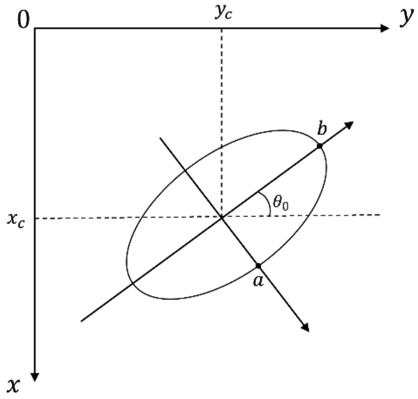

Figure 4.16 - Ellipse representation and its parameters.

The leftmost (L), topmost (T) and rightmost (R) points of the pericardium contour are considered as the white pixels in the thresholded ROI with lower ordinate, lower abscissa and higher ordinate, respectively.

The parameters a and b are, respectively, the semi x-axis and semi y-axis lengths of the ellipse. Parameter a is given by the greater distance between the centre and L or R points. The parameter b is given by the distance between the centre and T point.

Considering the distance between two points is given by the euclidean distance

$$d_{i,j} = \sqrt{\left(x_i - x_j\right)^2 + \left(y_i - y_j\right)^2} \tag{4.11}$$

where, $i, j \in \{L, T, C, R\}$, the distances d_a and d_b are given by

$$a = max\{d_{CL}, d_{CR}\} \tag{4.12}$$

$$b = d_{CT} \tag{4.13}$$

The angle θ_0 between the major axis of the ellipse and the y-axis of the image can be calculated as the angle between points C and T less π radians (or 180 degrees).

$$\theta_0 = arctan\left(\frac{y_C - y_T}{x_C - x_T}\right) - \pi \tag{4.14}$$

Finally, a semi-ellipse was drawn with a centre (x_c, y_c), semi x-axis and semi y-axis a and b, respectively, and an offset angle θ_0. Figure 4.17-b depicts all the calculated parameters. The final result of this step is a new ROI with a more restricted upper half (Figure 4.17-c).

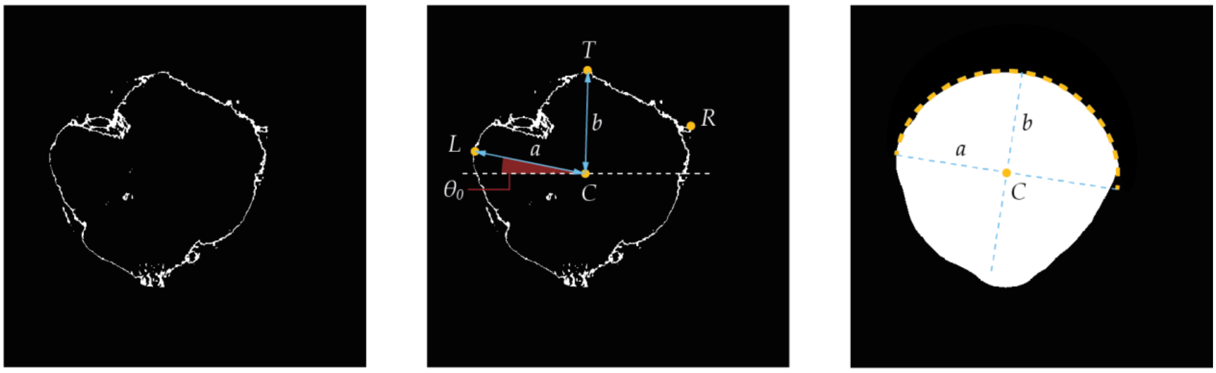

(a) (b) (c)

Figure 4.17 - Semi-ellipse fitting. Assessment of pericardium area by a threshold-based technique (a), the ellipse parameters estimation (b) and the new ROI mask with a more restricted upper half (d).

4.2.2.6. Convex hull followed by opening operation

The previous strategy only removes areas outside the pericardium in the upper half of the ROI, where mediastinal fat manifests more prevalence. In order to post-segment the ROI in both halves, a different and never used direction was followed. Convex hull followed by morphological opening operation was performed to remove undesirable heart areas in the current ROIs.

By using this method, the computation of pericardium contour for a particular image slice is reached in the following steps:

1. Pericardium assessment by segmentation based on thresholding;
2. Convex hull by Gift Wrapping Algorithm;
3. Morphological opening operation for edge smoothing.

The assessment of the pericardium area was achieved in the same way as in the previously presented substep. In contrast, the outer segmentation shape was approached to a convex hull, i.e., a minimal perimeter convex polygon containing the group of white pixels.

Convex hull was computed using Gift Wrapping Algorithm [82]. The algorithm starts with the leftmost point (p_0). At each step it is calculate the polar angles of the segments formed between all other points and the current point p_i. Using these angles, the point p_{i+1} is picked such that all the other points are to the right of the segment (Figure 4.18).

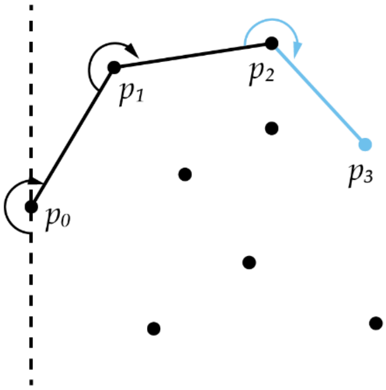

Figure 4.18 - Gift Wrapping Algorithm computing convex hull.

The convex hull represented by the yellow line in Figure 4.19-b was filled. An opening operation was then applied on the filled ellipse to smooth the polygon edges, where the SE was a filled ellipse with 30 px of width and 30 px of height.

This substep results in a new ROI mask with a more restricted area, not exclusively in its upper half, as Figure 4.19-c shows.

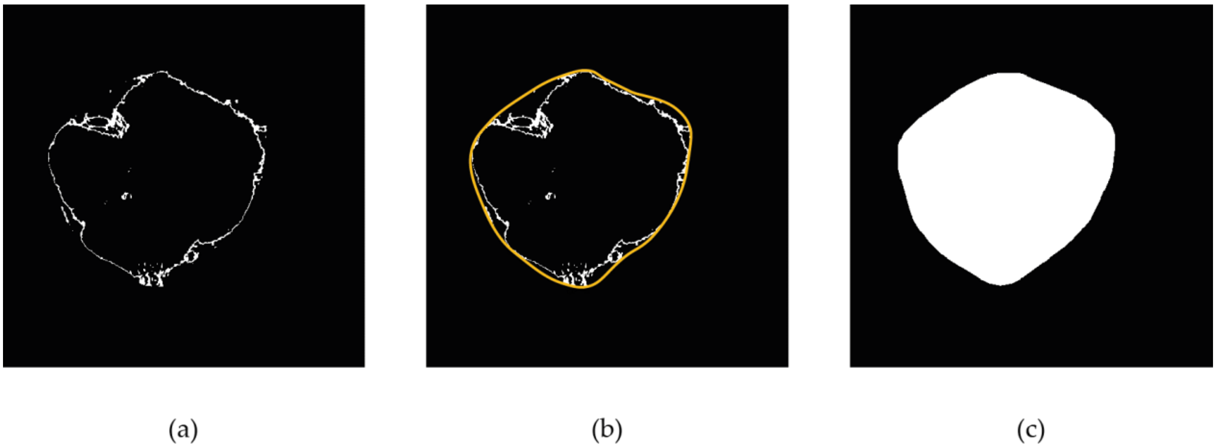

Figure 4.19 - Convex hull followed by opening operation. Assessment of pericardium area by a threshold-based technique (a), with the convex hull denoted by yellow line (b) and new ROI mask resulting from filled convex hull followed by opening (c).

4.2.2.7. Discard mechanism

In the last slices of each exam, the assessment of the pericardium by thresholding often results in spread areas, and Figure 4.20-c illustrates an example. Typically, the epicardial fat regions in these slices are smaller, as confirmed by the red region in Figure 4.20-b. Moreover, these slices contain other tissues, such as papillary muscles, whose grey level is closer to the applied threshold range of [-44, -1] HU.

When applying semi-ellipse fitting or convex hull to get the pericardium contour, the results end up in ROIs wider than supposed. Counting with overestimated ROIs would overestimate the epicardial fat volume due to the increase of false positive rate.

By inspection, a pattern was found in the last slices segmentation: the corresponding ROIs touch at least one edge of the image. Therefore, given the weak accuracy in segmenting these slices, the following criterion was implemented: *Slices presenting final ROIs so spread that touch at least one edge of the image are discarded in the automatic processing method and left to specialist consideration.*

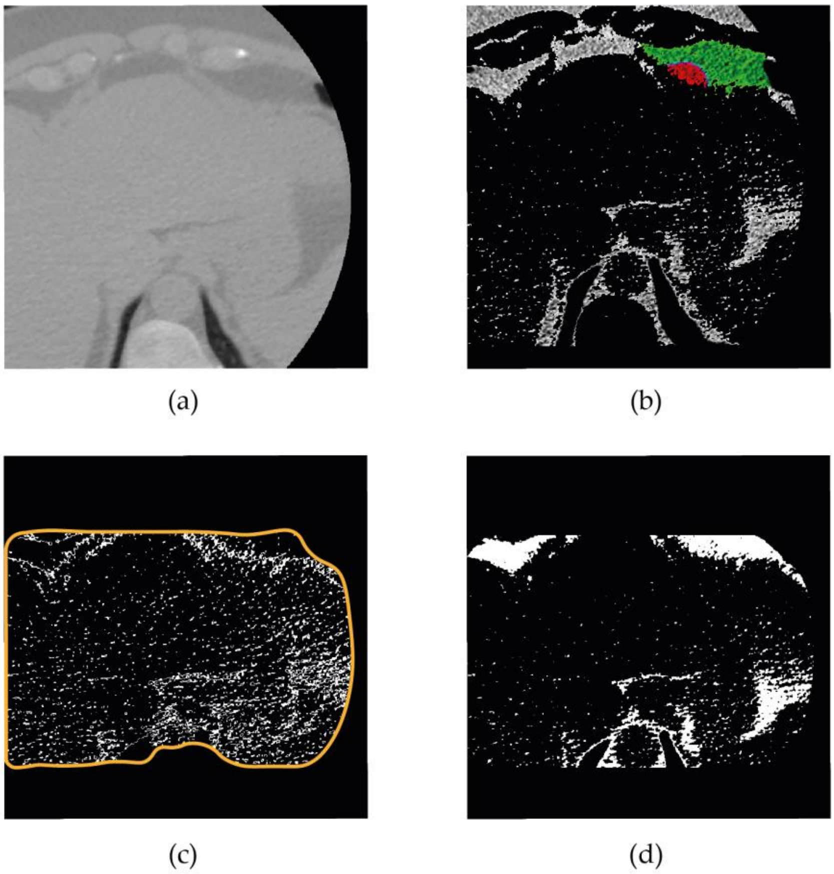

Figure 4.20 - Example of a discarded slice. Original image (a) and corresponding ground truth (b), where the red label represents epicardial fat. Pericardium area obtained by threshold-based segmentation with the outer contour of the ROI (c). Finally, the overestimated epicardial fat segmentation (d).

4.2.3. Step 3: Epicardial fat segmentation

The segmentation of epicardial fat is performed only inside the selected ROI, by applying bit-wise logical conjunction between the ROI mask $M(x, y)$ and the corresponding median filtered image $I(x, y)$. The resulting image $R(x, y)$, represented in Figure 4.21 is given by

$$R(x,y) = I(x,y) \wedge M(x,y) \quad \boldsymbol{if} \quad M(x,y) \neq 0 \tag{4.15}$$

where $I(x, y)$ and $R(x, y)$ have the same resolution.

As analyzed in Section 2.2.1, the overall fat of the human body can be accessed by an interval around -100 HU. Specifically, cardiac fat has lower intensity values in cardiac CT images [15]. There is no rigid intensity range for epicardial fat since it depends on CT scanners or acquisition protocols [10]. However, most specialists define epicardial fat interval as

$[-190, -30]$ [10], [83], $[-195, -45]$ [3], [6], $[-200, -30]$ [12], [66]. The range used in the present work was [-200, -30] HU, similar to the database providers Rodrigues et al. [12]. This interval fits properly in 8 bits-depth image and no interpolation is required, avoiding any possible data loss [12].

Thresholding window of [-200, -30] HU was applied on ROI image $R(x, y)$, outputting the thresholded image $T(x, y)$ given by

$$T(x, y) = \begin{cases} 1, & -200 \leq R(x, y) \leq -30 \\ 0, & otherwise \end{cases} \tag{4.16}$$

where the white area (pixels with value 1) corresponds to epicardial fat, and the black area (pixels with value 0) corresponds to no epicardial fat pixels.

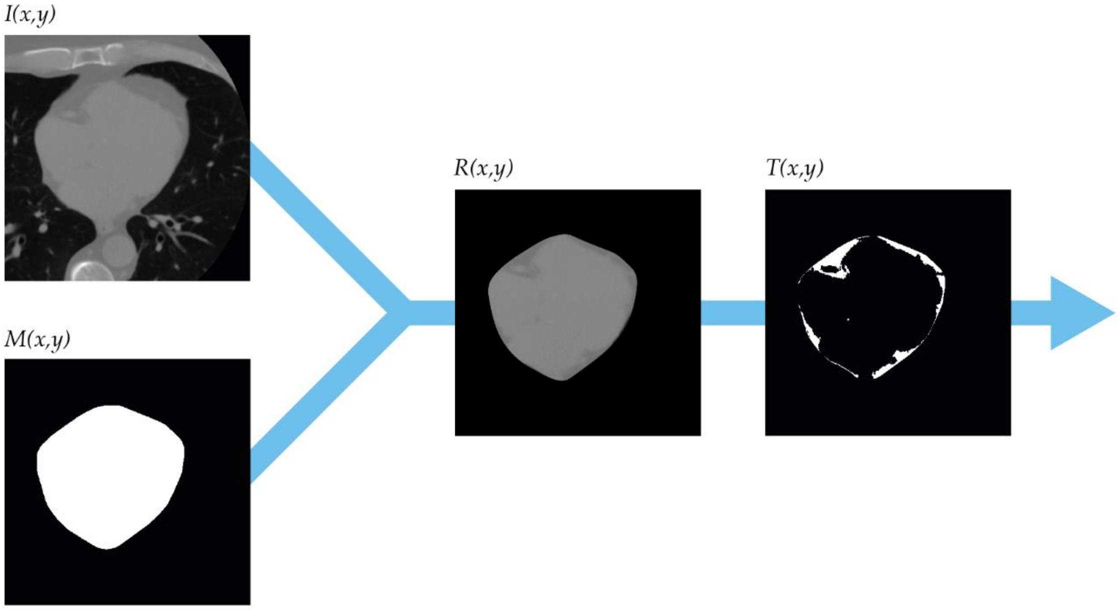

Figure 4.21 - Epicardial fat segmentation. Median filtered image $I(x, y)$, ROI mask $M(x, y)$, ROI segmentation $R(x, y)$ and epicardial fat segmentation mask $T(x, y)$.

4.2.4. Step 4: Epicardial fat volume computation

The epicardial fat volume of one patient is computed using simple interpolation between all epicardial fat segmentation masks, respecting the acquisition distance between them.

Slice thickness (h) is the distance between slices, and pixel spacing (w) is the physical distance between the centres of each two-dimensional pixel of a given slice. These values are stored in the DICOM file header. In the used scans, the slice thickness tag is 3.0 mm, while the pixel spacing tag varies between scans.

Let $p_n(i, j)$ be a pixel with coordinates (i, j) in the binarized segmented image of n^{th} slice, the epicardial fat volume (EFV) is given by

$$EFV = hw^2 \sum_n \sum_{i,j} p_n(i,j) \tag{4.17}$$

which can be easily translated in the product between the total number of white pixels in segmented images of all slices $\sum_n \sum_{i,j} p_n(i,j)$, and the volume of one voxel hw^2.

Figure 4.22 shows a 3D volume of epicardial fat resulting from interpolation of slices containing the epicardial fat segmentation masks.

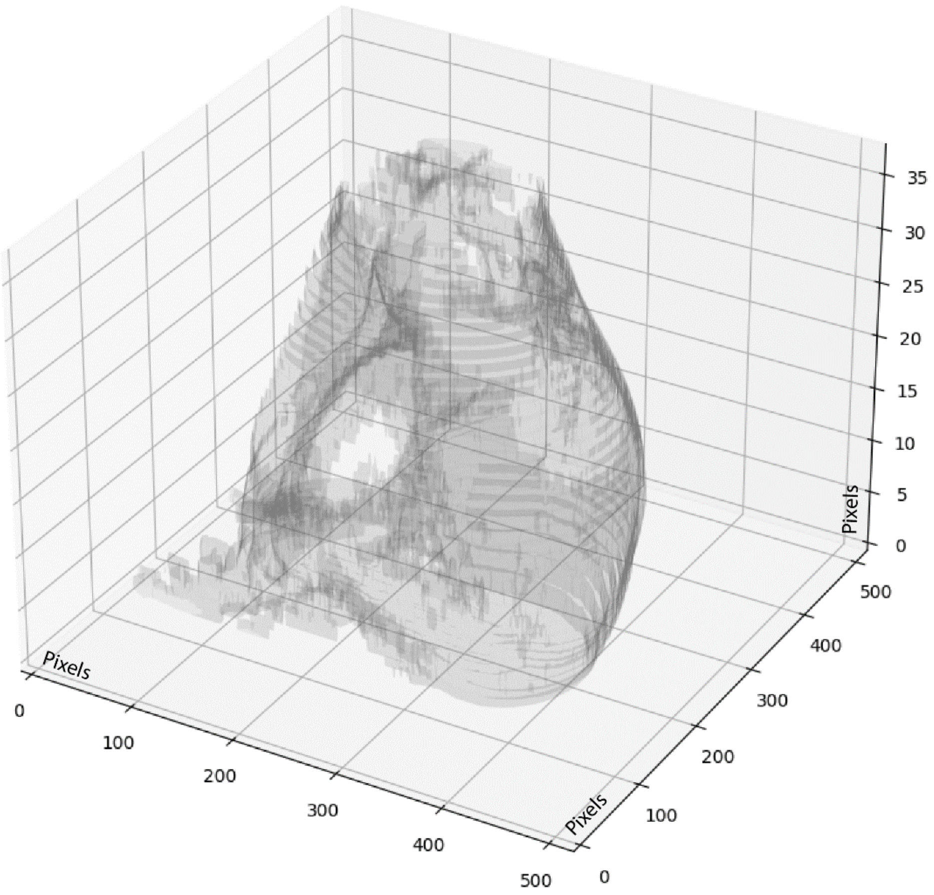

Figure 4.22 - 3D volume of epicardial fat resulting from segmented slices interpolation.

5.

HARTA SOFTWARE

The software HARTA was developed to enable manual adjustments on the pericardial tracing automatically set by the algorithm presented in the previous chapter. This process corresponds to the ROI refinement step mentioned in Section 4.2.

The present chapter explains in more detail the functionalities of this small proof of concept. The functionalities are described in terms of the user experience and from the implementation perspective.

HARTA and all the developed scripts are made available online at the following link: https://github.com/aforebelo/HARTA.

5.1. User experience

Figure 5.1 depicts the software's main window. This figure will aid the instructions on how to use HARTA. Firstly, the user uploads a dataset exam which should contain the data in format DICOM (.dcm). After loading, the user may press the "Calculate Volume" button to perform the EFV computation. A few seconds later, the "Automatic detection" box displays the automatically quantified Epicardial Fat Volume (EFV). To the left of the window, navigation over the slices is allowed (using the "Next" and "Previous" buttons) to check the performed segmentations. The epicardial fat segmentation is highlighted in red on each slice.

If the user wants to edit the segmentation of a given slice, the "Edit slice" button must be pressed. The software opens a secondary window where the user sets several points along the pericardium. As Figure 5.2 illustrates, the inserted points, marked as red squares, are connected by a blue line that shapes the pericardium contour. When the "Done" button is pressed, the new segmentation is saved, and the user backs to the main window. During this editing process, the "Manual intervention" box gives feedback about the edited slices. Once the edition is finished, the new volume is computed by clicking "Calculate New Volume". The new value is displayed in the manual intervention box so that the automatic and semi-automatic can be assessed and compared simultaneously. Manual intervention can be re-edited and rerun as many times as the user considers necessary.

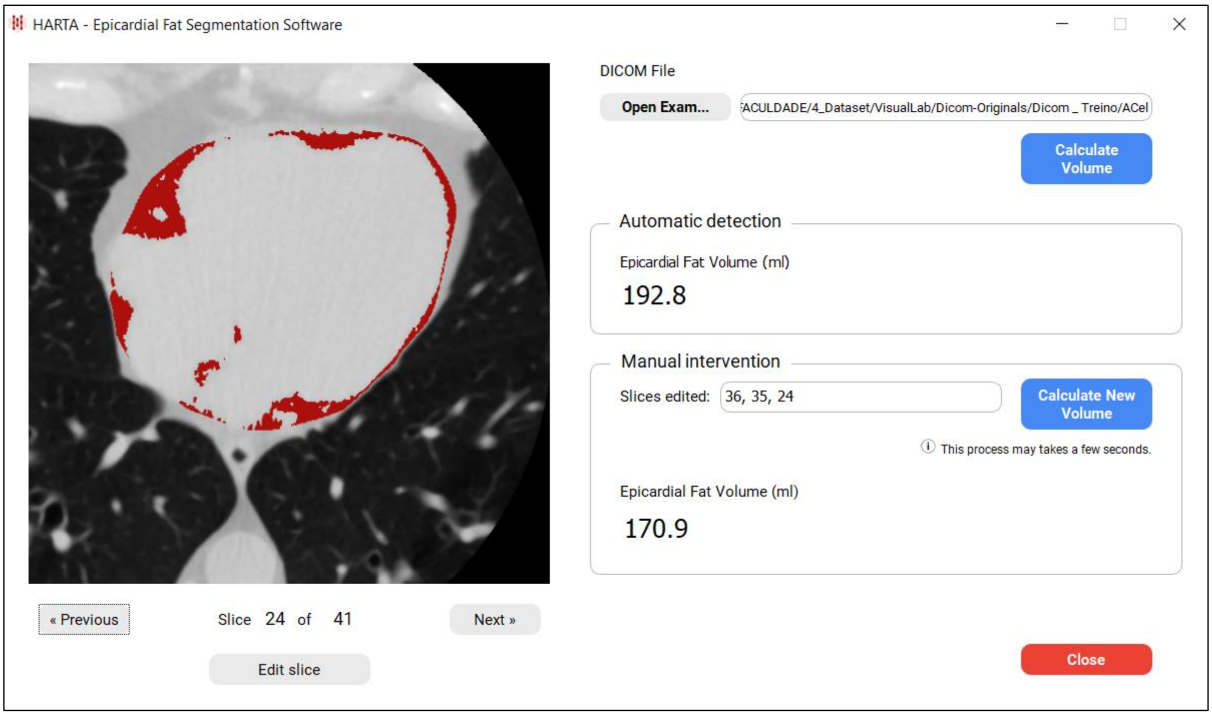

DICOM File: ACULDADE/4_Dataset/VisualLab/Dicom-Originals/Dicom _ Treino/ACel

Epicardial Fat Volume (ml)
192.8

Slices edited: 36, 35, 24

ⓘ This process may takes a few seconds.

Epicardial Fat Volume (ml)
170.9

Slice 24 of 41

Figure 5.1 - Main window of HARTA software.

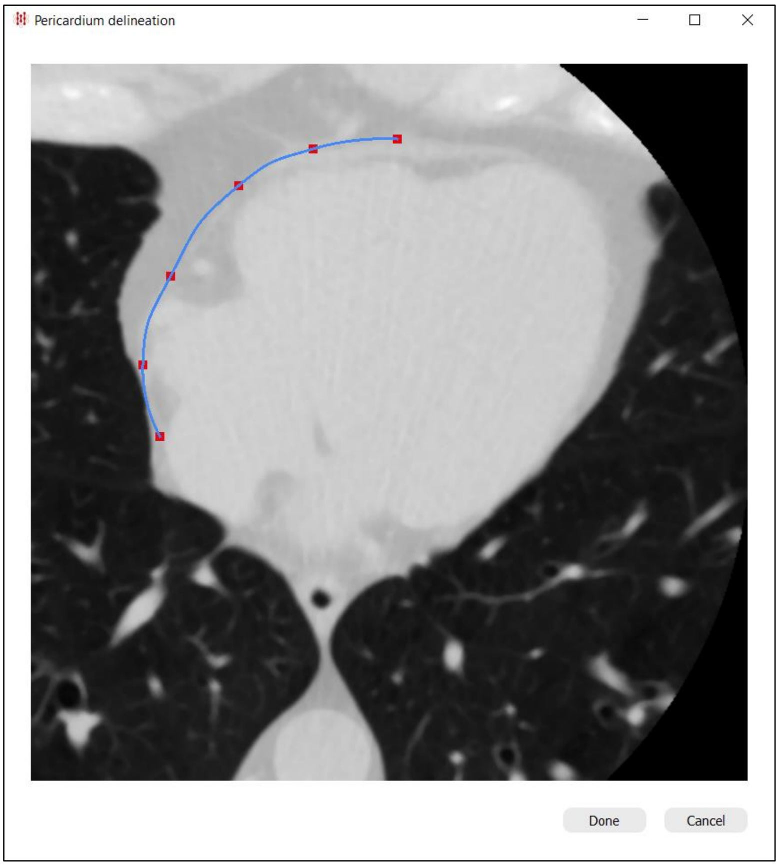

Figure 5.2 - "Pericardium delineation" window during a manually tracing of the pericardium.

5.2. Implementation

The HARTA interface was designed using PyQt5. PyQt is a library that allows the use of Qt GUI framework from *Python*. As the whole algorithm was developed using *Python*, this library makes the interface deployment quicker since both are in the same programming language.

The developed software must be seen as a prototype that provides the main operations so that this tool can be tested and used as a proof of concept. This section briefly describes the more relevant interface actions from the developer perspective. For more deployment details, the developed *Python* functions will be mentioned next to the corresponding action.

- **Calculate Volume button:** This button executes the entire epicardial fat segmentation algorithm described in chapter 4. However, only one of the proposed methods (M1 or M2) is used. The chosen method will be disclosed in the next chapter.

  Function call: _automatic_.segmentEpicardialFat( )

- **Pericardium delineation window:** In this window, the points set along the pericardium are connected by Bézier curves. These are polynomial functions used to create curved paths. A Bézier curve is defined as a set of control points, P_0 through P_n, where n is the curve degree. The first and last control points are always the curve's endpoints, whereas the intermediate control points (if any) generally do not lie on the curve [84].

  Quadratic Bézier curve ($n = 3$) has three control points being a point-to-point linear interpolation of two linear Bézier curves ($n = 2$). In its turn, the cubic Bézier curve ($n = 4$) has four control points being a point-to-point linear interpolation of two quadratic Bézier curves (Figure 5.3). A Bézier curve piece of degree n, is defined as

$$Q(t) = \sum_{i=0}^{n} V_i B_i^n(t) \quad ,0 \leq t \leq 1 \tag{5.1}$$

  where the V_i are the control points and the $B_i^n(t)$ are the Bernstein polynomial

$$B_i^n(t) = \binom{n}{i} t^i (1-t)^{n-i}, i = 0, \ldots, n \tag{5.2}$$

  where $\binom{n}{i}$ is the binominal coefficient.

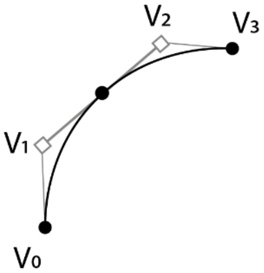

Figure 5.3 - Cubic Bézier curve.

In the pericardium contour, the points are connected by a cubic Bézier curve that promotes a smooth delineation that easily fits this anatomical structure. In this case, the equation curve is given by

$$Q(t) = (1-t)^3V_0 + 3(1-t)^2tV_1 + 3(1-t)t^2V_2 + t^3V_3 \tag{5.3}$$

The curve is initialized after the input of three points to ensure at least four control points. After that, the curve is updated at each new entered point. Figure 5.4 shows the necessary elements to update the Bézier curve.

The squares represent the intermediate control points (besides the endpoints) used in each curve calculation. These points are the extremities of a segment tangent to the curve in each inserted point. To find these segments and their extremities, the following data are considered:

1. The previous and next points (e.g., points A and C);
2. The angle bisector between the segments created with the previous and the current points, and the current and the next points (e.g., dashed segments $\overline{AB}$ and $\overline{BC}$, respectively);
3. Two handles that are perpendicular to the bisector angle. Each handle starts from the current point and has a length proportional to each segment (e.g., handles $\overline{BV_1}$ and $\overline{BV_2}$).

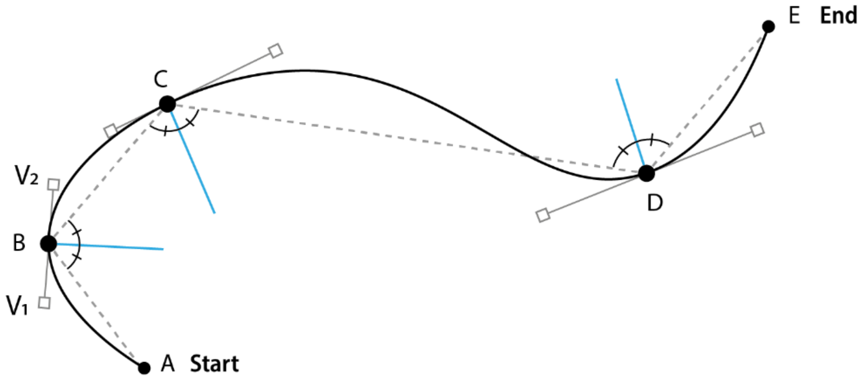

Figure 5.4 - Curve resulting from three consecutive cubic Bézier interpolations.

Functions call: mousePressEvent( ), paintEvent( ) and buildPath( ).

- **Done button:** After finishing the pericardium delineation, the user presses this button. During the action, the new outlined contour overwrites the generated contour in the automatic method.

Function call: onSubmit( )

- **Calculate New Volume button.** This button executes only steps (3) and (4) of the epicardial fat segmentation algorithm: epicardial fat segmentation and EFV quantification, respectively. The ROI masks used in step (3) are the generated ROI masks from the first automatic execution (not modified by the user) and the new ROI masks (outlined by the user).

  Function call: _semiautomatic_.segmentEpicardialFat( )

One of the concerns during the development of this tool was its accessibility. Creating a tool independent of medical software and operating systems gives HARTA great flexibility. Healthcare units using different clinical software can use this tool. Moreover, the fact this software has been developed on a license-free platform as *Python* makes its installation easier and without restrictions. In addition, public availability also allows community input for improvements.

Another concern that was taken into account throughout the development of this work was the algorithm's explanation rather than the code's details. In this way, this tool can be replicated as a plug-in in existing medical software using other programming languages.

The only requirement for HARTA installation is having *Python* and some of its libraries installed on the operating machine. In order to speed up this initial start-up, a short "Get started" tutorial was prepared. These instructions can be found in the GitHub repository, which the link is mentioned at the beginning of this chapter.

The present program is still considered a prototype. The functionalities previously described enable this tool to fulfil the minimum requirements, although it has a considerable margin of progression. Since it has not yet been tested in a real-world context, the next step would be to implement it in a clinical environment and survey the improvements. Further suggestions for future work will be given further.

6.

RESULTS AND DISCUSSION

In chapter 4, two methods (M1 and M2) were described for epicardial fat segmentation and quantification in non-contrast cardiac CT. To recall, M1 approaches pericardium to a semi-ellipse, while the M2 approaches the pericardium to a convex hull.

In this chapter, the performance of each method is compared to understand the viability of their use in segmenting and quantifying epicardial fat accurately in clinical practice. This chapter presents the results and discussion about each proposed method.

Two types of results are evaluated: segmented images and EFV values. These results were compared with the segmented images and the EFV values provided by the VisualLab database as ground truth.

The statistical evaluation metrics used to evaluate the segmentation performance were Dice Similarity Coefficient (DSC), False Positive Rate (FPR), False Negative Rate (FNR) and accuracy (formulas in Section 2.3.3). The EVF quantification performance was assessed by the Bland-Altman comparison and Pearson and Spearman correlation coefficients.

6.1. Registration and assessment images

Before extracting statistical metrics, the segmented images obtained by M1 and M2 were compared with the ground truth, slice-by-slice. The binarized images of automatic and manual segmentation were automatically aligned and scaled using a registration algorithm (Section 2.3.1).

The input of the registration process is a pair of images corresponding to the same slice. One of the images has the manual segmentation (ground truth) of epicardial fat, and the other has the automatic segmentation. The manual segmentation is the "fixed image" taken as the reference, while the automatic segmentation is the "moving image". The registration output is the moving image aligned with the same scale as the fixed image.

Figure 6.2 summarizes the substages of the registration process. Firstly, a keypoint detector and descriptor extractor was created to retain a maximum of 5000 features from each of the two images. The keypoints and descriptors were then computed to construct a vector containing information of each image.

The features of both images were matched by comparing the descriptors achieved in the previous step. The descriptor matcher used was the Brute Force Matcher with Hamming distance as measurement mode. Brute Force is used for matching the features of one image with another. It takes one descriptor of the fixed image and matches to all the moving image descriptors. The exact process is repeated until the fixed image descriptors are all compared. The Hamming distance is used to calculate the number of positions where the two descriptor vectors (of equal length) are different.

All matches were sorted by ascending order of their Hamming distances, and the top 90% were selected. The correspondence of the selected matches was used to estimate the transformation function parameters by finding the homography matrix. A homography is a transformation that maps a set of points in one image to the corresponding ones in another. Since a homography is a 3×3 matrix H, the geometric transformation that relates the two images is given by

$$\begin{bmatrix} x_1 \\ y_1 \\ 1 \end{bmatrix} = H \begin{bmatrix} x_2 \\ y_2 \\ 1 \end{bmatrix} = \begin{bmatrix} h_{00} & h_{01} & h_{02} \\ h_{10} & h_{11} & h_{12} \\ h_{20} & h_{21} & h_{22} \end{bmatrix} \begin{bmatrix} x_2 \\ y_2 \\ 1 \end{bmatrix} \tag{6.1}$$

where (x_1, y_1) and (x_2, y_2) are corresponding points in the fixed and moving images, respectively.

Finally, using the homography matrix, the moving image is transformed into an image that is aligned and rescaled with the fixed image.

After registration, the registered images were compared pixel-by-pixel, resulting in 4-coloured images, hereafter called assessment images. An assessment image, represented in Figure 6.1, can be interpreted as follows:

- Black pixels represent true negatives (TN), correctly classified as no epicardial fat;
- White pixels represent true positives (TP), correctly classified as epicardial fat;
- Red pixels represent false positives (FP), incorrectly classified as epicardial fat;
- Blue pixels represent false negatives (FN), incorrectly classified as no epicardial fat.

The evaluation metrics were extracted from these images.

Figure 6.1 - Assessment image obtained by comparison between manual and automated segmentation.

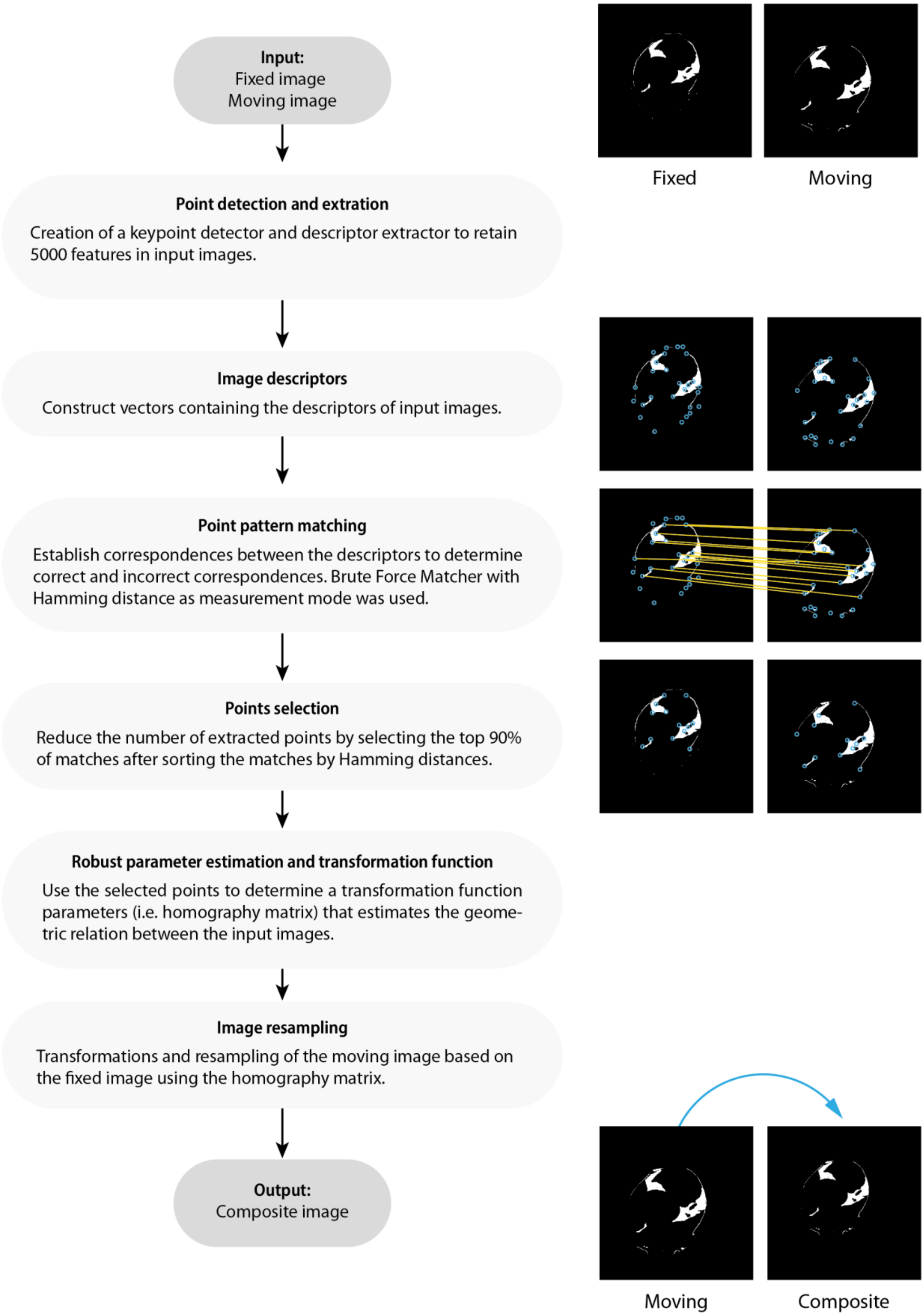

Input:
Fixed image
Moving image

Point detection and extration

Creation of a keypoint detector and descriptor extractor to retain 5000 features in input images.

Image descriptors

Construct vectors containing the descriptors of input images.

Point pattern matching

Establish correspondences between the descriptors to determine correct and incorrect correspondences. Brute Force Matcher with Hamming distance as measurement mode was used.

Points selection

Reduce the number of extracted points by selecting the top 90% of matches after sorting the matches by Hamming distances.

Robust parameter estimation and transformation function

Use the selected points to determine a transformation function parameters (i.e. homography matrix) that estimates the geometric relation between the input images.

Image resampling

Transformations and resampling of the moving image based on the fixed image using the homography matrix.

Output:
Composite image

Figure 6.2 - Image registration.

6.2. Segmentation evaluation

Figure 6.3 summarizes the mean DSC values per exam for each method. The values can be consulted in more detail in Table A.1 of Appendix A.

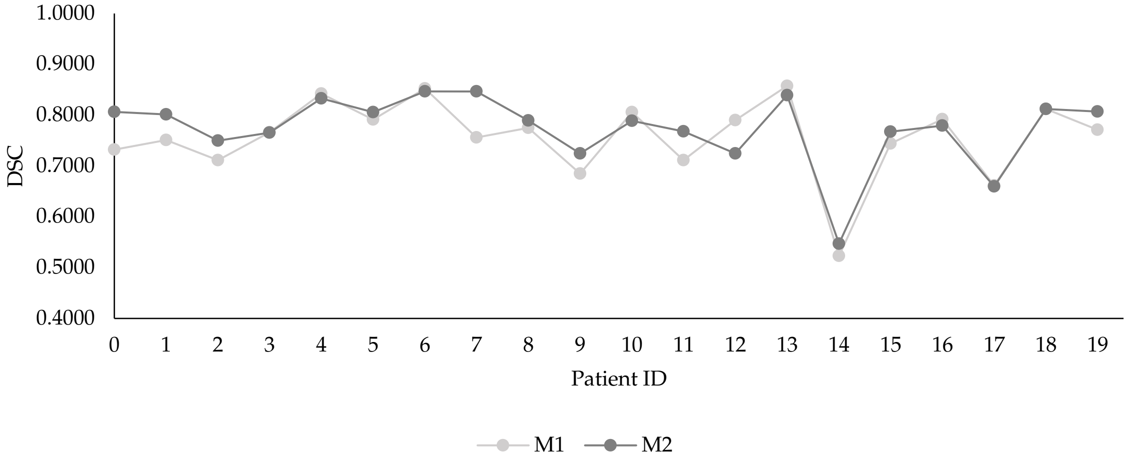

Figure 6.3 - DSC comparison between methods M1 and M2 over database exams.

In general, the M2 method reaches a better performance in 14 out of 20 exams. To better evaluate DSC dispersion among the two methods and their descriptive statistics, Figure 6.4 presents boxplots for each method.

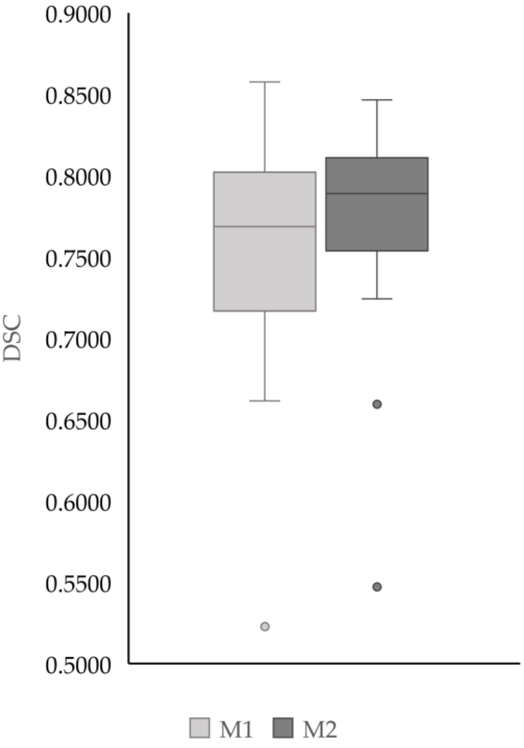

Figure 6.4 - Boxplots representing DSC dispersion for automatic methods M1 and M2.

The median of both methods are similar: 0.7686 to M1 and 0.7888 to M2. Notwithstanding, the higher median of M2 confirms the general better segmentation performance. The boxplot of M1 shows data more spread out than M2, which comprises the same data less dispersed. This aspect may suggest that the M2 method segments all exams approximately with the same quality, while the segmentation performance of the M1 method varies between images.

Analyzing the boxplot outliers, M1 denotes one outlier and M2 two, whereby exam 14 is the common outlier for both methods. Four slices were selected to find the reason for this outlier, each one from different regions of the heart, as illustrated in Figure 6.5.

Exam 14 corresponds to a low-fat heart, where each slice has thin areas of epicardial fat. In superior and middle regions, both methods slightly overestimated epicardial fat, as it can be evaluated by red areas representing FP. In the inferior region, was not detected epicardial fat also due to the small areas. At the first sign, it may not be clear why the segmentation of this exam presents the worst performance. However, as small epicardial fat areas are taken as ground truth, a slight difference negatively impacts the DSC metric.

The same tendency was observed in exam 17, the second outlier denoted by M2, shown in Figure 6.6. Apparently, exam 17 has more coloured areas than exam 14, translating into more false classifications, mainly FP. The reason for presenting more DSC is related to the true/false ratio of this metric formula. Since exam 17 is a more fatty heart, the $2TP$ parcel is greater, and false classifications do not negatively impact DSC as the previous outlier.

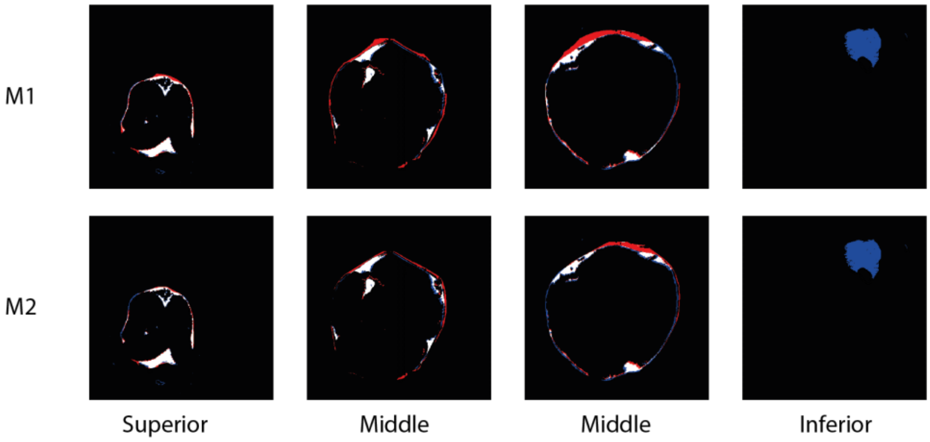

Figure 6.5 - Assessment images from exam 14, a DSC outlier achieved by methods M1 and M2.

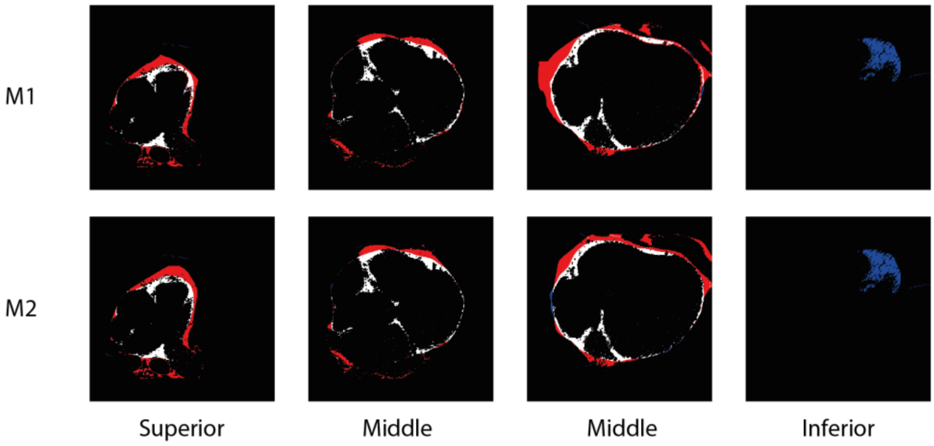

Figure 6.6 - Assessment images from exam 17, a DSC outlier achieved by methods M1 and M2.

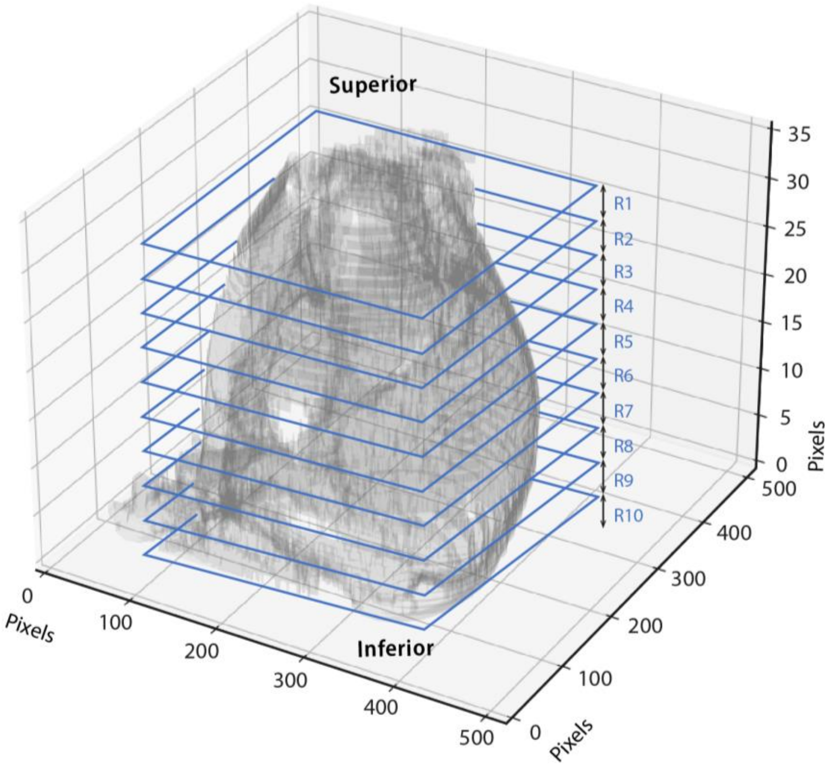

Figure 6.7 - Heart regions marked in a 3D epicardial fat volume result.

To locally evaluate the segmentation performance and better understand how it varies across the heart regions, slices of each exam were grouped into 10 groups from superior to inferior. In Figure 6.7, the regions are marked in a 3D epicardial fat volume result to provide greater spatial awareness about each heart section.

From Figure 6.8, it is possible to conclude that both methods perform better in the middle regions than in superior and inferior regions. To determine the reason for DSC fluctuation throughout the heart, FPR and FNR will be analyzed in each of the three main regions: superior, middle, and inferior. The values analyzed in Figures 6.8-6.10 can be consulted in more detail in Table A.2 of Appendix A.

- **Superior region**

  The superior region will be treated as the first two heart regions (R1 and R2) of Figure 6.7. In this region, lower DSC values are due to the prevalence of FP more than FN [3]. Comparing the two methods, M1 tends to reach higher FPR than M2 (Figure 6.9). In terms of FNR (Figure 6.10), it is M2 that registers higher values.

  The comparative analysis of FP and FN rates can be confirmed by observing Figure 6.11 with a set of slices regarding this region.

---

[3] It is important to note that rates are being compared and not discrete numbers of FP and FN. The TN parcel in FPR denominator (Eq. 2.6, Section 2.3.3) is always far greater than the TP parcel in FNR denominator (Eq. 2.7, Section 2.3.3). Logically, FPR will always be lower in all heart regions, than FNR. However, this does not mean that there are more FN than FP in all regions of the heart.

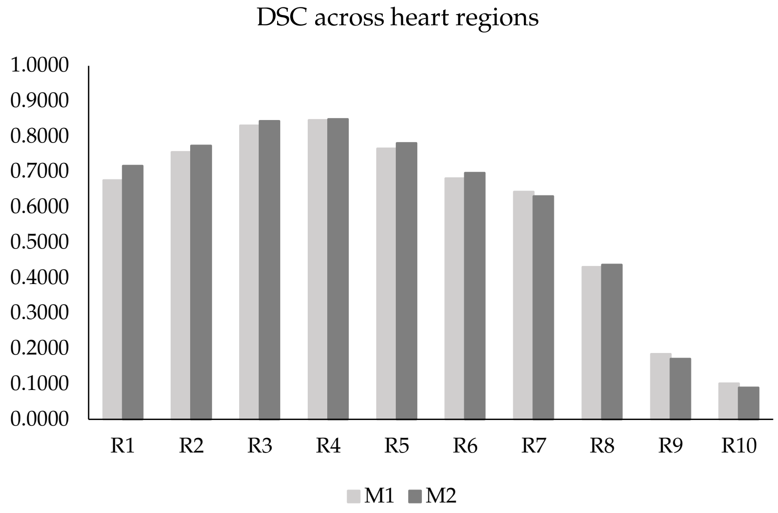

Figure 6.8 - Local DSC from inferior to superior heart regions achieved by methods M1 and M2.

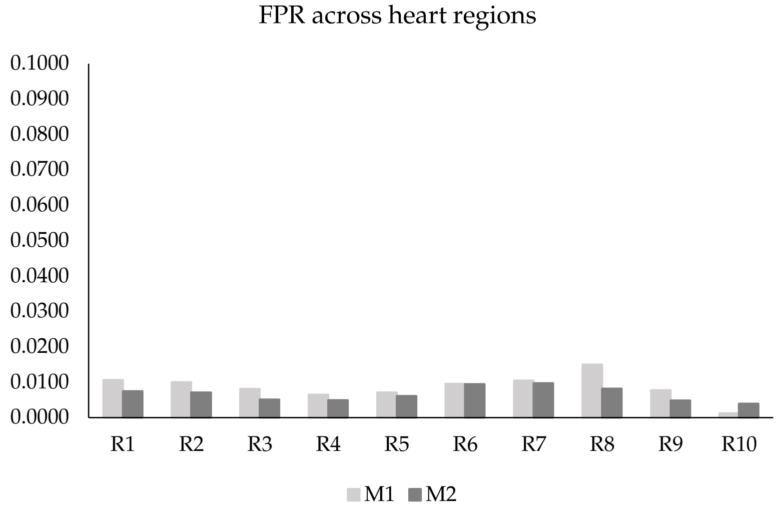

Figure 6.9 - FPR across heart regions achieved by automatic methods M1 and M2.

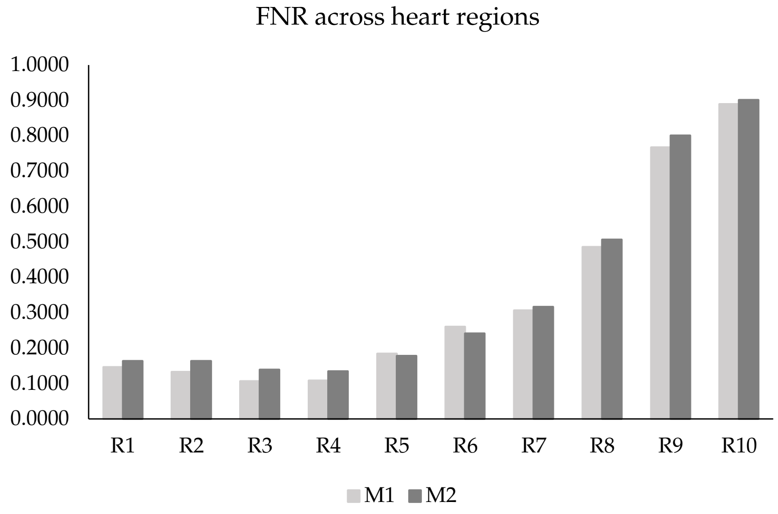

Figure 6.10 - FNR across heart regions achieved by automatic methods M1 and M2.

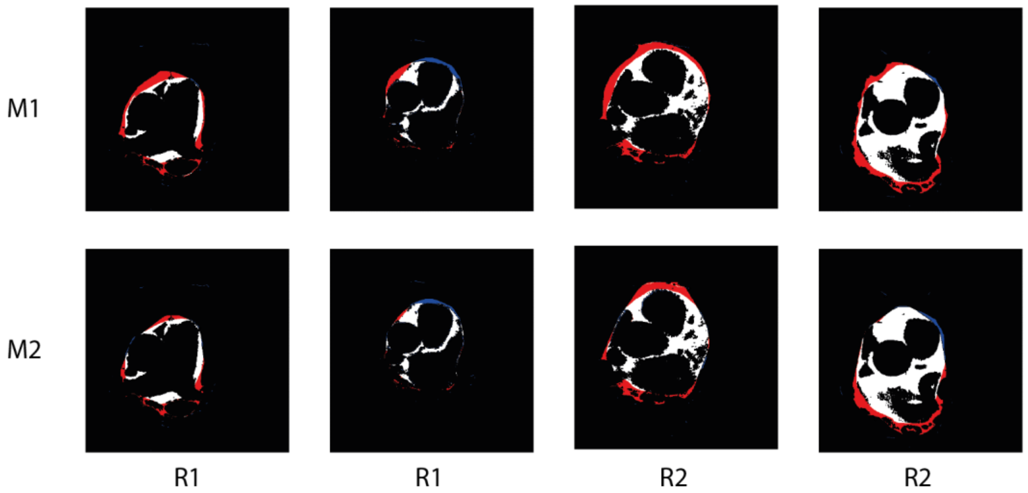

Figure 6.11 - Assessment images of the superior heart region segmented by methods M1 and M2. Each slices pair is from a different exam.

The superior heart region has complex anatomy where the pericardium is attached to the aorta, pulmonary veins and arteries. Since there are more contours in these slices, it is more difficult to distinguish the pericardium. The tendency is to take the outer ROI contour in place of the pericardium, generating a delineation larger than supposed that includes mediastinal fat. As mediastinal and epicardial fat are very similar in terms of grey level, mediastinal fat pixels are falsely classified as epicardial fat, justifying the higher FPR.

- **Inferior region**

The inferior region corresponds to regions R9 and R10 of Figure 6.7, in which R10 can also be referred to as the apex. In the inferior region, lower DSC values are due to the combined prevalence of FN and FP. Notwithstanding, FNR is the more predominant cause in the apex. M1 tends to reach higher FPR than M2 in region R9, while in the apex the situation is reversed (Figure 6.9). In terms of FNR (Figure 6.10), it is the M2 method that registers higher values.

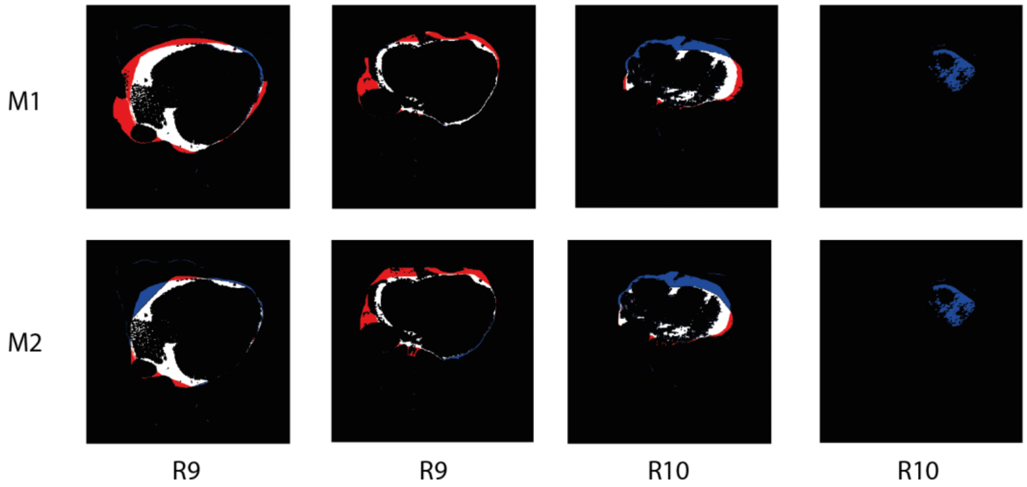

Figure 6.12 - Assessment images of the inferior heart region segmented by methods M1 and M2. Each slices pair is from a different exam.

Near the apex, the pericardial contour is usually thinner and not visible over the entire length. Similar to what happens in the superior region, other contours are often taken in place of the pericardium, generating an epicardial fat area wider than supposed.

Slices have small fat areas in the inferior region, and the pericardium assumes more irregular contours. The automatic process often discards these last slices since any acceptable shape is detected, justifying the FNR increase. In Figure 6.12, the last pair is an example of discarded slices.

The more significant quality segmentation loss in the inferior region compared to the superior can be explained by the discard mechanism mentioned in Section 4.2.2.7. In discarded slices, small sets of pixels representing epicardial fat were classified as negative. However, accounting with these erratic slices would drastically increase (even more) the FPR and meaningfully decrease DSC.

The pericardium contour in the superior and inferior regions comprises much less area than those in the middle. Hence, since they do not contribute significantly to the overall EFV [6], their segmentation is left to specialist intervention.

- **Middle region**

  The middle region corresponds to the regions between R3 to R8 of Figure 6.7. The FN and FP remain relatively low rates, noticing a slight increase of both errors from region R6 onward. Both methods perform better segmentation in the middle region. Analyzing Figure 6.13, it is clear to notice that FP and FN rates are less prevalent in the middle region when compared to superior and inferior regions.

  The middle heart region is less complex in terms of anatomical structures. These slices comprise the heart's chambers, where the pericardium typically follows a more linear contour.

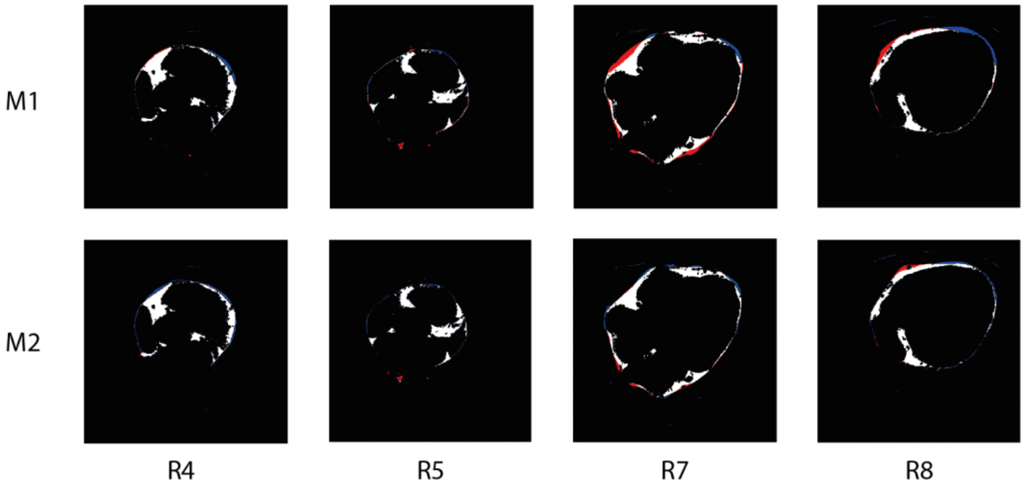

Figure 6.13 - Assessment images of the middle heart region segmented by methods M1 and M2. Each slices pair is from a different exam.

In conclusion, although M1 and M2 reach similar segmentation values, M1 generates more FP (red areas) while M2 tends to cause more FN (blue areas). The same aspect can be confirmed in Table 6.1, which contains the accuracy and confusion matrixes of automatic methods M1 and M2. Values calculated per exam can be consulted in more detail in Table A.3 of Appendix A.

Table 6.1 - Accuracy, True Positive (TP), True Negative (TN), False Positive (FP) and False Negative (FN) rates achieved by automatic methods M1 and M2.

Method	**Accuracy**	**TP Rate**	**TN Rate**	**FP Rate**	**FN Rate**
M1	0.9865	0.8422	0.9895	0.0105	0.1578
M2	0.9883	0.8310	0.9918	0.0082	0.1690

This table also summarizes the global performance of the proposed automatic methods, ensuring a high segmentation performance for both. Nevertheless, M2 is the more accurate method, with an accuracy of 0.9883 compared to 0.9865 achieved by M1.

6.3. **Quantification evaluation**

The epicardial fat volumes obtained in the 20 exams and respective absolute errors (AE) can be found in Table A.4 in Appendix A. Table 6.2 below summarizes the performance of both methods.

The EFV ground truth values range between 242.3 and 29.6 ml. Comparing this range with MAE values, there is an approximately 60% error decrease when using M2. The better results of EFV were obtained because this method selects ROIs closer to the pericardium, avoiding more FP and FN when compared with M1.

Table 6.2 - Mean absolute errors (MAE) obtained for automatic methods M1 and M2.

	MAE (ml)
M1	40.4 ± 34.1
M2	16.0 ± 12.7

Figure 6.14 depicts the dispersion plot of both methods where the manual EFV_M and automatic EFV_A volumes are correlated. Both methods achieved strong correlations by presenting relatively higher Pearson and Spearman correlation coefficients shown in Table 6.3.

Table 6.3 - Pearson and Spearman correlation coefficient achieved by methods M1 and M2.

	Pearson coefficient	Spearman coefficient
M1	0.9240	0.8539
M2	0.9366	0.8773

The coefficients reveal that the correlation between manual and fully automated volumes is better when M2 is used. Also, observing the two plots, it is clear the better performance of M2. The large dispersion observed in M1 suggests that this method tends to overestimate EFV, mainly in fatty hearts. The weaker correlation of M1 is reflected in its oblique fitted line and slope coefficient greater than one. Although the M2 plot presents a high scatter pattern, it seems to follow a positive trend, suggesting a general overestimation of EFV.

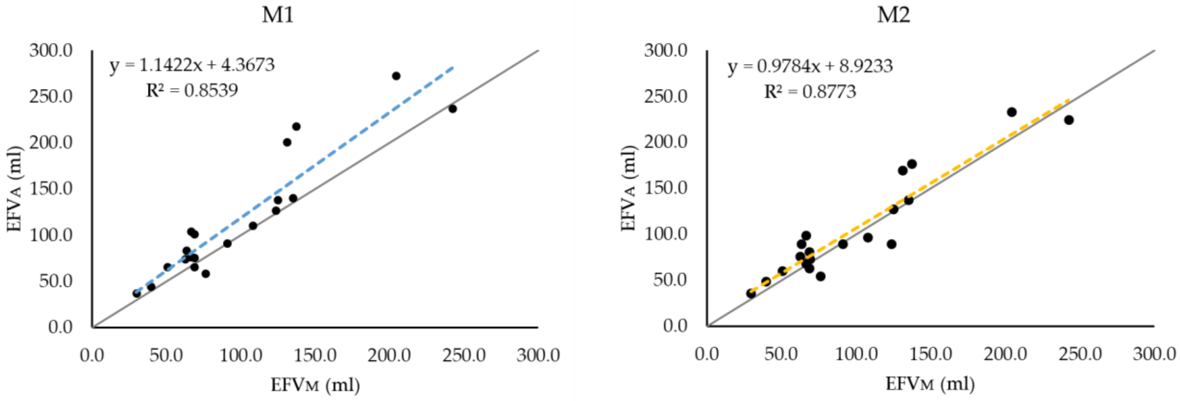

Figure 6.14 - Dispersion plot comparing automatic EFV (EFV_A) and manual EFV (EFV_M) obtained with the automatic methods M1 and M2.

Concerning the nature of the M1 method, these results suggest the semi-ellipse fitting to the ROI upper half works better in hearts with low and medium EFV. For hearts with higher EFV values, a more personalized contour is necessary to fit the pericardium over the entire length and not only in the upper half.

To extract more information about the quantification performance of M1 and M2, Band-Altman analysis was performed.

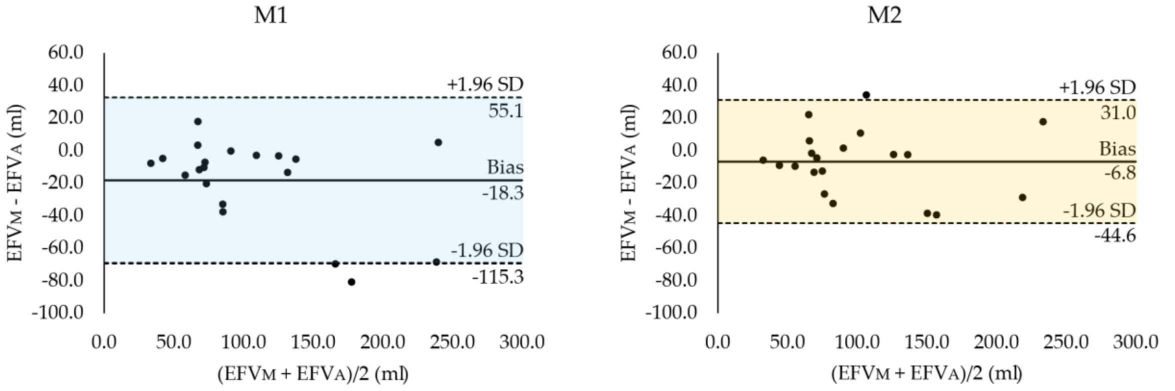

Figure 6.15 - Bland-Altman comparison between automatic EFV (EFV_A) and manual EFV (EFV_M) using the methods M1 and M2.

Observing both Bland-Altman plots, it is clear to find that the M1 confidence interval range is larger than the M2 range: -69.2 to +32.6 ml to M1 and -44.6 to +31.0 ml to M2. In M2 plot, 19 out of 20 samples are contained within the referred 95% confidence, while in the M1 plot, two outliers are counted. The superior limits of the two methods are close, suggesting a similar underestimation of EFV. However, the inferior limits show that M1 promote overestimation with greater amplitudes when compared with M2.

A bias of -18.3 and -6.8 ml was found for M1 and M2, respectively. These values indicate the automatically estimated EFV may lie above these biases, which can point to the existence of a systemic error of overestimation. Comparing the biases of the two methods, the overestimation of EFV is approximately 40% lower when using M2.

In fact, the proposed work follows the trend of fully automatic methods that overestimate the EFV, as reported by other works [6]–[8], [66]. This systemic overestimation can be justified by pericardium anatomical irregularities, making it difficult for an accurate ROI selection. The contour is often done around the pericardium rather than through it, promoting a slight increase of FP.

Overall, these results align with the general concern assumed in the segmentation evaluation section: M1 tends to register a higher prevalence of FP, translating into overestimated EFV compared with M2. Although M1 outputs acceptable segmentations of epicardial fat, the fully automatic method may not be accurate enough for clinical practice. This method could be considered a semi-automatic tool, but it would require many manual adjustments to quantify EFV accurately. Even M2 also overestimates the EFV, the method exhibits a slight difference that may meet more easily the clinical requirements since fewer adjustments would be needed.

It is important to note that the results were obtained considering only one reference (or ground truth). As already studied by other works, there is significant interobserver variability in epicardial fat segmentation. For instance, Ding et al. [3] report a variability of 8.0 ± 4.3% between 2 observers, and Barbosa et al. [15] report 10.4% between 3 observers.

The mean relative percentage difference was calculated to evaluate the variability between each method and the ground truth. The relative percentage difference per exam can be found in Table A.4 of Appendix A. Table 6.4 summarizes the results.

Table 6.4 - Mean relative percentage difference (MRPD) between the ground truth (GT) and the proposed methods M1 and M2, regarding the mean epicardial fat volume (EFV) and standard deviation (SD).

	Mean EFV (ml)	MRPD (%)
GT	97.9 ± 52.7	-
M1	128.0 ± 68.0	40.7 ± 34.1
M2	104.0 ± 55.0	13.1 ± 8.8

The ground truth provided by VisualLab [75] database reports a mean EFV and standard deviation of 97.9 ± 52.7 ml. Even with a slight difference, M2 is the method that presents a mean EFV and standard deviation close to the one taken as the ground truth with 104.0 ±

55.0 ml. Moreover, only M2 presents a mean percentage difference coincident with the interobserver variability values in literature, even though presenting a more extensive range.

Specialists did not test the proposed methods, so this dissertation does not provide inter- or intra-observer variability. For this reason, variability values reported from studies that segment similar cardiac imaging are being taken as a reference. Using this assumption, it is possible to state that M2 may be a potential assisting tool in clinical practice since it can achieve reliable EFV results with few (semi-automatic mode) or no adjustments (fully automatic mode).

6.4. Execution time evaluation

This section evaluates the performance of methods M1 and M2 in terms of execution time. This evaluation was tested on a Microsoft® Windows 10 x64 platform, equipped with an Intel® i7@1,80 GHz and 8 GB of RAM.

Table 6.5 includes the mean time required by each method to segment and quantify epicardial fat in one CT exam. All the execution times per exam can be found in Table A.5 of Appendix A.

Table 6.5 - Mean execution time and standard deviation achieved by the automatic methods M1 and M2.

	Mean execution time (s)
M1	7.3 ± 0.9
M2	8.8 ± 1.0

The time required by each method is similar using either M1 or M2, albeit M1 performs faster. From this analysis, it is possible to conclude that the Gift Wrapping Algorithm used for the convex hull takes more time than the semi-ellipse fitting. Nevertheless, time was not a crucial factor in choosing one method over another in this work. The main goal was to propose an algorithm that requests low computational complexity and runtimes suitable for clinical conditions.

During the development of the algorithm, the use of basic image techniques was prioritized, ending up in a solution with low computation costs. Comparing the achieved runtimes with the times reported in literature, it is possible to conclude that both methods accomplish a positive relation between accuracy and time.

7.

CONCLUSION

This study aimed to assess the feasibility of semi-automatically segmenting and quantifying epicardial fat using basic image techniques. To this purpose, two methods (M1 and M2) were developed. The main difference between these methods is the last operation used to select the ROI regarding the pericardium. The M1 method used a semi-ellipse fitting, while M2 performed a convex hull followed by an opening operation. Both methods were tested in a public database VisualLab [75], with 20 CT exams. The performance of each method was assessed to conclude which is the best method to segment and quantify epicardial fat accurately. Finally, the chosen method was integrated with an interface, and a prototype software (HARTA) was developed.

Both methods achieved similar results in terms of segmentation, although M2 produces slightly better results (DSC = 0.7888 and accuracy = 0.9883). The factor that differentiated the proposed methods was the quantification performance that was significantly better in method M2. The epicardial fat volumes obtained by M2 in the fully automated mode are strongly correlated with the values taken as ground truth (Spearman = 0.8773 and Pearson = 0.9366). However, the automatic measurements resulted in a systemic volume overestimation (bias = -6.8 *ml*), suggesting the need for manual intervention to improve performance, mainly in the last slices of each exam. In other words, the semi-automatic mode of the proposed method improves the performance provided by the fully automatic mode. In this sense, HARTA was created to allow manual adjustments. This prototype software should be seen as a proof of concept, presenting only the basic functionalities needed to validate the method presented.

Although the quite optimistic results, it must be recognized that the segmentation and quantification results did not achieve better performance than all works reported in the state-of-the-art chapter, especially when compared with solutions based on AI. Nevertheless, developing an AI solution with a small database would not constitute a significant contribution compared to works that employ thousands of exams. The focus of this thesis was to propose a sufficiently accurate alternative to these solutions, not requiring extensive databases and training phases with high computational costs. In this perspective, the results suggest a potential straightforward deployment mainly concerning the execution times results.

Responding to the hypothesis initially stated: *Overall, the use of basic image techniques is sufficiently accurate to semi-automatically segment and quantify epicardial fat in non-contrast CT scans and meet the needs of the medical routine.*

Notwithstanding, some improvements to achieve even better segmentation and quantification results with even less manual intervention are not excluded. A description of work contributions and potential ways to pursue future work are detailed in the following sections.

7.1. Work contributions

The main contributions of this dissertation were:

- **A new approach for automatic segmentation and quantification of epicardial fat** that provides unbiased and consistent results with minimal human intervention compared with entire manual procedures. The developed computer-assisted tool does not require neither training phases nor large databases. The use of basic image techniques resulted in a tool with low computational costs and short runtimes. All these properties allow immediate feasibility and deployment in clinical practice.

- **A software prototype** that allows an automatic segmentation process while including features for the physician to perform adjustments if needed. This prototype differentiates the present work since it is a tangible contribution available for public access so that the entire community can use and contribute with improvements. The developed *Python* scripts of the new approach and the prototype software are available online at the following link: https://github.com/aforebelo/HARTA.

- **An article** was also prepared and submitted as an output of the developed work. Until the submission of this thesis, the manuscript is under evaluation.

7.2. Future work

Despite the promising results presented in this thesis, further work is required to obtain more accurate results and get the first version of the proposed software. Some potential solutions are given below:

- **Increase the database** to test the software in a larger range of images, including contrast-enhanced CT scans or/and CT images from different scanners.

  This dissertation used an open-access database. To the best of our knowledge, it is the only public database containing cardiac CT images. A more extensive database of CT exams was initially planned to be provided by a hospital unit. Unfortunately, the exams did not arrive in time to enrich the work developed.

- **Segmentation improvement**, mainly in the last slices of each exam where the epicardial fat area is smaller. One potential solution would be using segmentation based on AI unsupervised methods, specifically in last slices or those needing a more detailed segmentation. Although these improvements have temporal implications, they would require fewer manual interventions by the specialist.

- **Implementation of more software features**: a threshold range input to apply the algorithm in different images previously mentioned; a first and last slice inputs so the specialist can analyse the fat volume in specific heart regions.

- **Performance assessment of the semi-automatic software mode.** This work did not evaluate the software performance regarding the number of adjustments inserted by the specialist. It would be interesting to test the semi-automatic mode in a group of healthcare professionals. In this way, some metrics could be extracted:
    - A survey of failure patterns, so new solutions could be proposed to solve them.
    - The intra- and interobserver variability between measurements.
    - The impact a computed-assisted solution has on cardiologist practice.

BIBLIOGRAPHY

[1] V. H. C. de Albuquerque *et al.*, "Fast fully automatic heart fat segmentation in computed tomography datasets," *Computerized Medical Imaging and Graphics*, vol. 80, Mar. 2020, doi: 10.1016/j.compmedimag.2019.101674.

[2] G. Milanese *et al.*, "Quantification of epicardial fat with cardiac CT angiography and association with cardiovascular risk factors in symptomatic patients: From the ALTER-BIO (alternative cardiovascular bio-imaging markers) registry," *Diagnostic and Interventional Radiology*, vol. 25, no. 1, pp. 35–41, Jan. 2019, doi: 10.5152/dir.2018.18037.

[3] X. Ding, D. Terzopoulos, M. Diaz-Zamudio, D. S. Berman, P. J. Slomka, and D. Dey, "Automated pericardium delineation and epicardial fat volume quantification from noncontrast CT," *Medical Physics*, vol. 42, no. 9, pp. 5015–5026, 2015, doi: 10.1118/1.4927375.

[4] C. Militello *et al.*, "A semi-automatic approach for epicardial adipose tissue segmentation and quantification on cardiac CT scans," *Computers in Biology and Medicine*, vol. 114, Nov. 2019, doi: 10.1016/j.compbiomed.2019.103424.

[5] M. Marwan and S. Achenbach, "Quantification of epicardial fat by computed tomography: Why, when and how?," *Journal of Cardiovascular Computed Tomography*, vol. 7, no. 1, pp. 3–10, 2013, doi: 10.1016/j.jcct.2013.01.002.

[6] J. V. Spearman *et al.*, "Automated quantification of epicardial adipose tissue using CT angiography: Evaluation of a prototype software," *European Radiology*, vol. 24, no. 2, pp. 519–526, Feb. 2014, doi: 10.1007/s00330-013-3052-2.

[7] M. J. Park, J. I. Jung, Y. S. Oh, and H. J. Youn, "Assessment of epicardial fat volume with threshold-based 3-dimensional segmentation in CT: Comparison with the 2-dimensional short axis-based method," *Korean Circulation Journal*, vol. 40, no. 7, pp. 328–333, Jul. 2010, doi: 10.4070/kcj.2010.40.7.328.

[8] D. Dey *et al.*, "Automated Quantitation of Pericardiac Fat From Noncontrast CT," *Investigative Radiology*, vol. 43, no. 2, pp. 145–153, 2008, doi: 10.1097/RLI.0b013e31815a054a.

[9] F. Commandeur *et al.*, "Fully Automated CT Quantification of Epicardial Adipose Tissue by Deep Learning: A Multicenter Study," *Radiology: Artificial Intelligence*, vol. 1, no. 6, Nov. 2019, doi: 10.1148/ryai.2019190045.

[10] G. Coppini, R. Favilla, P. Marraccini, D. Moroni, and G. Pieri, "Quantification of Epicardial Fat by Cardiac CT Imaging," *The Open Medical Informatics Journal*, vol. 4, pp. 126–135, 2010.

[11] A. J. Weinhaus and K. P. Roberts, "Anatomy of the Human Heart," in *Handbook of Cardiac Anatomy, Physiology, and Devices*, Second., P. A. Iaizzo, Ed. New York, USA:

Springer, 2009, pp. 59–87.

[12] O. Rodrigues, F. F. C. Morais, N. A. O. S. Morais, L. S. Conci, L. V. Neto, and A. Conci, "A novel approach for the automated segmentation and volume quantification of cardiac fats on computed tomography," *Computer Methods and Programs in Biomedicine*, vol. 123, pp. 109–128, Jan. 2016, doi: 10.1016/j.cmpb.2015.09.017.

[13] C. X. Wong, A. N. Ganesan, and J. B. Selvanayagam, "Epicardial fat and atrial fibrillation: Current evidence, potential mechanisms, clinical implications, and future directions," *European Heart Journal*, vol. 38, no. 17, pp. 1294–1302, 2017, doi: 10.1093/eurheartj/ehw045.

[14] Y. Wu, A. Zhang, D. J. Hamilton, and T. Deng, "Epicardial Fat in the Maintenance of Cardiovascular Health," *Methodist Debakey Cardiovasc J.*, vol. 13, no. 1, pp. 20–24, 2017, doi: 10.14797/mdcj-13-1-20.

[15] J. G. Barbosa, B. Figueiredo, N. Bettencourt, and J. M. R. S. Tavares, "Towards automatic quantification of the epicardial fat in non-contrasted CT images," *Computer Methods in Biomechanics and Biomedical Engineering*, vol. 14, no. 10, pp. 905–914, 2011, doi: 10.1080/10255842.2010.499871.

[16] D. M. Ouwens, H. Sell, S. Greulich, and J. Eckel, "The role of epicardial and perivascular adipose tissue in the pathophysiology of cardiovascular disease," *Journal of Cellular and Molecular Medicine*, vol. 14, no. 9. pp. 2223–2234, 2010, doi: 10.1111/j.1582-4934.2010.01141.x.

[17] S. W. Rabkin, "Epicardial fat: Properties, function and relationship to obesity," *Obesity Reviews*, vol. 8, no. 3, pp. 253–261, 2007, doi: 10.1111/j.1467-789X.2006.00293.x.

[18] H. S. Sacks *et al.*, "Uncoupling protein-1 and Related Messenger Ribonucleic Acids in Human Epicardial and Other Adipose Tissues: Epicardial Fat Functioning as Brown Fat," *Journal of Clinical Endocrinology and Metabolism*, vol. 94, no. 9, pp. 3611–3615, 2009, doi: 10.1210/jc.2009-0571.

[19] G. A. Roth, C. Johnson, A. Abajobir, and F. Abd-Allah, "Global, Regional, and National Burden of Cardiovascular Diseases for 10 Causes, 1990 to 2015," *Journal of the American College of Cardiology*, vol. 70, no. 1, pp. 1–25, 2017, doi: 10.1016/j.jacc.2017.04.052.

[20] P. Joseph *et al.*, "Reducing the Global Burden of Cardiovascular Disease, Part 1," *Circulation Research*, vol. 121, no. 6, pp. 677–694, 2017, doi: 10.1161/CIRCRESAHA.117.308903.

[21] A. A. Mahabadi *et al.*, "Association of Epicardial Adipose Tissue With Progression of Coronary Artery Calcification Is More Pronounced in the Early Phase of Atherosclerosis Results From the Heinz Nixdorf Recall Study," 2014.

[22] P. M. Gorter *et al.*, "Quantification of epicardial and peri-coronary fat using cardiac computed tomography; reproducibility and relation with obesity and metabolic syndrome in patients suspected of coronary artery disease," *Atherosclerosis*, vol. 197, no. 2, pp. 896–903, Apr. 2008, doi: 10.1016/j.atherosclerosis.2007.08.016.

[23] N. Aslanabadi *et al.*, "Epicardial and Pericardial Fat Volume Correlate with the Severity of Coronary Artery Stenosis," *Journal of Cardiovascular and Thoracic Research*, vol. 6, no. 4, pp. 235–239, Dec. 2014, doi: 10.15171/jcvtr.2014.018.

[24] M. Janik *et al.*, "Epicardial adipose tissue volume and coronary artery calcium to predict myocardial ischemia on positron emission tomography-computed tomography studies," *Journal of Nuclear Cardiology*, vol. 17, no. 5, pp. 841–847, Oct. 2010, doi: 10.1007/s12350-010-9235-1.

[25] H. Marques *et al.*, “Cardiac computed tomography previous to atrial fibrillation ablation – effects of technological improvements and protocol optimization,” *Revista Portuguesa de Cardiologia*, vol. 37, no. 11, pp. 873–883, Nov. 2018, doi: 10.1016/j.repc.2018.03.011.

[26] G. Iacobellis, “Local and systemic effects of the multifaceted epicardial adipose tissue depot,” *Nature Reviews Endocrinology*, vol. 11, no. 6, pp. 363–371, Jun. 2015, doi: 10.1038/nrendo.2015.58.

[27] H. Acet *et al.*, “New inflammatory predictors for non-valvular atrial fibrillation: Echocardiographic epicardial fat thickness and neutrophil to lymphocyte ratio,” *International Journal of Cardiovascular Imaging*, vol. 30, no. 1, pp. 81–89, 2014, doi: 10.1007/s10554-013-0317-4.

[28] T. F. Chao *et al.*, “Epicardial Adipose Tissue Thickness and Ablation Outcome of Atrial Fibrillation,” *PLOS ONE*, vol. 8, no. 9, Sep. 2013, doi: 10.1371/journal.pone.0074926.

[29] G. Iacobellis *et al.*, “Echocardiographic Epicardial Adipose Tissue Is Related to Anthropometric and Clinical Parameters of Metabolic Syndrome: A New Indicator of Cardiovascular Risk,” *Journal of Clinical Endocrinology and Metabolism*, vol. 88, no. 11, pp. 5163–5168, Nov. 2003, doi: 10.1210/jc.2003-030698.

[30] S. Sarin *et al.*, “Clinical Significance of Epicardial Fat Measured Using Cardiac Multislice Computed Tomography,” *American Journal of Cardiology*, vol. 102, no. 6, pp. 767–771, Sep. 2008, doi: 10.1016/j.amjcard.2008.04.058.

[31] X. Ding *et al.*, “Automated pericardial fat quantification from coronary magnetic resonance angiography: feasibility study,” *Journal of Medical Imaging*, vol. 3, no. 1, p. 014002, Feb. 2016, doi: 10.1117/1.jmi.3.1.014002.

[32] D. Davidovich, A. Gastaldelli, and R. Sicari, “Imaging cardiac fat,” *European Heart Journal Cardiovascular Imaging*, vol. 14, no. 7, pp. 625–630, Jul. 2013, doi: 10.1093/ehjci/jet045.

[33] N. Sharma and L. M. Aggarwal, “Automated medical image segmentation techniques,” *Journal of medical physics*, vol. 35, no. 1, pp. 3–14, 2010, doi: 10.4103/0971-6203.58777.

[34] W. A. Kalender, “X-ray computed tomography,” *Physics in Medicine and Biology*, vol. 51, no. 13, Jul. 2006, doi: 10.1088/0031-9155/51/13/R03.

[35] R. A. Powsner and E. R. Powsner, “Single-photon emission computed tomography (SPECT),” in *Essential Nuclear Medicine Physics*, Second., M. Sugden, L. Brindley, K. Charman, and E. Bonnet, Eds. Oxford: Blackwell Pub, 2006, pp. 85–113.

[36] M. A. Campos and A. A. Diaz, “The Role of Computed Tomography for the Evaluation of Lung Disease in Alpha-1 Antitrypsin Deficiency,” *Recent Advances in Chest Medicine*, vol. 153, no. 5, pp. 1240–1248, May 2018, doi: 10.1016/j.chest.2017.11.017.

[37] R. A. Powsner, E. R. Powsner, and R. A. Powsner, “Essential nuclear medicine physics,” in *Essential Nuclear Medicine Physics*, 2nd ed., M. Sugden, L. Brindley, K. Charman, and E. Bonnet, Eds. Oxford: Blackwell Pub, 2006, pp. 20–29.

[38] R. E. Kanza, C. Allard, and M. Berube, “Cardiac findings on non-gated chest computed tomography: A clinical and pictorial review,” *European Journal of Radiology*, vol. 85, no. 2, pp. 435–451, Feb. 2016, doi: 10.1016/j.ejrad.2015.11.042.

[39] E. Lin and A. Alessio, “What are the basic concepts of temporal, contrast, and spatial resolution in cardiac CT?,” *Journal of Cardiovascular Computed Tomography*, vol. 3, no. 6, pp. 403–408, Nov. 2009, doi: 10.1016/j.jcct.2009.07.003.

[40] P. Sahbaee, E. Abadi, W. P. Segars, D. Marin, R. C. Nelson, and E. Samei, “The effect of

contrast Material on radiation Dose at CT: Part II. A Systematic Evaluation across 58 Patient Models1," *Radiology*, vol. 283, no. 3, pp. 749–757, Jun. 2017, doi: 10.1148/radiol.2017152852.

[41] C. P. Purysko, R. Renapurkar, and M. A. Bolen, "When does chest CT require contrast enhancement?," *Cleveland Clinic Journal of Medicine*, vol. 83, no. 6, pp. 423–426, 2016, doi: 10.3949/ccjm.83a.15037.

[42] C. R. Hamilton-Craig, D. Friedman, and S. Achenbach, "Cardiac computed tomography-evidence, limitations and clinical application," *Heart Lung and Circulation*, vol. 21, no. 2, pp. 70–81, Feb. 2012, doi: 10.1016/j.hlc.2011.08.070.

[43] S. Prat-Gonzalez, J. Sanz, and M. J. Garcia, "Cardiac CT: Indications and limitations," *Journal of Nuclear Medicine Technology*, vol. 36, no. 1, pp. 18–24, Mar. 2008, doi: 10.2967/jnmt.107.042424.

[44] R. Chityala and S. Pudipeddi, "Image and Its Properties," in *Image Processing and Acquisition using Python*, Chapman and Hall/CRC, Ed. Boca Raton, Florida, 2020, pp. 37–57.

[45] P. Mildenberger, M. Eichelberg, and E. Martin, "Introduction to the DICOM standard," *European Radiology*, vol. 12, no. 4, pp. 920–927, Apr. 2002, doi: 10.1007/s003300101100.

[46] E. A. B. da Silva and G. V. Mendonca, "Digital Image Processing," in *The Electrical Engineering Handbook*, WAI-KAI CHEN, Ed. Burlington: Academic Press, 2005, pp. 891–910.

[47] B. Zitová and J. Flusser, "Image registration methods: A survey," *Image and Vision Computing*, vol. 21, no. 11, pp. 977–1000, 2003, doi: 10.1016/S0262-8856(03)00137-9.

[48] F. E. Z. A. El-Gamal, M. Elmogy, and A. Atwan, "Current trends in medical image registration and fusion," *Egyptian Informatics Journal*, vol. 17, no. 1, pp. 99–124, Mar. 2016, doi: 10.1016/j.eij.2015.09.002.

[49] D. L. Pham, C. Xu, and J. L. Prince, "Current Methods in Medical Image Segmentation," *Annual Review of Biomedical Engineering*, vol. 2, no. 1, pp. 315–337, 2000, doi: 10.1146/annurev.bioeng.2.1.315.

[50] Z. Ma, J. M. R. S. Tavares, R. N. Jorge, and T. Mascarenhas, "A review of algorithms for medical image segmentation and their applications to the female pelvic cavity," *Computer Methods in Biomechanics and Biomedical Engineering*, vol. 13, no. 2, pp. 235–246, 2010, doi: 10.1080/10255840903131878.

[51] R. Chityala and S. Pudipeddi, "Segmentation," in *Image Processing and Acquisition using Python*, C. and Hall/CRC, Ed. Boca Raton, Florida, 2020, pp. 167–193.

[52] K. K. D. Ramesh, G. Kiran Kumar, K. Swapna, D. Datta, and S. Suman Rajest, "A review of medical image segmentation algorithms," *EAI Endorsed Transactions on Pervasive Health and Technology*, vol. 7, no. 27, 2021, doi: 10.4108/eai.12-4-2021.169184.

[53] R. Pohle and K. D. Toennies, "Segmentation of medical images using adaptive region growing," in *Medical Imaging 2001: Image Processing*, 2001, vol. 4322, pp. 1337–1346, [Online]. Available: http://spiedl.org/terms.

[54] J. Dehmeshki, X. Ye, and J. Costello, "Shape based region growing using derivatives of 3D medical images: application to semiautomated detection of pulmonary nodules," in *Proceedings 2003 International Conference on Image Processing*, 2003, pp. I–1085.

[55] P. M. Thompson and A. W. Toga, "Detection, visualization and animation of abnormal anatomic structure with a deformable probabilistic brain atlas based on random vector field transformations," *Medical Image Analysis*, vol. 1, no. 7, pp. 271–294, 1997.

[56] C. Davatzikos, "Spatial Normalization of 3D Brain Images Using Deformable Models," *Journal of computer assisted tomography*, vol. 20, no. 4, pp. 656–665, 1996.

[57] J. Jiang, P. Trundle, and J. Ren, "Medical image analysis with artificial neural networks," *Computerized Medical Imaging and Graphics*, vol. 34, no. 8, pp. 617–631, Dec. 2010, doi: 10.1016/j.compmedimag.2010.07.003.

[58] P. Su, T. Chen, W. Xu, X. Shao, H. Wang, and Y. Zhao, "Dominant-Set-Based Consensus For Fuzzy C-Means Clustering Ensemble; Dominant-Set-Based Consensus For Fuzzy C-Means Clustering Ensemble," in *2018 International Conference on Machine Learning and Cybernetics (ICMLC)*, 2018, vol. 1.

[59] A. Norouzi *et al.*, "Medical image segmentation methods, algorithms, and applications," *IETE Technical Review (Institution of Electronics and Telecommunication Engineers, India)*, vol. 31, no. 3, pp. 199–213, 2014, doi: 10.1080/02564602.2014.906861.

[60] A. A. Taha and A. Hanbury, "Metrics for evaluating 3D medical image segmentation: Analysis, selection, and tool," *BMC Medical Imaging*, vol. 15, no. 1, Aug. 2015, doi: 10.1186/s12880-015-0068-x.

[61] K. H. Zou *et al.*, "Statistical Validation of Image Segmentation Quality Based on a Spatial Overlap Index," *Academic Radiology*, vol. 11, no. 2, pp. 178–189, 2004, doi: 10.1016/S1076-6332(03)00671-8.

[62] R. Molteni, "Prospects and challenges of rendering tissue density in Hounsfield units for cone beam computed tomography," *Oral and Maxillofacial Radiology*, vol. 116, no. 1, pp. 105–109, 2013, doi: 10.1016/j.oooo.2013.04.013.

[63] Q. Zhang, J. Zhou, B. Zhang, W. Jia, and E. Wu, "Automatic Epicardial Fat Segmentation and Quantification of CT Scans Using Dual U-Nets with a Morphological Processing Layer," *IEEE Access*, vol. 8, pp. 128032–128041, 2020, doi: 10.1109/ACCESS.2020.3008190.

[64] A. Pednekar, A. N. Bandekar, I. A. Kakadiaris, and M. Naghavi, "Automatic Segmentation of Abdominal Fat from CT Data," in *2005 Seventh IEEE Workshops on Applications of Computer Vision (WACV/MOTION'05)*, 2005, vol. 1, pp. 308–315, doi: 10.1109/ACVMOT.2005.31.

[65] A. N. Bandekar, M. Naghavi, and I. A. Kakadiaris, "Automated Pericardial Fat Quantification in CT Data," Sep. 2006.

[66] R. Shahzad *et al.*, "Automatic quantification of epicardial fat volume on non-enhanced cardiac CT scans using a multi-atlas segmentation approach," *Medical Physics*, vol. 40, no. 9, 2013, doi: 10.1118/1.4817577.

[67] A. Norlén *et al.*, "Automatic pericardium segmentation and quantification of epicardial fat from computed tomography angiography," *Journal of Medical Imaging*, vol. 3, no. 3, pp. 034003-undefined, Sep. 2016, doi: 10.1117/1.jmi.3.3.034003.

[68] É. O. Rodrigues, A. Conci, F. F. C. Morais, and M. G. Pérez, "Towards the Automated Segmentation of Epicardial and Mediastinal Fats," in *2015 IEEE International Conference on Industrial Technology (ICIT)*, 2015, pp. 1779–1785, doi: 10.1109/ICIT.2015.7125355.

[69] O. Rodrigues, L. O. Rodrigues, L. S. N. Oliveira, A. Conci, and P. Liatsis, "Automated recognition of the pericardium contour on processed CT images using genetic algorithms," *Computers in Biology and Medicine*, vol. 87, pp. 38–45, Aug. 2017, doi: 10.1016/j.compbiomed.2017.05.013.

[70] O. Rodrigues, V. H. A. Pinheiro, P. Liatsis, and A. Conci, "Machine learning in the prediction of cardiac epicardial and mediastinal fat volumes," *Computers in Biology and Medicine*, vol. 89, pp. 520–529, Oct. 2017, doi: 10.1016/j.compbiomed.2017.02.010.

[71] L. Zhang, J. Sun, B. Jiang, L. Wang, Y. Zhang, and X. Xie, "Development of artificial intelligence in epicardial and pericoronary adipose tissue imaging: a systematic review," *European Journal of Hybrid Imaging*, vol. 5, no. 1, Dec. 2021, doi: 10.1186/s41824-021-00107-0.

[72] X. He *et al.*, "Automatic segmentation and quantification of epicardial adipose tissue from coronary computed tomography angiography," *Physics in Medicine and Biology*, vol. 65, no. 9, May 2020, doi: 10.1088/1361-6560/ab8077.

[73] F. Commandeur *et al.*, "Machine learning to predict the long-term risk of myocardial infarction and cardiac death based on clinical risk, coronary calcium, and epicardial adipose tissue: A prospective study," *Cardiovascular Research*, vol. 116, no. 14, pp. 2216–2225, Dec. 2020, doi: 10.1093/cvr/cvz321.

[74] V. Zlokolica *et al.*, "Semiautomatic Epicardial Fat Segmentation Based on Fuzzy c-Means Clustering and Geometric Ellipse Fitting," *Journal of Healthcare Engineering*, vol. 2017, 2017, doi: 10.1155/2017/5817970.

[75] "Visual Lab, A Computed Tomography Cardiac Dataset," 2014. http://visual.ic.uff.br/en/cardio/ctfat/ (accessed Jun. 27, 2021).

[76] A. A. Omer, O. I. Hassan, A. I. Ahmed, and A. Abdelrahman, "Denoising CT Images using Median based Filters: a Review," in *2018 International Conference on Computer, Control, Electrical, and Electronics Engineering (ICCCEEE)*, 2018, pp. 1–6, doi: 10.1109/ICCCEEE.2018.8515829.

[77] T. Jain, P. Bansod, C. B. Singh Kushwah, and M. Mewara, "Reconfigurable hardware for median filtering for image processing applications," in *Proceedings - 3rd International Conference on Emerging Trends in Engineering and Technology, ICETET 2010*, 2010, pp. 172–175, doi: 10.1109/ICETET.2010.172.

[78] J. N. Sarvaiya, S. Patnaik, and S. Bombaywala, "Image registration by template matching using normalized cross-correlation," in *International Conference on Advances in Computing, Control and Telecommunication Technologies*, 2009, pp. 819–822, doi: 10.1109/ACT.2009.207.

[79] R. C. Gonzalez and R. E. Woods, "Morphological Image Processing," in *Digital Image Processing*, A. Dworkin, J. McDonnell, V. O'Brien, D. A. George, and G. Dulles, Eds. Upper Saddle River, New Jersey: Pearson/Prentice Hall, 2002, pp. 519–560.

[80] L. He, X. Ren, Q. Gao, X. Zhao, B. Yao, and Y. Chao, "The connected-component labeling problem: A review of state-of-the-art algorithms," *Pattern Recognition*, vol. 70, pp. 25–43, Oct. 2017, doi: 10.1016/j.patcog.2017.04.018.

[81] H. Samet, "Connected Component Labeling Using Quadtrees," *Journal of the ACM*, vol. 28, no. 3, pp. 487–501, Aug. 1981.

[82] M. A. Jayaram and H. Fleyeh, "Convex Hulls in Image Processing: A Scoping Review," *American Journal of Intelligent Systems*, vol. 6, no. 2, pp. 48–58, 2016, doi: 10.5923/j.ajis.20160602.03.

[83] H. Shmilovich *et al.*, "Threshold for the upper normal limit of indexed epicardial fat volume: Derivation in a healthy population and validation in an outcome-based study," *American Journal of Cardiology*, vol. 108, no. 11, pp. 1680–1685, Dec. 2011, doi: 10.1016/j.amjcard.2011.07.031.

[84] L. Shao and H. Zhou, "Curve Fitting with Bézier Cubics," *Graphical Models and Image Processing*, vol. 58, no. 3, pp. 223–232, 1996, doi: https://doi.org/10.1006/gmip.1996.0019.

[85] R. C. Gonzalez and R. E. Woods, "Introduction," in *Digital Image Processing*, Pearson, Ed. Hudson Street, New York, 2018, pp. 1–28.

[86] R. C. Gonzalez and R. E. Woods, "Digital Image Fundamentals," in *Digital Image Processing*, A. Dworkin, J. McDonnell, V. O'Brien, D. A. George, and G. Dulles, Eds. Upper Saddle River, New Jersey, 2002, pp. 34–71.

[87] R. Chityala and S. Pudipeddi, "Spatial Filters," in *Image Processing and Acquisition using Python*, Chapman and Hall/CRC, Ed. Boca Raton, Florida, 2020, pp. 61–92.

[88] R. C. Gonzalez and R. E. Woods, "Image Enhancement in Spatial Domain," in *Digital Image Processing*, A. Dworkin, J. McDonnell, V. O'Brien, D. A. George, and G. Dulles, Eds. Upper Saddle River, New Jersey, 2002, pp. 75–142.

A

TABLES

Appendix A contains the tables with the metrics extracted from segmented slices of each patient exam. The analysis of the results is addressed in Chapter 6 and grouped by the following sections: segmentation evaluation (Section 6.2), quantification evaluations (Section 6.3) and execution time evaluation (Section 6.4).

Regarding the **segmentation evaluation**, Table A.1 and Table A.2 summarize the metrics results per exam, while Table A.3 evaluate the segmentation per heart region:

- Table A.1 presents the Dice Similarity Coefficient (DSC) per exam achieved for the automatic methods M1 and M2.
- Table A.2 summarizes the metrics DSC, False Positive Rate (FPR) and False Negative Rate achieved by automatic methods M1 and M2 for each of the 10 heart regions.
- Table A.3 presents the accuracy, True Positive (TP), True Negative (TN), False Positive (FP) and False Negative (FN) rates achieved by automatic methods M1 and M2.

Regarding the **quantification evaluation**, Table A.4 compares the Epicardial Fat Volume (EFV) achieved by the methods M1 and M2 and the ground truth (GT). It also presents the respective absolute errors (AE) and relative percentage difference (RD).

Finally, concerning **execution time evaluation**, Table A.5 shows the time to segment and quantify the epicardial fat for each exam using the M1 and M2 methods.

Table A.1 - Dice Similarity Coefficient (DSC) per exam achieved for the automatic methods M1 and M2.

Patient ID	DSC	
	M1	M2
0	0.7321	0.8063
1	0.7379	0.8011
2	0.7115	0.7498
3	0.7659	0.7653
4	0.8421	0.8328
5	0.7839	0.8059
6	0.8522	0.8464
7	0.7563	0.8465
8	0.7749	0.7891
9	0.6859	0.7248
10	0.7838	0.7886
11	0.7110	0.7677
12	0.7838	0.7242
13	0.8575	0.8392
14	0.4962	0.4985
15	0.7438	0.7672
16	0.7892	0.7795
17	0.6565	0.6594
18	0.8042	0.8121
19	0.7712	0.8072

Table A.2 - Dice Similarity Coefficient (DSC), False Positive Rate (FPR) and False Negative Rate (FNR) achieved for the automatic methods M1 and M2 in each of the 10 heart regions.

Patient ID	DSC		FPR		FNR	
	M1	M2	M1	M2	M1	M2
R1	0.6768	0.7170	0.0106	0.0074	0.1462	0.1632
R2	0.7563	0.7737	0.0100	0.0071	0.1327	0.1641
R3	0.8312	0.8442	0.0081	0.0051	0.1063	0.1393
R4	0.8464	0.8493	0.0065	0.0049	0.1086	0.1344
R5	0.7657	0.7818	0.0071	0.0061	0.1843	0.1784
R6	0.6818	0.6971	0.0095	0.0094	0.2606	0.2417
R7	0.6435	0.6311	0.0105	0.0097	0.3064	0.3162
R8	0.4311	0.4378	0.0150	0.0082	0.4863	0.5063
R9	0.1845	0.1711	0.0077	0.0049	0.7673	0.8006
R10	0.1017	0.0897	0.0012	0.0039	0.8897	0.9011

Table A.3 - Accuracy, True Positive (TP), True Negative (TN), False Positive (FP) and False Negative (FN) rates achieved by automatic methods M1 and M2.

Patient ID	**Accuracy**		**TP Rate**		**TN Rate**		**FP Rate**		**FN Rate**	
	M1	**M2**	**M1**	**M2**	**M1**	**M2**	**M1**	**M2**	**M1**	**M2**
0	0.9723	0.9832	0.6233	0.7404	0.9968	0.9964	0.0032	0.0036	0.3767	0.2596
1	0.9876	0.9923	0.6647	0.7497	0.9980	0.9982	0.0020	0.0018	0.3353	0.2503
2	0.9835	0.9867	0.5812	0.6286	0.9987	0.9989	0.0013	0.0011	0.4188	0.3714
3	0.9913	0.9916	0.7492	0.7873	0.9962	0.9953	0.0038	0.0047	0.2508	0.2127
4	0.9897	0.9890	0.8994	0.9030	0.9921	0.9915	0.0079	0.0085	0.1006	0.0970
5	0.9685	0.9741	0.6758	0.7292	0.9980	0.9959	0.0020	0.0041	0.3242	0.2708
6	0.9956	0.9954	0.8556	0.8620	0.9976	0.9973	0.0024	0.0027	0.1444	0.1380
7	0.9829	0.9914	0.6447	0.8342	0.9982	0.9961	0.0018	0.0039	0.3553	0.1658
8	0.9839	0.9846	0.7053	0.7264	0.9965	0.9965	0.0035	0.0035	0.2947	0.2736
9	0.9957	0.9964	0.7671	0.7931	0.9972	0.9977	0.0028	0.0023	0.2329	0.2069
10	0.9922	0.9924	0.6832	0.6893	0.9993	0.9993	0.0007	0.0007	0.3168	0.3107
11	0.9943	0.9954	0.7839	0.7983	0.9962	0.9973	0.0038	0.0027	0.2161	0.2017
12	0.9930	0.9909	0.7596	0.7118	0.9976	0.9967	0.0024	0.0033	0.2404	0.2882
13	0.9927	0.9919	0.8686	0.8862	0.9956	0.9940	0.0044	0.0060	0.1314	0.1138
14	0.9800	0.9822	0.4750	0.5216	0.9912	0.9907	0.0088	0.0093	0.5250	0.4784
15	0.9803	0.9846	0.6440	0.6754	0.9978	0.9973	0.0022	0.0027	0.3560	0.3246
16	0.9904	0.9903	0.7529	0.7355	0.9967	0.9968	0.0033	0.0032	0.2471	0.2645
17	0.9731	0.9754	0.4975	0.5075	0.9996	0.9990	0.0004	0.0010	0.5025	0.4925
18	0.9939	0.9943	0.7806	0.7989	0.9976	0.9975	0.0024	0.0025	0.2194	0.2011
19	0.9912	0.9925	0.8622	0.8849	0.9931	0.9940	0.0069	0.0060	0.1378	0.1151

Table A.4 - Epicardial Fat Volume (EFV) achieved by methods M1 and M2 and respective absolute errors (AE) and relative percentage difference (RPD) compared to the ground truth (GT).

Patient ID	EFV (ml)			AE (ml)		RPD (%)	
	GT	M1	M2	M1	M2	M1	M2
0	137.1	254.4	176.8	117.3	39.7	85.6	15.6
1	68.7	119.2	81.3	50.5	12.6	73.5	10.6
2	124.9	155.8	127.4	30.9	2.5	24.7	1.6
3	66.4	97.9	68.1	31.5	1.7	47.4	1.7
4	242.3	150.5	224.5	91.8	17.8	37.9	11.8
5	204.3	316.0	233.1	111.7	28.8	54.7	9.1
6	68.8	71.9	62.8	3.1	6.0	4.5	8.3
7	123.6	178.0	89.4	54.4	34.2	44.0	19.2
8	134.9	155.1	137.5	20.2	2.6	15.0	1.7
9	29.6	43.2	35.6	13.6	6.0	45.9	13.9
10	90.8	91.3	89.4	0.5	1.4	0.6	1.5
11	39.7	52.5	48.8	12.8	9.1	32.2	17.3
12	68.8	96.0	73.4	27.2	4.6	39.5	4.8
13	76.3	64.9	54.2	11.4	22.1	14.9	34.1
14	63.2	103.2	89.9	40.0	26.7	63.3	25.9
15	107.8	123.5	97.0	15.7	10.8	14.6	8.7
16	66.4	119.4	99.0	53.0	32.6	79.8	27.3
17	131.1	212.8	169.7	81.7	38.6	62.3	18.1
18	50.6	69.9	60.3	19.3	9.7	38.1	13.9
19	62.4	84.2	75.8	21.8	13.4	34.9	15.9

Table A.5 - Execution times to segment and quantify the epicardial fat in each exam, using the automatic methods M1 and M2.

Patient ID	**Execution time (s)**	
	M1	**M2**
0	6.8	8.0
1	6.4	8.1
2	6.8	8.6
3	6.6	8.7
4	7.7	9.9
5	6.9	8.2
6	6.2	7.3
7	6.7	8.2
8	5.9	7.4
9	9.0	11.1
10	8.1	9.8
11	8.1	9.8
12	6.8	8.5
13	7.1	8.4
14	7.4	9.1
15	6.8	8.1
16	9.4	11.1
17	7.8	8.1
18	7.7	8.6
19	7.8	9.3

B

METHODOLOGY FLOWCHART

In this dissertation, image processing methods for automatic epicardial fat segmentation are described in chapter 4. The ROI refinement step, which consists of manual adjustments by the specialist, are presented in chapter 5.

Appendix B aims to overview the developed work through a flowchart diagram that summarizes the entire process from DICOM files upload until epicardial fat volume output. Figure B.1 outline the process, coupled with output images of each step.

For programming details, the developed scripts are available at the following link: https://github.com/aforebelo/HARTA. In particular, the functions of all steps presented in this appendix are in the file called _automatic_.py.

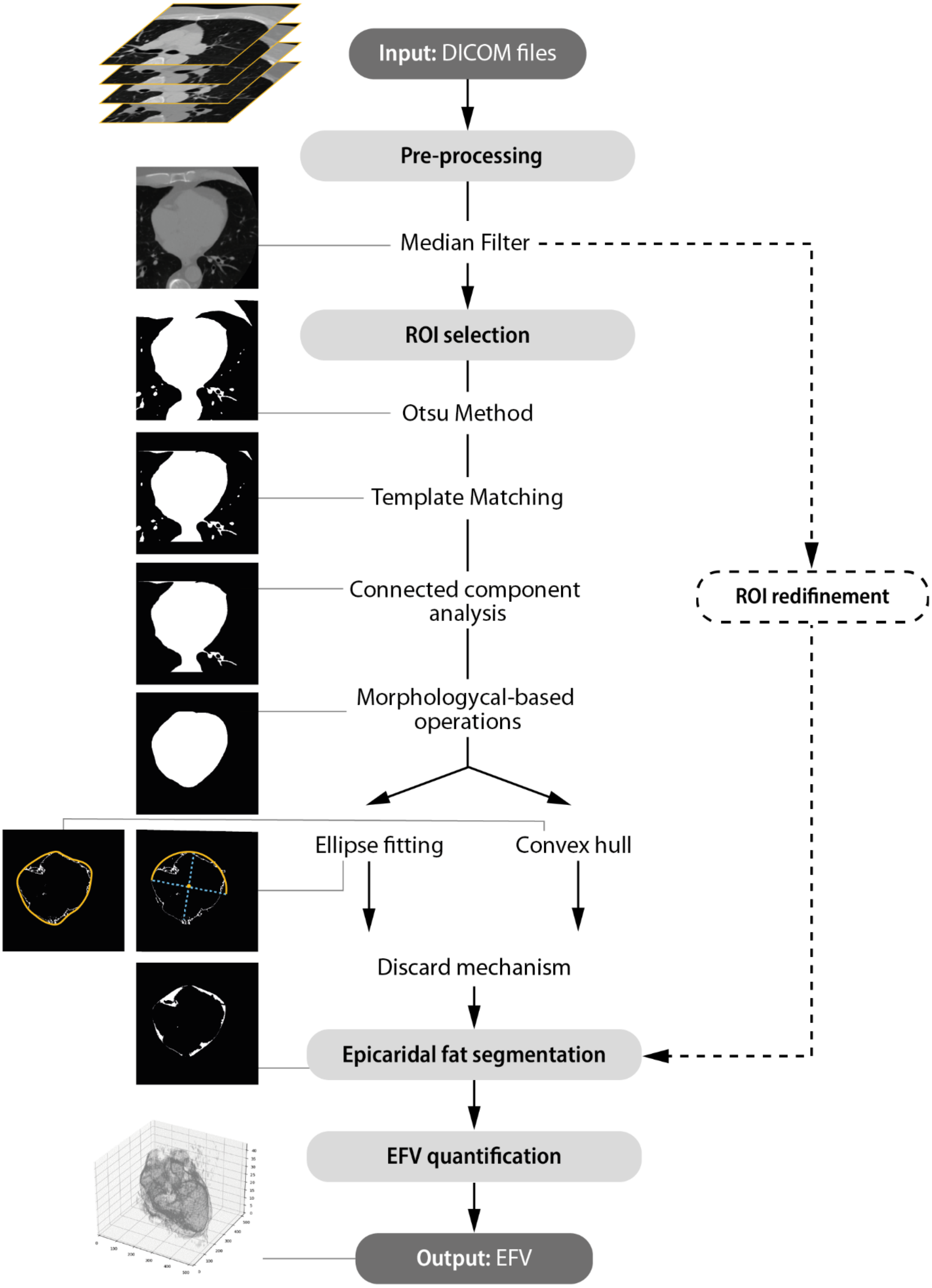

Figure B.1 - Flowchart of the adopted methodology and supported by output images of each step.

C

IMAGE PROCESSING BASIC CONCEPTS

Appendix C aims to support the reader in terms of the basic concepts in image processing. Firstly, the concept of digital image and its representation is introduced, as well as the bit-depth concept and the role in medical image storage. Finally, the definition of (spatial) filtering is addressed, and its mechanism is briefly described.

C.1. Representation of Digital Image

An image may be defined as a two-dimensional function, $f(x, y)$, where x and y are spatial (plane) coordinates and the amplitude of f, at any pair of coordinates (x, y), is the intensity or grey level of the image at that point. When x, y, and f are discrete quantities, the image is defined as a digital image [85]. The coordinate convention used to represent a digital image with M rows and N columns is illustrated in Figure C.2.

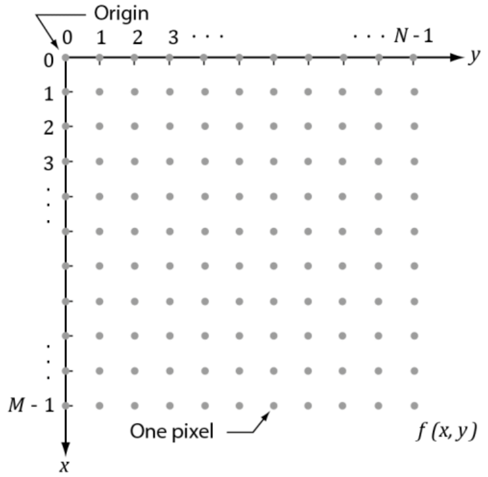

Figure C.2 - Coordinate convention to represent digital images. Adapted from Gonzalez and Woods [86].

Accordingly to the preceding convention, a $M \times N$ digital image can be seen as a matrix and therefore can be written in the following compact matrix form presented by equation C.1.

$$f(x,y) = \begin{bmatrix} f(0,0) & f(0,1) & \dots & f(0,N-1) \\ f(1,0) & f(1,1) & \dots & f(1,N-1) \\ \vdots & \vdots & & \vdots \\ f(M-1,0) & f(M-1,1) & \dots & f(M-1,N-1) \end{bmatrix} \qquad (C.1)$$

C.2. Bit-Depth

The digitization process requires decisions about values for M, N, and the number of discrete grey levels allowed for each pixel. The only requirement of these values is that they have to be positive integers. Regarding the grey levels, due to processing storage and sampling hardware considerations, the number of grey levels is given by

$$L = 2^{bitdepth} \tag{C.2}$$

The pixel range of a given image format is determined by bit-depth, with a range of $[0, L-1]$. For example, an 8-bit image will have a range of $[0, 2^8 - 1] = [0, 255]$. As expected, an image with higher bit-depth needs more storage in disk and memory. The number, b, of bits required to store a digitized image is

$$b = M \times N \times bitdepth \tag{C.3}$$

Most common photographic formats such as JPEG and PNG use 8 bits for storage and only have positive values. Medical and microscope images use a higher bit-depth, as scientific applications demand higher accuracy. A 16-bit medical image has both positive and negative pixel values, with a range of [- 32768, +32767] for a total number of 65536 (= 2^{16}) values [44], [86].

Scientific image formats store the pixel values at high precision to ensure that physical phenomena records are not lost. For example, how was approached in Section 2.2.1, in CT, a pixel value of upper than 1000 indicates bone. If the image is stored in 8-bit, the pixel value of bone would be truncated at 255, so the information will be permanently lost. The most significant pixels in CT have an intensity upper than 255 and hence need higher bit-depth [44].

C.3. Filtering

In image processing, filtering can be seen as the heart of image quality and further processing. A filter removes undesired features from the image, such as noise or other visually distracting impurities or, in some cases, might produce errors in further processing [87].

Each filter has a specific utility and is designed to either remove a type of noise or to enhance aspects of the image [87]. Image enhancement falls into two broad categories:

- **Spatial domain**, which refers to the image plane itself, and approaches in this category are based on direct manipulation of pixels in an image [88].
- **Frequency domain**, which refers to processing techniques based on modifying the Fourier transform of an image [88].

In regards to the present work, image enhancement is accomplished exclusively in the spatial domain.

C.3.1. Spatial filtering

Spatial domain methods operate directly on pixels composing an image and can be denoted by the expression

$$g(x,y) = T[f(x,y)] \tag{C.4}$$

where $f(x, y)$ is the input image, $g(x, y)$ is the processed image, and T is an operator on f, defined over some neighbourhood of (x, y) [86].

The neighbourhood about a point (x, y) is defined by using a square or rectangular sub-image area centred at (x, y), as Figure C.3 shows. The sub-image is defined as a mask, kernel, filter or window, with the first three terms being the most prevalent terminology. Each value in a mask is known as a coefficient [87], [88].

The centre of the mask is moved along the image from pixel to pixel, starting at the top left corner. The operator T is applied at each location (x, y) to yield the output g at that location. The process utilizes only the pixels in the image area spanned by the mask [88].

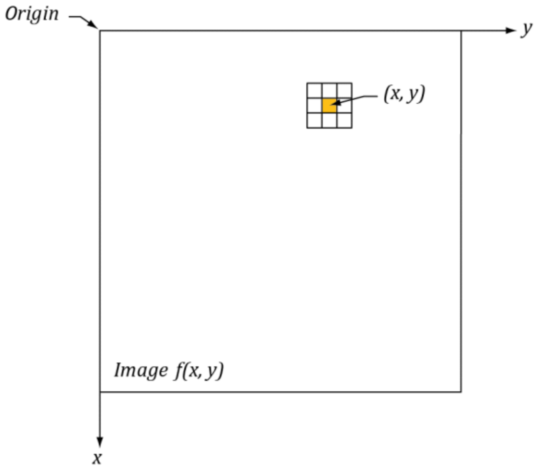

Figure C.3 - A 3×3 neighbourhood about a point (x, y) in an image. Adapted from Gonzalez and Woods [88].

C.3.2. Mechanism of spatial filtering

The process of spatial filtering is illustrated in Figure C.4. This process involves moving the filter mask from point to point in an image. At each point (x, y), and for linear spatial filter, the response is given by a sum of products of the filter coefficients and the corresponding image pixels in the area spanned by the filter mask [88].

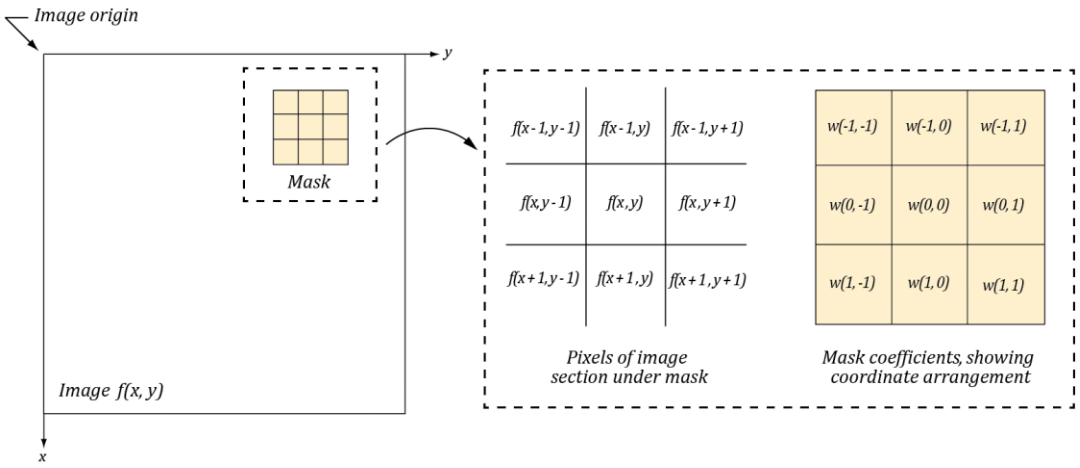

Figure C.4 - Mechanism of spatial filtering. Adapted from Gonzalez and Woods [88].

In general, linear filtering of an image f of size $M \times N$ with a filter mask of size $m \times n$ is given by the following expression

$$g(x,y) = \sum_{s=-a}^{a} \sum_{t=-b}^{b} w(s,t) f(x+s, y+t) \qquad (C.5)$$

where, $a = (m-1)/2$ and $b = (n-1)/2$, due to the coefficient $w(0,0)$ coincides with image value $f(x,y)$, indicating that the mask is centred at (x,y) when the sum computation of products takes place.

The linear filtering process given in equation C.6 is similar to a frequency domain concept called convolution. For this reason, linear spatial filtering often is referred to as "convolving a mask with an image" [88].

NOVA SCHOOL OF
SCIENCE & TECHNOLOGY

SEMI-AUTOMATIC APPROACH FOR EPICARDIAL FAT SEGMENTATION AND QUANTIFICATION ON NON-CONTRAST CARDIAC CT

ANA FILIPA OLIVA REBELO

2021